ISBN 978-82-326-6127-5 (printed ver.)
ISBN 978-82-326-5782-7 (electronic ver.)
ISSN 1503-8181 (printed ver.)
ISSN 2703-8084 (electronic ver.)

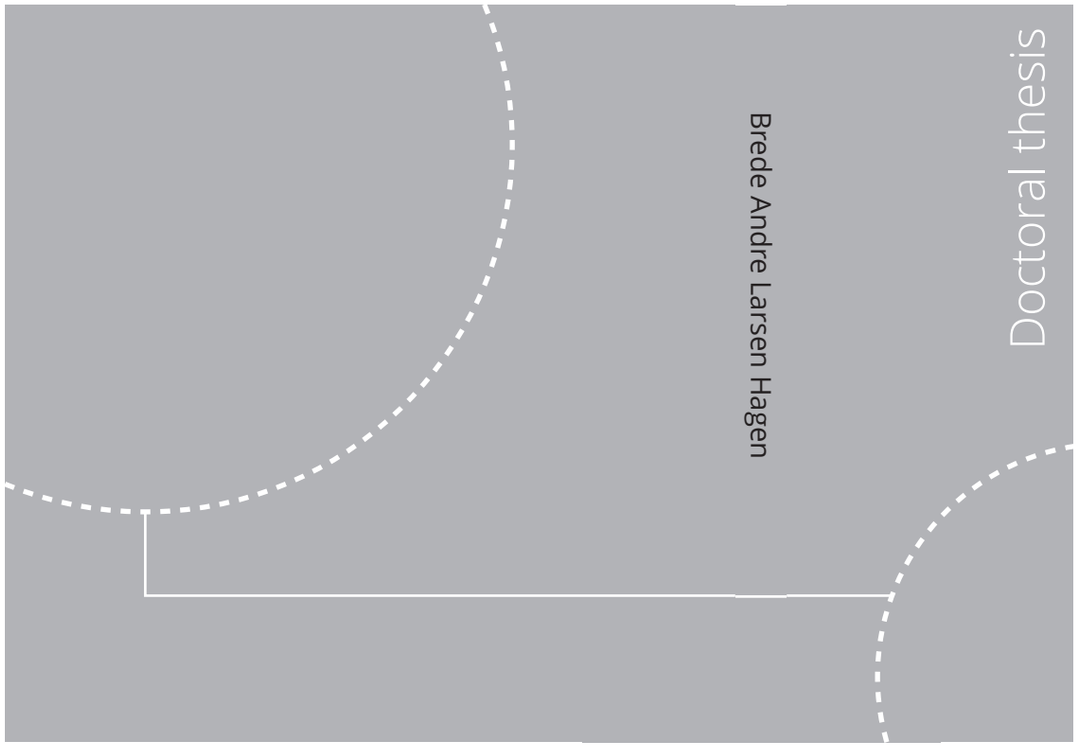

Doctoral theses at NTNU, 2022:147

Brede Andre Larsen Hagen

Gradient-based design optimization and off-design performance prediction of Rankine cycles and Radial Inflow Turbines

NTNU
Norwegian University of
Science and Technology

Doctoral theses at NTNU, 2022:147

NTNU
Norwegian University of
Science and Technology
Thesis for the degree of
Philosophiae Doctor
Faculty of Engineering
Department of Energy and Process Engineering

NTNU
Norwegian University of
Science and Technology

Brede Andre Larsen Hagen

Gradient-based design optimization and off-design performance prediction of Rankine cycles and Radial Inflow Turbines

Thesis for the degree of Philosophiae Doctor

Trondheim, May 2022

Norwegian University of Science and Technology
Faculty of Engineering
Department of Energy and Process Engineering

NTNU
Norwegian University of
Science and Technology

NTNU
Norwegian University of Science and Technology

Thesis for the degree of Philosophiae Doctor

Faculty of Engineering
Department of Energy and Process Engineering

ISBN 978-82-326-6127-5 (printed ver.)
ISBN 978-82-326-5782-7 (electronic ver.)
ISSN 1503-8181 (printed ver.)
ISSN 2703-8084 (electronic ver.)

Doctoral theses at NTNU, 2022:147

PRINTED IN NORWAY
NO - 1598

NORDIC SWAN ECOLABEL
Printed matter
2041 0731

Printed by Skipnes Kommunikasjon AS

Preface

This thesis is submitted in partial fulfillment of the requirements for the degree of philosophiae doctor (Ph.D.) at the Norwegian University of Science and Technology (NTNU). The research described herein was carried out at the Department of Energy and Process Engineering at the Faculty of Engineering. My main supervisor was Professor Petter Nekså (NTNU/SINTEF Energy Research), Senor Researcher Ph.D. Trond Andresen (SINTEF Energy Research) and Associate Professor Lars O. Nord (NTNU) were my co-supervisors during this work.

This research was a part of the research center HighEFF which aims at reducing the specific energy use and CO_2 emissions from the Norwegian industry. HighEFF is funded by the Research Council of Norway and several industrial partners and I greatly acknowledge their financial support.

This thesis is comprised of an introductory part of six chapters and a collection of scientific papers. Chapter 1 introduces the Rankine cycle and the radial inflow turbine (RIT) and presents the objective and scope of the Ph.D. work. Chapter 2 and Chapter 3 describe the numerical routines and mathematical models that were applied and developed during the Ph.D. They are the building blocks of the novel methods for analyzing Rankine cycles and RITs that are introduced in Chapter 4. Selected results from the Ph.D. case study are presented in Chapter 5. The introductory part ends with Chapter 6, which summarizes the conclusions obtained by the Ph.D. work and proposes several paths for future research. The scientific papers collected in Appendix A and B constitute a major part of this thesis. The reader is referred to them for the details of the proposed methods and the obtained results, and the presentation of the work in the context of the state-of-the-art of scientific literature.

Acknowledgments

I am extremely grateful to my main supervisor Petter and my co-supervisor Trond. Considering our different points of view on the relative importance of numerical details vs practical considerations, Petter, I thank you for your trust by letting me go my own way and backing up my choices in front of others. Instead, our disagreement led to interesting discussions. I was indeed about to get lost in the equations. Luckily, I returned to the *"real world"* when Trond proposed to utilize heat from the metal that is produced at a ferroalloy plant. Many thanks for bringing industrial context to my Ph.D. work, Trond. Completing this Ph.D. thesis was a long journey with several ups and downs. I especially appreciated the support from both of you when I struggled with the motivation. I would also like to thank my co-supervisor Lars for introducing me to your research group and for always helping me whenever I needed it.

This thesis involved a lot of independent work. I will therefore express my deepest gratitude to those I collaborated with during the last three and a half years. Thank you, Monika, for sharing my opinion that science can be both confusing and frustrating, especially before our paper was accepted. I was lucky to be your co-supervisor, Matteo, for your 3 months Erasmus study at NTNU. Your knowledge about turbomachinery, combined with your accuracy and scientific curiosity was very inspiring. Thank you, Geir, for involving me in some of your activities at SINTEF Energy Research. Of particular importance for the progress of my Ph.D. was my colleague, Roberto Agromayor. Our cooperation or your supervision started when I asked a question like "how to make a simple mathematical model of a turbine". Your knowledge of turbomachinery design in particular and natural science in general, and your communication of it, is impressive. I am honored of having you as a co-author on one of the attached papers.

I am also grateful to friends and colleagues at SINTEF/NTNU for the breaks where I could focus on something else than science such as a conversation, a game, a competition, or the adrenaline that appears when being in vertical terrain. Thank you for patiently introducing me to outdoor climbing, Sigurd. Special thanks to Sigurd and Hans Kristian for the company on skis to mountains and with rope to steeper mountains. Our adventures and their preparation were some of the keys that gave me the spirit required to carry out this work.

My last words go to those who are and unfortunately was closest to me. I dedicate the effort put into this thesis to you, Mum. Thank you, Dad, Sindre, and Gaute, for your unconditional support and company. Finally, my dear Sina, without your love and support, I am not sure if I would have been able to complete this work.

Summary

A major fraction of today's electricity is generated by Rankine cycle power systems utilizing the thermal energy of fossil sources such as coal and natural gas, or nuclear energy. However, the carbon content in the fossil energy sources and concern of nuclear radiation are driving forces for adapting the Rankine cycle technology towards other applications. Indeed, solar radiation, geothermal heat, biomass, and industrial surplus heat are regarded as safe and environmentally friendly heat sources for Rankine cycle power systems. A Rankine cycle power system generates electricity using a working fluid circulating between the heat source and a heat sink. In the majority of cases, this working fluid is steam and the power is generated by a steam turbine that is connected to a generator. However, it is challenging to design effective low capacity (below a few MW_e) steam turbines, which is often the case for environmentally friendly heat sources. However, this turbine design challenge can be overcome by instead using an organic substance or CO_2 as the working fluid.

In contrast to steam Rankine cycles whose designs are more or less standardized, the consideration of alternative working fluids leads to many candidates for cycle configuration and component design. This thesis proposed methods to design and analyze Rankine cycles and their major components. The underlying mathematical models are formulated in a general way and combine several engineering disciplines such as applied thermodynamic, heat transfer, and fluid flow. This means that the methods are valid for a large range of operating conditions and working fluid candidates. The mathematical models were also formulated to minimize the computational cost. Indeed, the methods apply an efficient gradient-based optimization algorithm for solving a system of equations *and* optimizing the degrees of freedom simultaneously. The methods also support several novel control approaches that improve the Rankine cycle performance at off-design operating conditions. This means that the methods are especially useful for applications where the characteristics of the heat source or the heat sink vary with time.

The capabilities of the proposed methods were demonstrated for the case of power production from a highly time-dependent heat source at a representative Norwegian ferroalloy plant. This case study considered a heat recovery system that captured, smoothed, and delivered the heat that is released from the process of batch-wise metal casting to a Rankine cycle. Three designs for this Rankine cycle were generated. In addition, the annual electricity production that can be obtained from each of these Rankine cycles was estimated considering four different control approaches. The “standard” sliding pressure control approach yielded an annual electricity production of up to 11.6 GWh. In addition, the annual electricity production can be increased by more than 10% by considering novel control approaches or adjusting the design operating point.

Contents

Nomenclature

Latin symbols

a	Speed of sound	m/s
A_c	Cross-sectional flow area	m^2
A_s	Heat transfer surface area	m^2
b	Blade height	m
c_p	Specific heat capacity of the heat source	J/kg K
C	Absolute flow velocity	m/s
C_0	Spouting velocity	m/s
D_h	Hydraulic diameter	m
e	Specific exergy	J/kg
h	Specific enthalpy	J/kg
I	Rothalpy	J/kg
l	Distance from inlet	m
$\dot{m}$	Mass flow rate	kg/s
$Ma = W/a$	Mach number	-
n	Number of ODE-solver steps	-
o_n	Nozzle throat opening	m
p	Pressure	Pa
P	Perimeter, $P = 4A_c/D_h$	m
Q	Heat transfer rate/duty	W
r	Radial coordinate	m
R	Total thermal resistance per unit length	mK/W
R_f''	Fouling factor	m^2K/W
s	Specific entropy	J/kg K
s	Distance between blades	m
t	Blade edge thickness	m
T	Temperature	K

$U = \omega r$	Blade velocity	m/s
U	Overall heat transfer coefficient	W/m^{2}K
W	Relative flow velocity	m/s
$\dot{W}$	Net power output	W
x	Distance from one end of the heat exchanger	m

Greek symbols

α	Heat transfer coefficient	W/m^{2}K
α	Absolute flow angle	rad
β	Relative flow angle	rad
Δ	Difference	-
$\overline{\Delta T}$	Mean temperature difference	K
Δx	ODE-solver step length	m
η_P	Pump isentropic efficiency	-
η_T	Turbine isentropic efficiency	-
$\eta_{T,calc}$	Isentropic efficiency computed by the RIT model	-
η_{EM}	Electromechanical conversion efficiency	-
η^I	Thermal (first law) efficiency	-
η^I_{rev}	Thermal efficiency of the reversible Rankine cycle	-
η^{II}	Exergy (second law) efficiency	-
ϵ	Convergence criterion	-
ε	Effectiveness	-
$\varepsilon_a, \varepsilon_r, \varepsilon_d$	Clearances (RIT model parameters)	m
ρ	Density	kg/m^3
$\nu = U/C_0$	Velocity ratio	-
ω	Rotational velocity	rad/s
ω_s	Specific speed	-

Subscripts

1,2,…,6	State points within the RIT model
1,2,…,11	Rankine cycle state points (between components)
c	Cold fluid or heat sink
d	Value at the design point
h	Hot fluid or heat source
in	Inlet
min	Minimum value
out	Outlet
th	The throat of the nozzle or the rotor
wf	Working fluid

Abbreviations

GHX	Generic heat exchanger
HX	Heat exchanger
LMTD	Log mean temperature difference
NTU	Number of transfer units
ODE	Ordinary differential equation
PCHE	Printed circuit heat exchanger
PPTD	Pinch point temperature difference
RIT	Radial inflow turbine
SQP	Sequential quadratic programming
VIGV	Variable inlet guide vanes
VRS	Variable rotational speed

Chapter 1 Introduction

1.1 Motivation

Increasing concerns of global warming due to the emission of anthropogenic greenhouse gases have resulted in ambitious climate goals worldwide. For example, the European Union recently increased its ambition to reduce its greenhouse gas emissions by at least 55% within 2030 compared to the emission level in 1990 [1]. One key to reaching this goal is to replace fossil energy, whose utilization emits the greenhouse gas CO_2, with more environmentally friendly heat sources for producing power. Examples of such energy sources are industrial surplus heat [2], biomass [3], solar energy [4], and geothermal energy [5]. These energy sources could provide a significant fraction of the world's power demand [6], but their limited capacity and/or temperature constrain their widespread utilization. First, the use of the steam Rankine cycle [7] is challenging for systems below a few MWe because the combination of small mass flow rate and large volume flow ratio lead to capital intensive expanders with low efficiency [8]. Although the small capacity expander design challenge can be overcome by using an organic fluid [8], [9], or CO_2 [10] as the *working fluid*, the low thermal efficiencies associated with power production from low-temperature heat sources is a challenge for the profitability of any Rankine cycle system. Therefore, a key factor to enable further utilization of environmentally friendly heat sources for power production is to increase the cost-efficiency of Rankine cycle power systems.

1.2 The Rankine cycle and its thermodynamic performance

The Rankine cycle can be defined as a process that converts heat into mechanical work by means of a working fluid. In the single pressure level Rankine cycles depicted in Figure 1.1 the working circulates in a closed loop between the heat source and a heat sink and passes two or three heat exchangers, the pump, and the expander in each loop.

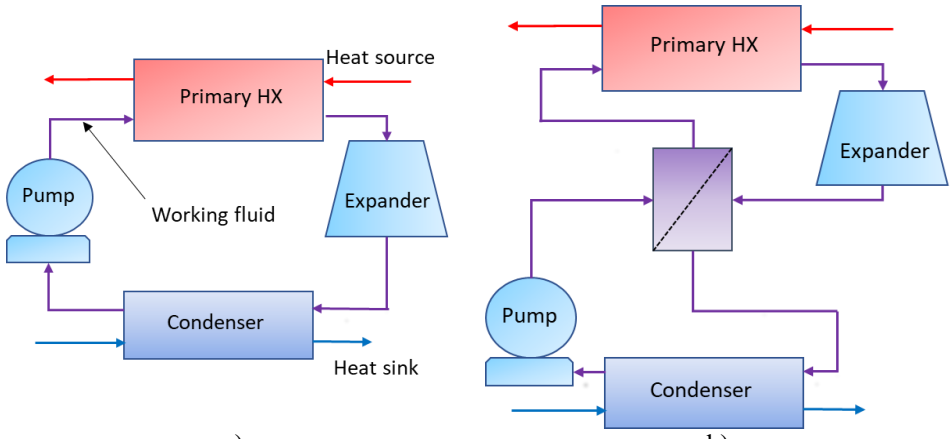

a) b)

Figure 1.1: Illustration of single pressure Rankine cycles: The basic Rankine cycle (a) and the recuperated Rankine cycle (b).

Heat exchangers (HXs) are key components of the Rankine cycle:

- The Primary HX transfers heat from the heat source to the working fluid
- The condenser releases heat from the working fluid to the heat sink which is typically ambient water or air
- The recuperator transfers heat from the expander outlet to the pump outlet, see Figure 1.1(b)

The expander is a key component in which the *enthalpy* (energy related to pressure and temperature) of the working fluid is converted to mechanical energy in terms of a rotating shaft. In heat-to-power applications, this rotating shaft is connected to a generator that produces electricity. The pump is also an important component as it increases the pressure of the working fluid enabling the closed-loop operation.

There are several ways to characterize the thermodynamic performance of a Rankine cycle. Astolfi et al. [11] (p. 185-189) defines the following three indicators of thermodynamic performance:

- Net power output, $\dot{W}$
- Thermal efficiency, also referred to as the first law efficiency, η^I
- Exergy efficiency, also referred to as the second law efficiency, η^{II}

The most obvious of these is the net power output defined as the difference between the power produced by the generator(s) and the power consumed by the pump motor(s). Thermal efficiency is defined as the ratio between the net power output and available heat in the heat source.

$$\eta^I = \frac{\dot{W}}{Q_{h,max}} \tag{1.1}$$

In Eq. (1.1) it is assumed that the heat source has a constant mass flow rate and that $Q_{h,max}$ is the heat released when the heat source is cooled down to its lower temperature limit $T_{h,min}$. If there is no constraint on the heat source temperature, $T_{h,min}$ is equal to the ambient temperature. An alternative and commonly used expression for thermal efficiency

replaces $Q_{h,max}$ with the heat input to the cycle or, equivalently, the Primary HX duty, see Refs. [12]–[14]. However, Astolfi et al. [11] warn against using this expression for performance indication because care must be taken to avoid misinterpretation. Indeed, a Rankine cycle with poor utilization of the heat source has a poor thermodynamic performance that might not be reflected by the ratio between the net power output and the Primary HX duty.

Exergy efficiency is defined as the ratio between the net power output and the available exergy in the heat source.

$$\eta^{II} = \frac{\dot{W}}{\dot{m}_h\left(e_{h,in} - e_{h,min}\right)} = \frac{\dot{W}}{\dot{m}_h \int_{min}^{in} de} \tag{1.2}$$

The specific exergy can be expressed as

$$e = h - h_0 - T_0(s - s_0), \tag{1.3}$$

where the subscript 0 indicates ambient conditions. The *infinitesimal* exergy difference or the exergy *differential* can be obtained by differentiating Eq. (1.3) with respect to h and s:

$$de = \left(\frac{\partial e}{\partial h}\right) dh + \left(\frac{\partial e}{\partial s}\right) ds = dh - T_0 ds. \tag{1.4}$$

The integral in Eq. (1.2) requires the following two assumptions of the heat source fluid to yield a well-known analytical solution [11].

1. Negligible variation in the specific heat capacity with temperature.
2. Negligible pressure drop in the Primary HX.

In this case, $dp = 0$ leading to expressions for the enthalpy and entropy differentials that can be integrated analytically since c_p is assumed constant:

$$dh = \left(\frac{\partial h}{\partial T}\right)_p dT + \left(\frac{\partial h}{\partial p}\right)_T dp = c_p dT \tag{1.5}$$

$$ds = \left(\frac{\partial s}{\partial h}\right)_p dh + \left(\frac{\partial s}{\partial p}\right)_h dp = \frac{dh}{T} = \frac{c_p dT}{T}, \tag{1.6}$$

Indeed,

$$\int_{min}^{in} de = c_p \int_{min}^{in} \left(1 - \frac{T_0}{T}\right) dT = c_p \left[\left(T_{h,in} - T_{h,min}\right) - T_0 \ln \frac{T_{h,in}}{T_{h,min}}\right]. \tag{1.7}$$

Combining Eq. (1.2) with Eq. (1.7) and using $Q_{h,max} = \dot{m}_h c_p \left(T_{h,in} - T_{h,min}\right)$ yield the following expressions for the exergy efficiency:

$$\eta^{II} = \frac{\dot{W}}{Q_{h,max}\left[1 - \frac{T_0}{T_{h,in} - T_{h,min}} \ln \frac{T_{h,in}}{T_{h,min}}\right]} = \frac{\eta^I}{\eta^I_{rev}} \tag{1.8}$$

Eqs. (1.2)-(1.8) is one way to derive the expression given by Eq. (1.9) for the efficiency of the reversible Rankine cycle, which in the literature is also referred to as the Lorenz efficiency [9], [11].

$$\eta_{rev}^{I} = 1 - \frac{T_0}{T_{h,in} - T_{h,min}} \ln\left(\frac{T_{h,in}}{T_{h,min}}\right) \tag{1.9}$$

This expression requires only the temperature of the heat source for estimating the thermodynamic performance potential of a Rankine cycle. Figure 1.2 demonstrates that the net power output of a Rankine cycle is only a fraction of the available heat and that this fraction is especially low for low-temperature heat sources.

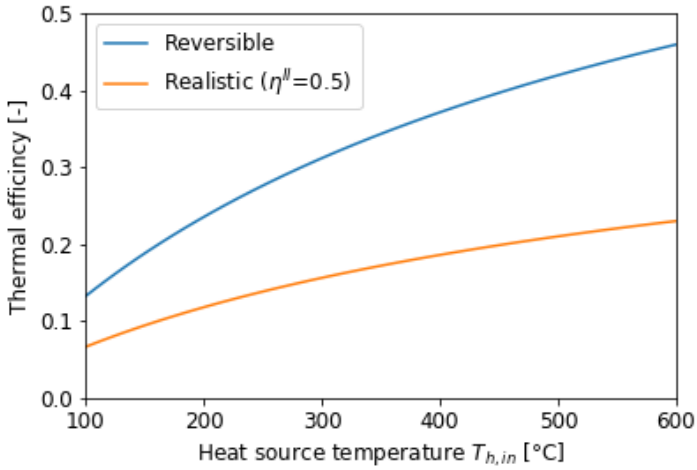

Figure 1.2: Thermal efficiency of the reversible, and a realistic Rankine cycle vs. heat source temperature. The reversible efficiency was computed by Eq. (1.9) using $T_0 = T_{h,min} = 10$ °C.

The difference between the two curves in Figure 1.2 indicates the performance improvement potential for the Rankine cycle. Important sources of irreversibilities in Rankine cycles, and thus sources for performance improvement are [9]:

- Partial utilization of the heat source, i.e., that the Primary HX cools down the heat source to a temperature higher than $T_{h,min}$
- The temperature difference between the hot and cold fluids in the HXs
- Fluid pressure drop in the HXs
- Entropy production in the expander and the pump
- Electromechanical conversion

1.3 Objective

The objective of the Ph.D. work is to improve the cost-efficiency of Rankine cycles through modeling and simulation.

1.4 Defining the scope

A relevant question when defining the scope of the thesis work is: How to *define* cost-efficiency? Astolfi et al. [11] (p. 191-196) describe methods for performing techno-economic optimization of Rankine cycles. In this context they present the following three candidates for the techno-economic objective function:

- Maximize the net present value of the project with a constraint on the payback time
- Minimize the Levelized cost of electricity (LCOE)
- Minimize the specific cost (the ratio between the total cost and the net power output)

Hence, the cost-efficiency can be regarded as a compromise between the thermodynamic performance and costs.

Another important question to consider is: How to *improve* the cost-efficiency? One option is to consider *novel architectures* such as adopting zeotropic mixtures as the working fluid or multiple pressure levels. Quoilin et al. [15] suggested in the techno-economic survey from 2013 that either of these architectures could be the next generation of organic Rankine cycles due to their superior thermodynamic performance potential. However, whether they also improve the cost-efficiency depends on the target application due to their potentially increased costs. I want to illustrate this point through their techno-economic comparison with the "standard" basic Rankine cycle using a pure working fluid.

Most heat sources and heat sinks are sensible meaning that their temperature change when heat is added or removed. For such cases, Zeotropic mixtures enable a lower mean temperature difference between the fluids, $\overline{\Delta T}$, in the condenser and the evaporator since their isobaric phase change occurs over a gliding temperature. This is the reason for the superior thermodynamic performance potential of Rankine cycles employing zeotropic mixtures [16]. However, the lower $\overline{\Delta T}$ must be compensated for by a larger heat transfer conductance, also referred to as the UA-value, to transfer the same amount of heat, see Eq. (1.10).

$$Q = UA_s\overline{\Delta T} \tag{1.10}$$

In addition, the degradation of the heat transfer coefficient of zeotropic mixtures during evaporation and condensation is well-known [17]. These two factors contribute to a larger need for heat transfer surface area leading to a larger HX investment cost.

The situation is similar for the multi-pressure level Rankine cycle whose additional components enable a better temperature match between the working fluid and the heat source but leads to a larger investment cost. For this reason, Astolfi [18] (p. 80) suggests multi-pressure level Rankine cycles for applications where the cost of the heat source is large such as deep geothermal reservoirs or other cases where the benefit of obtaining a high exergy efficiency outweighs the additional costs. These are often multi-MW applications. Three pressure level steam bottoming cycles are indeed adopted in modern gas turbine combined cycle power plants [7].

The novel architectures govern the *design* of Rankine cycles. I believe the consideration of Rankine cycle *operation* for cases where the heat source or sink characteristics vary with time yields a clearer path towards improved cost-efficiency. In such cases, the thermodynamic performance at off-design conditions can be improved with little additional cost. Capra and Martelli [19] demonstrated that a design optimization that takes into

account the off-design performance of the Rankine cycle can improve the cost-efficiency of the system with respect to a conventional design approach that only accounts for the system performance at the design point. More specifically, Capra and Martelli [19] applied the two aforementioned methods to design a combined heat and power Rankine cycle and showed that the former resulted in up to 22% higher annual profit than the latter [20].

In addition, the thermodynamic performance of Rankine cycle systems whose design already exists can be increased by adopting a more flexible control approach. For instance, Quoilin et al. [21] demonstrated that a control strategy allowing the evaporating pressure to vary yields better part-load performance compared to the control strategy with this pressure fixed to its value at the design point. In addition, Schuster et al. [22] demonstrated a significant performance improvement potential by equipping the turbine with movable nozzle blades also known as variable inlet guide vanes (VIGV). Finally, Dong et al. [23] demonstrated that the Rankine cycle performance can be improved by regulating the rotational speed of the expander.

Accounting for off-design performance by considering various control approaches requires mathematical models for the Rankine cycle and its components of sufficient accuracy. To avoid an overwhelming modeling and simulation effort, I made a couple of choices with respect to cycle configuration and expander architecture.

The Ph.D. work relies on the single pressure level Rankine cycles. This includes the basic Rankine cycle and the recuperated cycle illustrated in Figure 1.1.

Concerning the HXs, shell and tube (large-scale system) or plate HXs (small-scale systems) are most often applied [15]. A quantitative comparison between these HX technologies for Rankine cycle applications is provided in Ref. [24]. However, other HX technologies are often required for cases when the heat source and/or heat sink is a gas. For example, the air-cooled condenser is applied when water is not available as the heat sink [18] (p. 71). In addition, if the working fluid pressure and/or temperature is high, such as for CO_2 Rankine cycles, the adoption of a more resistant HX technology, such as the printed circuit heat exchanger (PCHE), might be preferred [10]. Considering the variety of HX technology options, the methods developed in this work do not rely on certain HX technologies.

I am not aware of any mathematical model that can predict the expander performance for various operating conditions and rotational speeds without relying on a certain expander architecture. However, the radial inflow turbine (RIT) is a particularly promising expander architecture due to its ease of manufacturing and the ability to accommodate a large pressure ratio within a single stage [25]. In addition, the commercially available option of equipping the RIT with VIGV enables flexible off-design operation [26], [27]. For these reasons, the Ph.D. work relies on the RIT as the expander architecture.

1.5 Scope

The Ph.D. work is limited to the following scope:

- Focus on applications where the characteristics of the heat source or heat sink vary with time
- Focus on improving the Rankine cycle performance at off-design conditions
- Rely on the “standard” single-pressure level Rankine cycle

- Rely on RIT as the expander architecture

1.6 Novel contributions

I focused on developing flexible and robust methods with a low computational cost. Thus, most of the novelties of the Ph.D. work are related to *how* the numerical results were obtained. The contributions of the Ph.D. work to the scientific community can be summarized as

- A new solution procedure for HX models
- A new method to design an RIT
- A new method for predicting the performance of an RIT
- Validation of the underlying RIT model against experimental data
- A new method to design a Rankine cycle
- A new method to optimize the performance of a Rankine cycle
- Design and analysis of a Rankine cycle for a novel heat-to-power system utilizing heat released from the process of batch-wise metal casting

1.7 Main scientific publications

Papers I-IV listed below are the core of the present research and can be found in Appendix A.

Paper I

B. A. L. Hagen, M. Nikolaisen, T. Andresen, "A novel methodology for Rankine cycle analysis with generic heat exchanger models," *Applied Thermal Engineering*, vol. 165, no. 114566, 2020, DOI: https://doi.org/10.1016/j.applthermaleng.2019.114566.

Paper II

B. A. L. Hagen, M. Cavo, T. Andresen, P. Nekså, "Gradient-Based Design Optimization of a Radial Inflow Turbine," in *IIR Rankine 2020 Conference*, 2020.

Paper III

B. A. L. Hagen, R. Agromayor, P. Nekså, "Equation-Oriented Methods for Design Optimization and Performance Analysis of Radial Inflow Turbines," *Energy*, vol. 237, no. 121596, 2021, DOI: https://doi.org/10.1016/j.energy.2021.121596.

Paper IV

B. A. L. Hagen, T. Andresen, P. Nekså, "Equation-Oriented Methods for optimizing Rankine cycles using Radial Inflow Turbine," Submitted to *Energy* January 26. 2022. Accepted for publication April 1. 2022.

1.8 Other scientific publications

During the period of my Ph.D., I coauthored two conference papers and two journal articles. Although none of them are core publications to this work, some of them are of relevance for the Ph.D. work. For example, Paper V describes a dynamic model to analyze a novel heat-to-power system. Indeed, the case study of the Ph.D. project considers the Rankine cycle of this heat-to-power system and relies on the outcome of the dynamic model. Thus, Paper V contains relevant background information which can be found in Appendix B. Moreover, the novel HX solution procedure was applied for solving the HXs described in Paper VI and Paper VIII.

Paper V

T. Andresen, S. Lingaas, B. A. L. Hagen, P. Nekså, "Dynamic Analysis of Energy Recovery Utilizing Thermal Storage from Batch-Wise Metal Casting," in *Rankine 2020 Conference*, 2020.

Paper VI

H. Deng, B. A. L. Hagen, M. Nikolaisen, T. Andresen, "Comparing Three Methods for Design Analyzes of Rankine Cycle for Waste Heat Recovery from Natural Gas Compression," in *Rankine 2020 Conference*, 2020.

Paper VII

Marit. J. Mazzetti, et al., "Achieving 50% weight reduction of offshore steam bottoming cycles," *Energy*, vol. 230, no. 120634, 2021, DOI: https://doi.org/10.1016/j.energy.2021.120634

Paper VIII

R. M. Montanes, G. Skaugen, B. A. L. Hagen, D. Rohde, "Compact Steam Bottoming Cycles: Minimum Weight Design Optimization and Transient Response of Once-Through Steam Generators," *Front. Energy Res.*, 2021, DOI: https://doi.org/10.3389/fenrg.2021.687248

Chapter 2 Background

This chapter gives practical introductions to applied thermodynamic and mathematical optimization, which are the cornerstones for the models and methods developed in the Ph.D. work.

2.1 Thermophysical properties

Rankine cycle models require the use of thermodynamic properties (Table 2.1) and transport properties (viscosity, thermal conductivity, and surface tension), commonly referred to as thermophysical properties. More specifically, the mathematical models described in Chapter 3 consider *state points,* which refer to a physical location in which the numerical values of the thermodynamic properties and possibly also the transport properties are required. The state points can be defined by two thermodynamic properties since the remaining properties can be derived using an Equation of state (EOS) [28].

Table 2.1: Thermodynamic properties considered in this work.

Symbol	Name
T	Temperature
p	Pressure
ρ	Density
a	Speed of sound
h	Specific enthalpy
s	Specific entropy

This is not necessarily an easy task from a numerical point of view. Most EOSs are explicit in density and temperature [28]. This means that once the couple (ρ, T) is known the other thermodynamic properties can be computed by a single evaluation of the EOS. Although vapor-liquid equilibrium (VLE) calculations might be required if the fluid phase is not known a priori, deriving the thermodynamic properties from the couple (ρ, T) is a relatively straightforward procedure [28].

However, in the context of Rankine cycle modeling, the (ρ,T) couple is seldom known a priori. The thermodynamic function calls, also known as flashes, used in the mathematical models contain other couples of thermodynamic properties, see Table 2.2. Such cases require iterations on the EOS to identify the (ρ,T) couple that corresponds to the given input parameters.

Table 2.2: The thermodynamic function calls used to compute the thermodynamic states in the mathematical models.

Input parameters	Computational cost [-]* [28]	Mathematical models applied
(p, T)	2	Rankine cycle, Radial inflow turbine
(p, h)	10	Heat exchanger, Rankine cycle
(p, s)	10	Radial inflow turbine, Rankine cycle
(h, s)	200	Radial inflow turbine

*Approximate computational cost relative to the case with (ρ, T) as input parameters

The models implemented in this work are compatible with any thermophysical library that supports the thermodynamic function calls of Table 2.2. A good thermophysical library has accurate EOSs and transport property models of the fluids under consideration as well as effective and robust routines for handling the iterative processes your thermodynamic function calls require. The simulations performed in the thesis work applied the thermophysical library REFPROP v10.0 [29] to compute the thermophysical properties of most of the involved fluids. The only exception is the heat sink fluid whose thermophysical properties were computed using an in-house model for incompressible water.

2.2 Mathematical optimization

This section introduces the topic of mathematical optimization and the gradient-based optimization algorithm adopted in the methods described in Chapter 4 through an optimization example. The optimization algorithm adopted in this work is NLPQL [30], which is a sequential quadratic programming (SQP) method. SQP is a class of effective optimization methods developed for solving nonlinear optimization problems with both equality and inequality constraints [31].

This section focuses on solving the following optimization problem:

Minimize

$$f(x, y) = \sin(y)\exp[(1-\cos x)^2] + \cos(y)\exp[(1-\sin x)^2] + (x-y)^2 \qquad (2.1)$$

Subject to $-10 \leq x \leq 0$

$-4 \leq y \leq 1.$

The aim of this optimization problem is to find the numerical values of the *independent variables,* x and y, that minimize the value of the *objective function* given by Eq. (2.1).

A contour plot of the objective function including two attempts of solving the optimization problem with NLPQL is shown in Figure 2.1. The only difference in the setup of the two optimization attempts is the *start values* used for the independent variables. However, this resulted that the optimizations converging to different solutions.

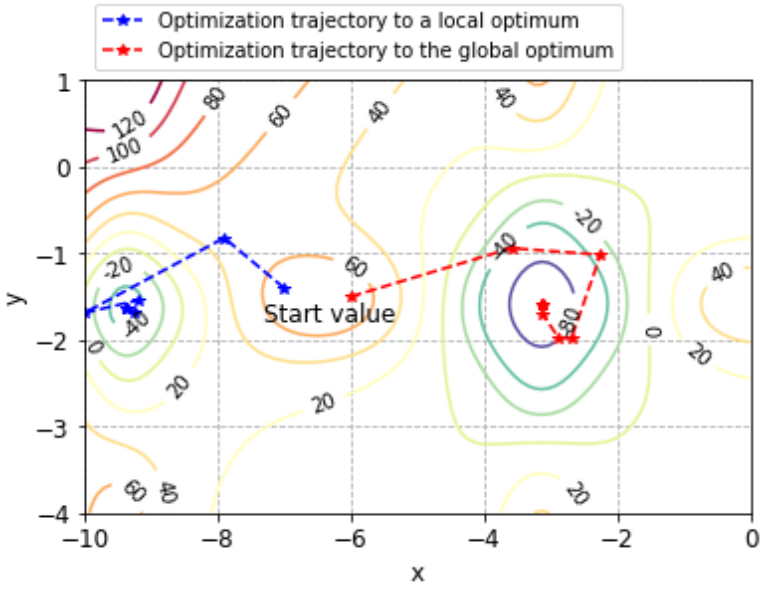

Figure 2.1: Contour plot of the objective function and the trajectory of two optimizations.

The risk of converging to a *local optimum,* illustrated by the blue optimization trajectory in Figure 2.1, is one of the main limitations of gradient-based optimization algorithms. The reason for this is that the gradient-based optimization algorithm doesn't explore the whole domain of the independent variables. Instead, it applies local information (function values and gradients) to search for the next iterate. For example, NLPQL and other SQP methods generate the next iterate by solving a quadratic subproblem [30], [31].

An advantage of gradient-based optimization methods is however that they require relatively few iterations to converge to an optimum leading to a low computationally cost. For example, the optimization examples of Figure 2.1 used only a handful of iterations to converge.

Another limitation of gradient-based optimization algorithms is that a successful convergence to an optimum is only guaranteed when the involved functions are smooth. In the context of mathematical optimization, a function is smooth if its second-order derivatives exist and are continuous [31] (p. 17). Unfortunately, this is not always the case for engineering problems. For example, the smoothness of thermodynamic function calls used in this work, see Table 2.2, could be questioned.

A practical approach for evaluating the suitability of a gradient-based optimization algorithm for solving an optimization problem is to analyze the outcome from several optimizations using different start values for the independent variables. To illustrate the proposed *multi-start* approach, 100 attempts of solving the optimization problem defined by Eq. (2.1) were carried out with NLPQL using the variable start values indicated in Figure 2.2. The outcome of the corresponding optimizations is indicated with a diamond-shaped marker of the same color. Since the objective function is smooth it was not a big surprise that all optimizations converged to an optimum. A bit more surprising is that the results

from the optimizations were distributed over four different optima indicating that there exist at least 3 local optima in addition to the *global optimum* indicated by the red diamond-shaped marker.

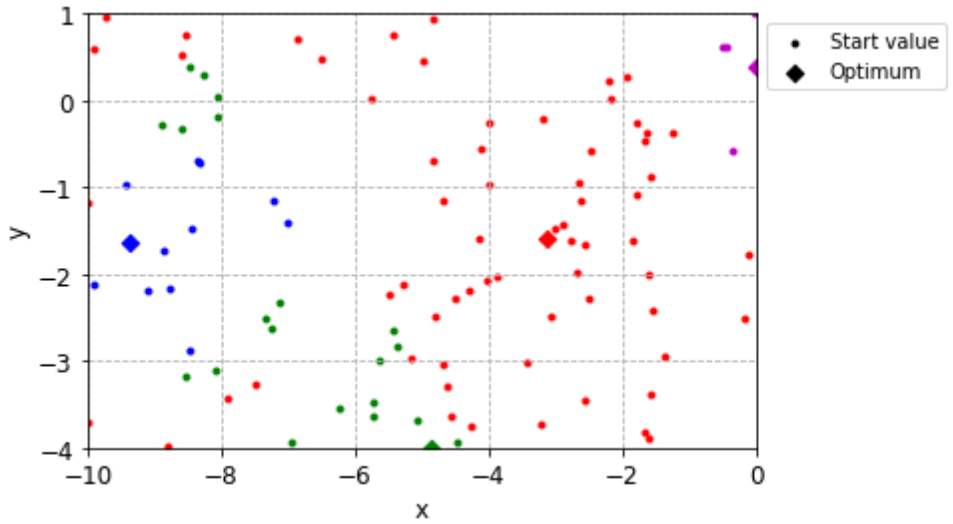

Figure 2.2: Start values for the independent variables (small markers) and the outcome of the optimization (the large diamond-shaped marker of the same color).

Similar multi-start approaches were carried out for the methods presented in Chapter 4. They indicate that the optimization converges to the global optimum with a high probability. The reader is referred to Paper III and Chapter 5 for further details on the robustness of the methods.

Chapter 3 Mathematical models

This chapter describes the mathematical models that were developed and implemented during the Ph.D. work. They are important building blocks for the novel methods described in Chapter 4.

3.1 Generic heat exchanger model

The motivation behind the development of the generic heat exchanger (GHX) model was the need for a HX model of sufficient accuracy without relying on a certain HX technology. Hence, the GHX-model accounts for only the geometry parameters, e.g., hydraulic diameter and cross-sectional flow area, that are used by the heat transfer coefficient- and pressure gradient correlations. The GHX model was first introduced in Paper I and later applied in the case study of the Ph.D. project, see Paper IV and Chapter 5. Although this case study only considered a compact HX with a counter-current flow orientation in a CO_2 Rankine cycle, the GHX model supports any two-fluid HX with a co-current or counter-current flow orientation. Indeed, the GHX model has been used to analyze various HX types in different Rankine cycle applications, see Paper VI, Paper VIII, and Ref. [32].

3.1.1 Model formulation

The GHX model contains three ordinary differential equations (ODEs) describing heat transfer and fluid flow in the HX. The first ODE relates the local heat transfer rate per unit length to the temperature difference between the two fluids.

$$\frac{dQ}{dx} = \frac{T_h - T_c}{R} \tag{3.1}$$

The position coordinate x in Eq. (3.1) refers to the distance from one end of the HX and the local thermal resistance per unit length, R, is computed using the outcome of the heat transfer correlations.

$$R = \frac{1}{\alpha_c P_c} + \frac{R''_{f,c}}{P_c} + r_w + \frac{R''_{f,h}}{P_h} + \frac{1}{\alpha_h P_h} \tag{3.2}$$

The fouling factors $R''_{f,c}, R''_{f,h}$ in Eq. (3.2) can be used to account for fouling thermal resistance. Tables with values for the fouling factor, e.g., Ref. [33] (p. 674) and Ref. [34] (p. 400), indicate that fouling thermal resistance depends on the fluid type and velocity. Moreover, since fouling is caused by impurities or other reactions between the fluid and the wall material, the fouling factor also depends on the length of service of the HX [33] (p. 673). The parameter r_w can be used to account for thermal resistance by conduction through the HX material. It depends on the thermal conductivity of the HX material, the HX geometry and the distance between surfaces in contact with the hot and the cold fluid but is usually much smaller than the other resistances [34] (p. 399). For simplicity, the

fouling and conduction thermal resistances were neglected in the PhD case study by setting $r_w = R''_{f,c} = R''_{f,h} = 0$.

The two remaining ODEs relate the change in pressure of the cold and hot fluids per unit length with the outcome of the pressure gradient correlations.

$$\frac{dp}{dx} = \pm\left(\frac{dp}{dl}\right)_{corr} \tag{3.3}$$

The $\pm$ sign in Eq. (3.3) emphasizes that the pressure can either increase or decrease when moving through an HX in one direction with a counter-current flow orientation.

3.1.2 The novel solution procedure

The analytical solution to Eq. (3.1) can be used to derive the well-known LMTD- and ε-NTU methods [33] (p. 675-694). However, this solution relies on the assumption that both the specific heat of the fluids and R are constant, see e.g. Ref. [33] (p. 677) or Ref. [34] (p. 409). Unfortunately, this is not the case for Rankine cycles whose working fluid may undergo two-phase change processes (condensation and evaporation) and may be operated close to the critical point where the properties vary much. To illustrate this, the numerical values of the specific heat capacities, R, and pressure gradients in two of the HXs presented in Chapter 5 are shown in Figure 3.1 and Figure 3.2.

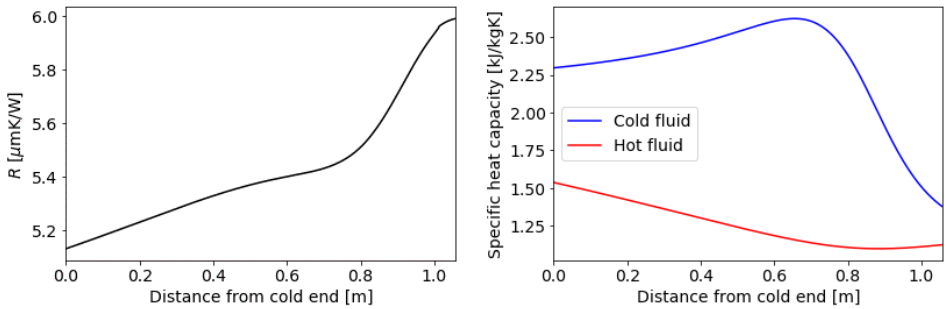

a) b)

Figure 3.1: Outcome of the GHX model: Thermal resistance per unit length (a) and specific heat capacity of the fluids (b) in the recuperator.

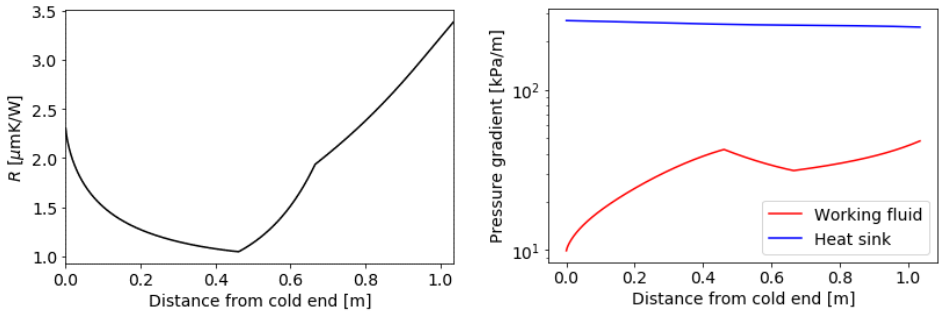

a) b)

Figure 3.2: Outcome of the GHX model: thermal resistance per unit length (a) and fluid pressure gradients (b) in the condenser.

The varying fluid properties indicate that the accuracy of using the LMTD-method or the ε-NTU method in the context of Rankine cycle analysis is questionable. This is, however, not a new observation. For example, Cavallini describes the underlying assumptions of the ε-NTU method in the context of organic Rankine cycles as "*somewhat restrictive*" [34] (p. 419). One approach used to account for variable fluid properties is to discretize the HX and use the LMTD-method or the ε-NTU method for each sub-HX. This approach was recommended in Ref. [10] (p. 233) in the context of CO_2 Rankine cycles and applied in Refs.[35], [36].

The novelty of the GHX model is that the variable fluid properties are accounted for by solving Eqs. (3.1) and (3.3) numerically. Indeed, the GHX model solves the system of ODEs as an *initial value* problem [37] (p. 902-903). This requires that both thermodynamic states at one end of the HX and a stop criterion are defined but enables a once-through calculation procedure. The solution procedure of the GHX model, hereafter referred to as the ODE-solver, starts at the end of the HX where the thermodynamic states of both fluids are defined ($x = 0$) by using the fourth-order Runge-Kutta method [37] (p. 904-905) to move a step Δx towards the other end (in the x-direction). The outcome of this ODE-solver step is the heat transfer rate

$$\Delta Q = \pm \dot{m}_j \Delta h_j, \quad j = (c, h) \tag{3.4}$$

and the pressure changes Δp_c, Δp_h that occurs over the interval $[0, \Delta x]$. The $\pm$ sign in Eq. (3.4) emphasizes that the enthalpy change can be positive or negative depending on whether the fluid is hot or cold and whether the ODE-solver step is against or along the fluid flow direction. Thus, the enthalpy and pressure of the fluids at $x = \Delta x$ are defined once the ODE-solver step is performed and the remaining thermophysical properties are computed using pressure-enthalpy function calls.

Now the ODE-solver is ready to move further into the HX. The ODE-solver moves step-by-step, as described above, until the stop criterion defining the other end of the HX is reached. The GHX model supports two stop criteria:

- Predefined length, L
- Predefined duty (total heat transfer rate), Q

The predefined L stop criterion was used in Paper I because it enables a simple process of determining Δx and the number of ODE solver steps, n. In Paper I n was predefined and

$$\Delta x = \frac{L}{n}. \tag{3.5}$$

The predefined L stop criterion implicates that the duty is a result of the GHX model.

$$Q = \sum_{i=1}^{n} \Delta Q_i \tag{3.6}$$

However, the duty given by Eq. (3.6) may not agree with the requirement of the Rankine cycle. Indeed, constraints were required to ensure consistent HX duties of the Rankine cycle analyzed in Paper I.

When developing the Rankine cycle design optimization method described in Section 4.3, it was realized that consistent HX duties are known by the Rankine cycle model. Hence, the predefined Q stop criterion was introduced in Paper IV to reduce the complexity of the mathematical problem. In this case, a predefined Δx was used for the first n ODE-solver

steps. When the n[th] step exceeded the predefined duty the length of the last step, Δx_n, was reduced by performing 10 *successive substitutions* (see e.g. Ref. [38] p. 223-224), to ensure a consistent HX duty. Now the length is a result of the GHX model:

$$L = (n-1)\Delta x + \Delta x_n \tag{3.7}$$

The output of the GHX model that is processed to the Rankine cycle model is the pressure drops of the two fluids, L, and the heat transfer surface area

$$A_s = L(P_c + P_h). \tag{3.8}$$

When dealing with derivative-based methods such as NLPQL and Runge-Kutta, it is essential that all functions are *continuous*. However, the outcome from the heat transfer and pressure gradient correlations applied for single-phase and two-phase flow differ at the dew point. This work applied linear interpolations of the outcome of the correlations between vapor quality of 0.8 and the dew point which ensure the continuous transition between single-phase gas and two-phase flow illustrated in Figure 3.3.

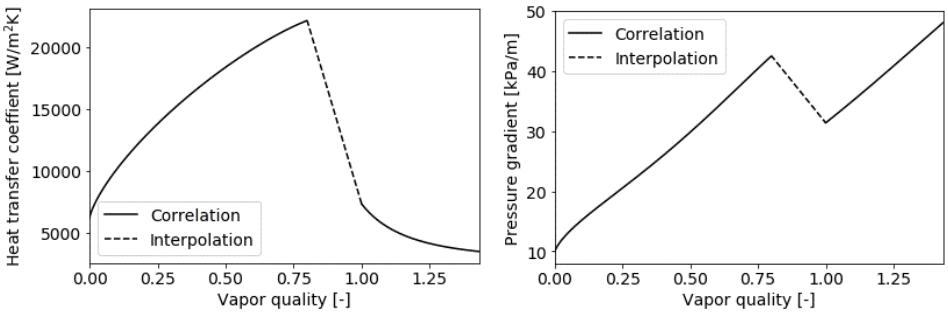

a) b)

Figure 3.3: Outcome of GHX model for the condenser presented in Chapter 5: Working fluid heat transfer coefficient (a) and pressure gradient (b).

The x-axis of Figure 3.3 represents the vapor quality

$$q = \frac{h - h_l}{h_g - h_l}\ , \tag{3.9}$$

where h_l is the saturated liquid enthalpy and h_g is the enthalpy at the dew point.

3.1.3 Numerical performance

The GHX model has a more elegant approach for solving an HX compared to the aforementioned discretization method. The GHX model may also improve the accuracy vs. computational cost trade-off since the numerical error of the fourth-order Runge-Kutta method is proportional to (n^{-4})[37] (p. 895). The results of Figure 3.4 illustrate that the GHX-model converges fast to a consistent solution when n increases. The numerical errors of Figure 3.4 were estimated as the relative deviation between the GHX model output and the corresponding output using n =1000.

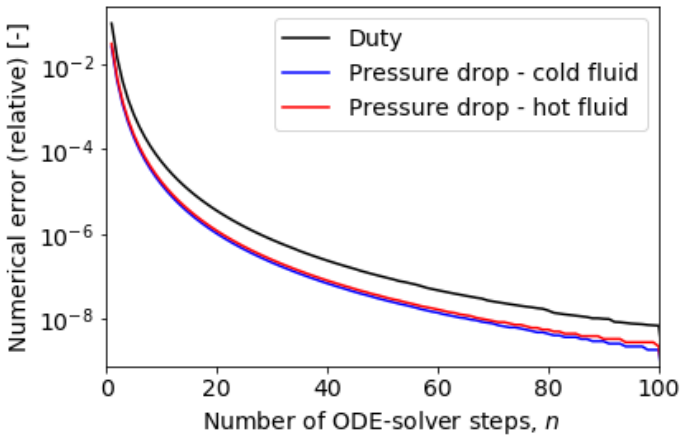

Figure 3.4: Convergency rate of the GHX-model when solving the Primary HX presented in Chapter 5: Numerical error vs. the number of ODE-solver steps.

3.2 The radial inflow turbine model

The mean-line model is arguably the simplest turbine flow model that accounts for geometry and fluid properties. This model assumes that the flow velocity is uniform along the blade span and considers only the main geometric parameters of the turbine, see Figure 3.5 and Figure 3.6. Consequently, the mean-line model can be applied as a first step of the fluid-dynamic turbine design procedure [39], [40]. In this work, a mean-line model was developed for generating the preliminary design of the RIT and predicting its design efficiency and off-design performance.

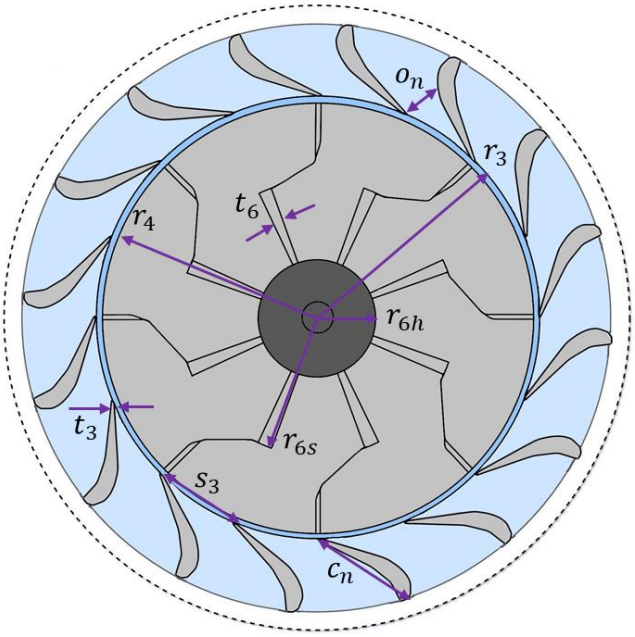

Figure 3.5: Radial-tangential view of the RIT**.**

This RIT model considers velocity triangles and state-points at the inlet, throat, and outlet of the nozzle and rotor, see Figure 3.6. The velocity triangle, see Figure 3.7, consist of three velocities:

1. The absolute velocity, C, is the flow velocity relative to a person standing next to the turbine.
2. The relative velocity, W, is the flow velocity relative to the blade.
3. The blade velocity, U, which is equal to ωr_4 at the entrance of the rotor and $\omega r_{6,RMS}$ at the exit of the rotor.

For the RIT studied in this work, the meridional direction equals the radial inward direction at the nozzle outlet and rotor inlet, while the meridional direction equals the axial direction at the rotor outlet (the meridional direction turns 90° in the rotor). The flow angles α, β are measured from the meridional direction towards the tangential direction. The velocity triangles at the nozzle outlet and rotor inlet are defined by (C, U, α) and the velocity triangles at the rotor outlet are defined by (W, U, β). In both cases, the remaining parameters of the velocity triangles can be computed using trigonometric identities [41]. There are no rotating blades in the nozzle ($U_3 = 0$). Consequently, the velocity triangle at the nozzle outlet is a single vector where $C_3 = W_3$ and $\alpha_3 = \beta_3$.

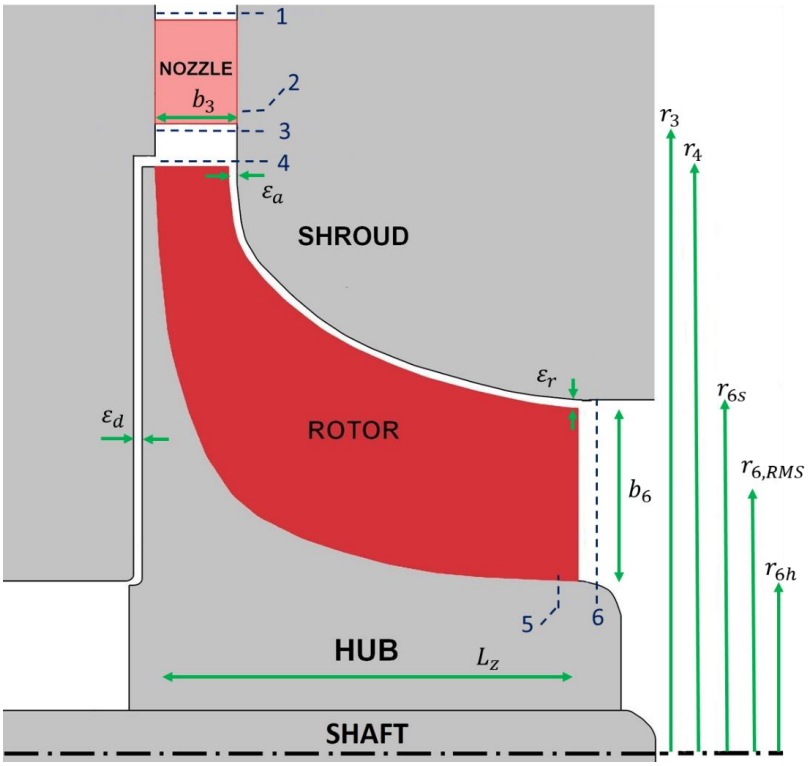

Figure 3.6: Axial-radial view of the RIT.

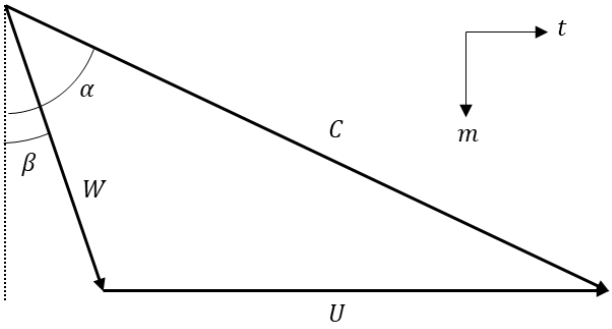

Figure 3.7: Illustration of a velocity triangle in the rotor and the angle convention used in this work.

The velocity triangles can be used to compute the enthalpy distribution. More specifically, the RIT model uses the fact that the rothalpy (Eq. (3.10)) is conserved ([42] (p.11)) to compute the enthalpy at the thermodynamic states.

$$I = h + \frac{1}{2}W^2 - \frac{1}{2}U^2 \tag{3.10}$$

The losses due to irreversibilities within the turbine were estimated by using an empirical loss model. The loss model adopted in this work was proposed by Meroni et al. [43] and considers loss mechanisms in the nozzle and the rotor and the space between them. Moreover, the loss model accounts for supersonic losses when the flow velocity exceeds the speed of sound, which is relevant for high-pressure ratio applications such as Rankine cycles. Meroni et al. [43] also introduced four coefficients to calibrate the loss model. More specifically they adjusted the calibration coefficients using an optimization algorithm to minimize the deviation between experimental data of six high-pressure ratio RITs and corresponding model predictions.

The RIT model supports both the *original* (when the calibration coefficients equal unity) and the *calibrated* loss model of Meroni et al. [43]. The validation of the RIT model against experimental data, see Paper III, showed that the calibrated loss model predicts higher RIT efficiencies than the original loss model. In addition, the cases for which the calibrated loss model agrees better with the experimental are limited to the highest-pressure ratios. Due to the moderate working fluid pressure ratios in case studies of the Ph.D. project, the more conservative *original* loss model was applied for the remainder of the thesis work.

Some RIT geometry parameters are used to compute the cross-sectional flow areas by Eqs. (3.11) and (3.12).

$$A_{c,i} = 2\pi r_i b_3, \quad \mathrm{i} = 3{,}4 \tag{3.11}$$

$$A_{c,6} = \pi(r_{6s}^2 - r_{6h}^2) \tag{3.12}$$

This enables the computation of three mass flow rates by Eq. (3.13).

$$\dot{m}_i = \rho_i A_i W_i \cos\beta_i, \qquad \mathrm{i} = 3{,}4{,}6 \tag{3.13}$$

Most of the geometry input parameters, such as the clearances $(\varepsilon_a, \varepsilon_r, \varepsilon_d)$, rotor axial length L_z and blade trailing edge thicknesses (t_3, t_6), are only used in the loss model.

The reader is referred to Paper III for a complete presentation of the parameters and equations involved in the mean-line model.

3.3 Rankine cycle model

The Rankine cycle model considers the cycle illustrated in Figure 3.8. Two components are added to the basic Rankine cycle illustrated in Figure 1.1(a):

- The recuperator transfers heat from the RIT outlet to the working fluid pump outlet, resulting in a higher working fluid temperature at the cold end of the Primary HX. If the heat source outlet is constrained to a sufficiently large temperature, the inclusion of the recuperator increases the thermodynamic performance potential of the Rankine cycle [36], [44].
- The sink pump increases the pressure of the heat sink pressure with the magnitude of its pressure drop occurring in the condenser. Thus, the inclusion of the sink pump gives a penalty of the sink pressure drop to the thermodynamic performance of the Rankine cycle. The location of the sink pump (downstream of the condenser) has a

numerical reason; the heat sink pressure drop must be computed before the sink pump model can be executed.

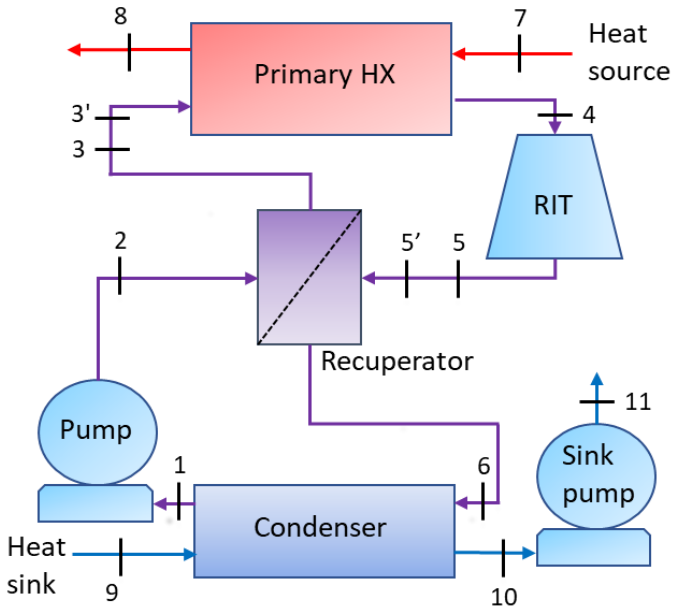

Figure 3.8: Layout of the basic recuperated Rankine cycle and the thermodynamic state points considered in the Rankine cycle model.

The Rankine cycle model governs the thermodynamic *state points* at the inlet and outlet of each of the components of the cycle, indicated by numbers 1-11 in Figure 3.8. The pumps are modeled with a prescribed isentropic efficiency defined by Eq. (3.14).

$$\eta_p = \frac{h(p_{out}, s_{in}) - h_{in}}{h_{out} - h_{in}} \tag{3.14}$$

Furthermore, the RIT isentropic efficiency, defined by Eq. (3.15) is used to compute the outlet of the turbine.

$$\eta_T = \frac{h_4 - h_5}{h_4 - h(p_4, s_5)} \tag{3.15}$$

The HXs of the Rankine cycle model have a counter-current flow orientation and it is assumed that the cold fluid receives all the heat leaving the hot fluid. Hence the HX duty can be expressed as

$$Q = \dot{m}_h\left(h_{h,in} - h_{h,out}\right) = \dot{m}_c\left(h_{c,out} - h_{c,in}\right) \tag{3.16}$$

The enthalpy change in the recuperator is computed using the effectiveness defined as the ratio between duty and maximum achievable duty.

$$\varepsilon = \frac{Q}{Q_{max}} = \frac{h_5 - h_6}{h_5 - h(p_5, T_2)} \tag{3.17}$$

The recuperator can be omitted by setting $\varepsilon = 0$. Hence the Rankine model also supports the basic Rankine cycle. The net power output of the Rankine cycle was computed by Eq. (3.18) which accounts for electromechanical conversion.

$$\dot{W} = \dot{m}_{wf}(h_4 - h_5)\eta_{EM} - \frac{\dot{m}_{wf}(h_2 - h_1)}{\eta_{EM}} - \frac{\dot{m}_c(h_{11} - h_{10})}{\eta_{EM}} \tag{3.18}$$

The physics occurring *within* the HXs and the RIT is in this work accounted for by the GHX-model and RIT model described in the two previous sections. For example, the GHX model predicts the pressure in state points 3, 3', and 5'. The reader is referred to the next chapter for further information on the coupling between the thermodynamic Rankine cycle model and the component models.

Chapter 4 Novel methods

Four methods have been developed during the Ph.D. for designing and analyzing the RIT and the Rankine cycle. Common for these methods is that they consist of a *problem formulation*, a *mathematical model,* and a *gradient-based* optimization algorithm. These building blocks and their interaction are illustrated in Figure 4.1.

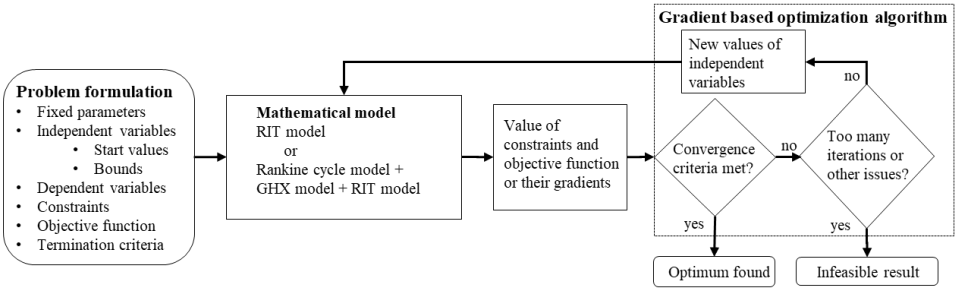

Figure 4.1: Flowchart of the methods used to design and analyze the RIT and the Rankine cycle.

When developing the methodologies, the parameters of the mathematical model were divided into three categories.

1. The *fixed parameters* are predefined by the user and do not change during the optimization.
2. The *independent variables* are adjusted by the optimization algorithm to find the numerical values that optimize a certain objective function subject to constraints.
3. The *dependent variables* are computed using the independent variables and fixed parameters and they include the objective function and constraints.

The optimization process starts by executing the mathematical model using the numerical values of the fixed parameters and the start values for the independent variables as input. After that, the numerical values for the constraints and the objective function (outcome of the mathematical model) are transferred to the optimization algorithm. The optimization algorithm will then send a new set of values for the independent variables back to the mathematical model. As the optimization algorithm also relies on gradient information it may request numerical values for the gradients of the objective function and the constraints to be returned. As indicated in Figure 4.1, this iterative procedure is repeated until the convergency criterion is met, or until the maximum number of iterations is exceeded.

The following sections introduce each of the methods for RIT design optimization, RIT performance analysis, and Rankine cycle design- and performance optimization. More specifically, they explain the capabilities and highlight the novelties of the methods. The reader is referred to Paper III and Paper IV for comprehensive coverages of the methods,

including the independent variables, fixed parameters, and equations used to compute the constraints and the objective function.

4.1 The RIT design optimization method

The RIT design optimization method can be used to generate the preliminary geometry that maximizes the design point RIT isentropic efficiency. The design point is defined by the inlet state, outlet pressure, and the working fluid mass flow rate and are consequently fixed parameters as indicated in Figure 4.2. The optimization objective is to maximize the total-to-static isentropic efficiency

$$\eta_{T,calc} = \frac{h_{in} - \left(h_{out} + \frac{1}{2}C_{out}^2\right)}{\Delta h_{is}}. \tag{4.1}$$

This objective function was selected because it is assumed that the kinetic energy leaving the rotor outlet, $\frac{1}{2}C_{out}^2$, is not recovered. The independent variables govern geometry- and velocity triangle parameters, and the entropy distribution and include the specific speed and the velocity ratio.

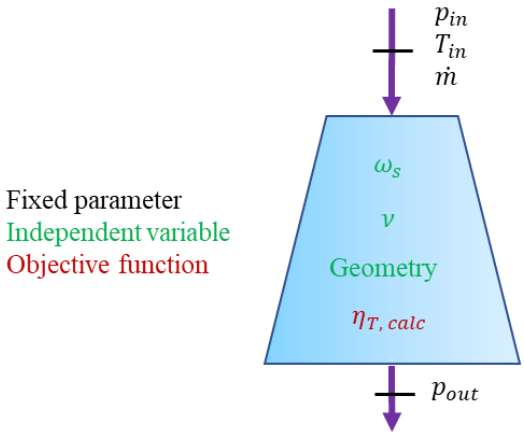

Figure 4.2: Overview of the RIT design optimization problem formulation.

An advantage of the chosen set of independent variables is that the computation of the remaining dependent variables is relatively straightforward. First, the isentropic enthalpy change, $\Delta h_{is} = h_{in} - h(p_{out}, s_{in})$, is computed using the fixed inlet state and outlet pressure. This enables the calculation of the spouting velocity, $C_0 = \sqrt{2\Delta h_{is}}$. Thereafter the rotational speed and the rotor radius are computed from the specific speed and velocity ratio variables.

$$\omega = \frac{(\Delta h_{is})^{0.75}}{\left(\dot{m}_{wf}/\rho_5\right)^{0.5}}\omega_s \tag{4.2}$$

$$r_4 = \frac{C_0}{\omega}\nu \tag{4.3}$$

After that, the preliminary RIT geometry is generated using the independent geometry variables and the fixed- and dependent geometry parameters. Once the RIT geometry is described, the explicit equations of the RIT model, such as Eqs. (3.11)-(3.13) and the loss model, are used to compute the remaining dependent variables.

The loss model requires numerical values of the relative velocity at the throat of the blade rows (nozzle and rotor). In the design optimization method, these values are estimated by Eq. (4.4). Hence, the design optimization supports supersonic velocities.

$$W_{th} = \begin{cases} W_{out}, & Ma_{out} < 1 \\ a_{out}, & Ma_{out} \geq 1 \end{cases} \tag{4.4}$$

A novelty of the design optimization method is the use of equality constraints, instead of inner iterations to ensure a consistent solution:

- Three equality constraints are imposed to ensure that the three mass flow rates given by Eq. (3.13) are equal to the design specification
- Two equality constraints are imposed to ensure that the entropy distribution is consistent with the entropy production predicted by the loss model
- One equality constraint is imposed to ensure that the computed turbine outlet pressure equals the design specification

The equality constraints are, together with the objective function, processed by the optimization algorithm in the search for the next iterate. As a result, the RIT model does not have to be solved at each intermediate optimization iteration and the computational cost of the problem is reduced.

4.2 The RIT performance analysis method

The RIT performance analysis method can be used to predict the isentropic efficiency and mass flow rate of an RIT whose design already exists at a given operating condition. This operating condition (design or off-design) is defined by the inlet state, outlet pressure, and rotational speed as indicated in Figure 4.3. There are some notable similarities with the design optimization method as both methods rely on the same RIT model and use the same independent variables related to flow velocities.

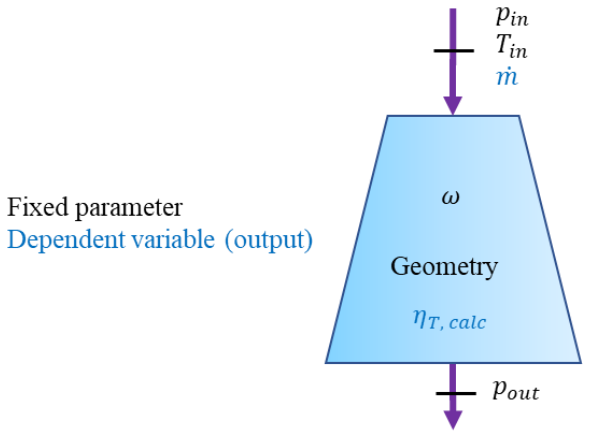

Figure 4.3: Overview of the RIT performance analysis problem formulation.

However, the performance analysis method uses the entropy at the throat of each blade row as an independent variable. This increased complexity is required to ensure physically consistent results in the case when the flow in either of the blade rows is choked. A reliable RIT performance analysis should predict a mass flow rate that increases with pressure ratio (by reducing the outlet pressure) until it converges to a limiting value that corresponds to the case when the flow velocity in either of the blade rows reaches the speed of sound, see Figure 4.4(a,c). At this point, the blade row is choked and a further increased pressure ratio will not affect the mass flow rate, or the thermodynamic states and velocity triangles upstream of the throat [45] (p. 264-265). The additional entropy variables and corresponding constraints ensure that, once a blade row is choked, a further increase in pressure ratio will not affect the thermodynamic state at the throat or any points upstream of the throat. Instead, the additional entropy production due to supersonic losses is assigned at the outlet of the blade row. Thus, both the mass flow rate and the density at the throat in which it depends on remain constant beyond the choking point, see Figure 4.4(a,d).

Seven equality constraints are imposed in the performance analysis method to ensure a consistent solution:

- Two equality constraints to ensure conservation of mass, i.e., that the three mass flow rates given by Eq. (3.13) are equal
- Four equality constraints to ensure that the entropy distribution is consistent with the entropy production predicted by the loss model
- One equality constraint to ensure that the computed turbine outlet pressure equals the specified outlet pressure

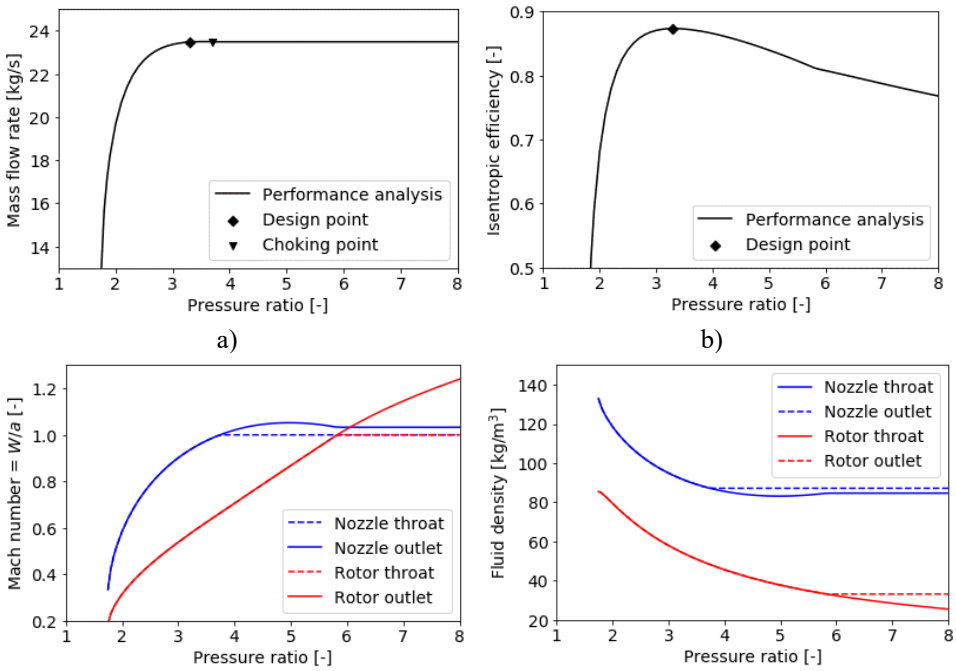

Figure 4.4: Outcome of the RIT performance analysis method using different pressure ratios (by adjusting the outlet pressure). Inlet conditions: CO_2 at 197 bar and 453 °C. The reader is referred to Table 5.3 for the RIT geometry and rotational speed.

The number of independent variables also equals seven. Consequently, the mathematical problem of the RIT performance analysis is a system of nonlinear equations.

The consideration of supersonic velocities is very relevant for RITs in Rankine cycle applications due to their relatively high-pressure ratios [43]. However, choked flow is rarely considered in the RIT performance analysis methods documented in the open literature. Meroni et al. [43] is indeed the only scientific article found that documented the treatment of choked flow in the context of RIT performance analysis. The present RIT performance analysis method introduces a simpler and more elegant treatment of choked flow:

- First, the use of a predefined outlet pressure ensures a unique solution to the problem when the flow in any blade row chokes. In contrast, Meroni et al. [43] used a predefined mass flow rate that requires care to ensure a unique solution; Once the turbine is choked there is an infinite number of values for the outlet pressure that yields the same mass flow rate, see Figure 4.4(a). Thus, Meroni et al. [43] also provided the outlet pressure in the case of a choked turbine to ensure a unique solution.
- Secondly, the use of blade row outlet velocities as independent variables avoids the need for an initial evaluation of whether any blade rows are choked as in Meroni et al. [43]. Instead, the choked flow calculation procedure activates every time the blade row outlet velocity is supersonic. In such cases, the thermodynamic state and the velocity at the throat of the blade row are computed by successive substitutions

until convergence ($\epsilon = 10^{-10}$), see the upper part of Figure 4.5. However, whether the blade row actually chokes depends solely on the magnitude of Ma_{out} at the last iteration before a feasible solution is found.

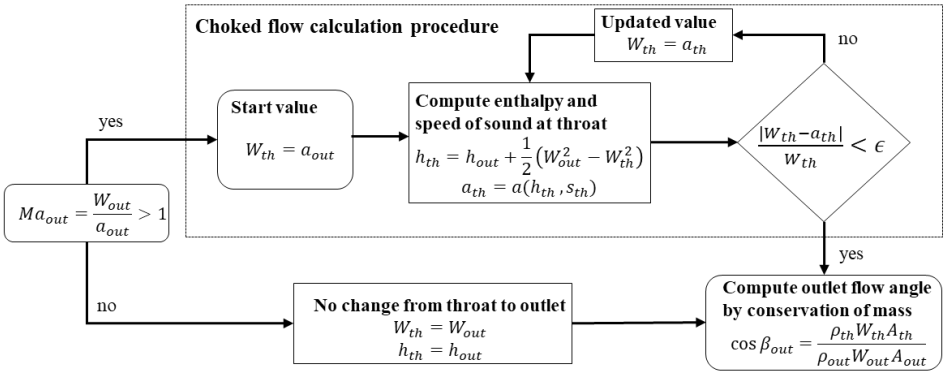

Figure 4.5: Method used to compute the relative velocity and thermodynamic state at the throat and the outlet flow angle of a blade row (nozzle or rotor) in the RIT performance analysis method.

4.3 The Rankine cycle design optimization method

The Rankine cycle design optimization method can be used to generate the preliminary design of the HXs and the RIT that maximizes the performance of a Rankine cycle at the design point. More specifically, the objective function to be maximized is the net power output and the design point is defined by the characteristics of the heat sink and heat source as indicated in Figure 4.6. The application for which the Rankine cycle optimization methods were demonstrated, see Chapter 5, governed indirect heat recovery from an industrial process. Thus, the heat source outlet temperature, T_8 in Figure 4.6, was assigned a fixed value according to the specification of the heat recovery system. For other cases such as when the heat source is not in a closed-loop, T_8 should be considered as an independent variable.

A pure thermodynamic model is often used in Rankine cycle design optimizations. In this case, the resulting optimization problem has few independent variables because the HXs can be defined by pinch point temperature differences (PPTDs), and the expander can be defined by an isentropic efficiency, see Paper I or Ref. [11]. Moreover, the preliminary design of the HXs and the RIT can be generated by subsequent component design procedures, such as using the RIT design optimization method introduced in Sec 4.1. One example of this approach can be found in Ref. [35]. However, this approach may yield suboptimal or inconsistent results. Song et al [12] proposed using a mean-line RIT model during the Rankine cycle design optimization and demonstrated that the RIT isentropic efficiency strongly depends on the working fluid. Moreover, using HX geometry parameters as independent variables in the Rankine cycle design optimization ensures optimal allocation of heat transfer surface area and optimal compromise between fluid pressure drop and PPTD in the HXs, see Paper I and Ref. [36]. I believe that the present

Rankine cycle design optimization method is the first using HX- *and* RIT geometry parameters as independent variables.

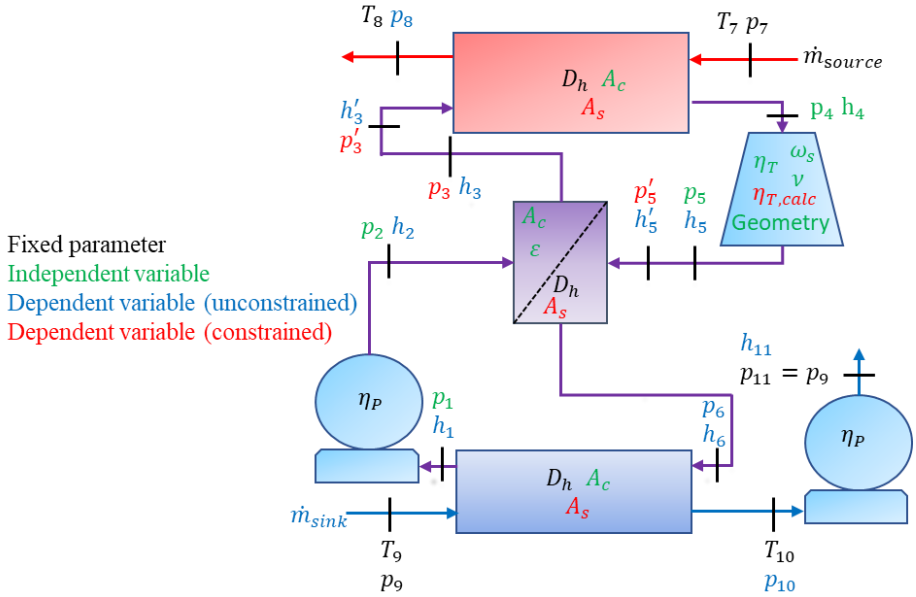

Figure 4.6: Overview of the Rankine cycle design optimization problem formulation.

The set of independent variables and fixed parameters yield a relatively straightforward procedure for generating the dependent variables indicated in Figure 4.6. First, state point 1 is computed as saturated liquid and the enthalpies (h_2, h_5, h_5') are computed using the definitions of the isentropic efficiency given by Eqs. (3.14) and (3.15). After that, the inlet enthalpies to the recuperator are defined, and its outlet enthalpies (h_3, h_3', h_6) are computed using the recuperator effectiveness. Thereafter, the conservation of energy in the HXs is used to compute the mass flow of the working fluid and the heat sink.

$$\dot{m}_{wf} = \frac{(h_7 - h_8)}{(h_4 - h_3)}\dot{m}_h \tag{4.5}$$

$$\dot{m}_c = \frac{(h_6 - h_1)}{(h_{10} - h_9)}\dot{m}_{wf} \tag{4.6}$$

Now, the duty and the thermodynamic states at one end of each HX are defined enabling executing the GHX model. More specifically, the Primary HX is solved from the hot to the cold end, and the recuperator and condenser are solved from the cold to the hot end using the ODE-solver described in Subsection 3.1.2. This enables the computation of the pressures, $(p_3, p_3', p_5', p_6, p_8, p_{10})$, and the heat transfer surface areas by Eq. (3.8). Thereafter the RIT model is executed similarly as described in Section 4.1. This enables the computation of the RIT isentropic efficiency by Eq. (4.1).

The Rankine cycle design optimization method takes advantage of equality constraints to ensure that the Rankine cycle model is consistent:

- Two equality constraints are imposed to ensure that $p_3 = p_3'$ and $p_5 = p_5'$.
- One equality constraint is imposed to ensure $\eta_T = \eta_{T,calc}$, i.e., that the value of the RIT isentropic efficiency variable equals the predicted value of the RIT model.

Constraint(s) must be imposed to avoid oversized HXs. In this work, an inequality constraint was imposed to limit the sum of the heat transfer surface areas of the HXs below a certain value.

Previous Rankine cycle design optimization methods couples RIT model and the Rankine cycle model using iteration(s) [12], [13], [46]. This means that the RIT model is solved within each evaluation of the Rankine cycle model. In contrast, the present Rankine cycle design optimization method includes the RIT model by means of equality constraints:

- Three equality constraints are imposed to ensure that the three mass flow rates given by Eq. (3.13) are equal to the working fluid mass flow computed by Eq. (4.5).
- Two equality constraints are imposed to ensure that the entropy distribution within the RIT is consistent with the entropy production predicted by the loss model.
- One equality constraint is imposed to ensure that the computed RIT outlet pressure equals p_5.

These equality constraints are analogous to those of the RIT design optimization method described in Section 4.1 and ensure that the RIT model is consistent. Moreover, all constraints are processed by the optimization algorithm meaning that neither the Rankine cycle model, nor the RIT model must be solved at each intermediate optimization iteration, leading to a low computational cost.

4.4 The Rankine cycle performance optimization method

The Rankine cycle performance optimization method can be used to predict or maximize the performance of a Rankine cycle whose design already exists. Consequently, the geometry of the HXs and the RIT geometry is solely defined by the fixed parameters, see Figure 4.7. Otherwise, there are some notable similarities between the Rankine cycle design- and performance optimization methods; Both methods use the same independent variables related to cycle state points and component efficiencies, and their underlying Rankine cycle- and GHX models are identical. Moreover, the set of equality constraints from the Rankine cycle design optimization methods is also applied in the present performance optimization method.

However, the HX lengths defined by the fixed parameters are not necessarily equal to the corresponding outcome of the GHX model. In addition, the Rankine cycle performance optimization method takes advantage of the novel treatment of choked flow described in Section 4.2. This ensures that the method is valid for supersonic flow velocities within the RIT but requires a higher resolution on the entropy distribution within the RIT. For these reasons the following *additional* equality constraints are imposed in the Rankine cycle performance optimization method to ensure a consistent solution:

- Three equality constraints to ensure consistent lengths of the GHX model.

- Two constraints to ensure consistent entropies at the throat of the blade rows in the RIT model.

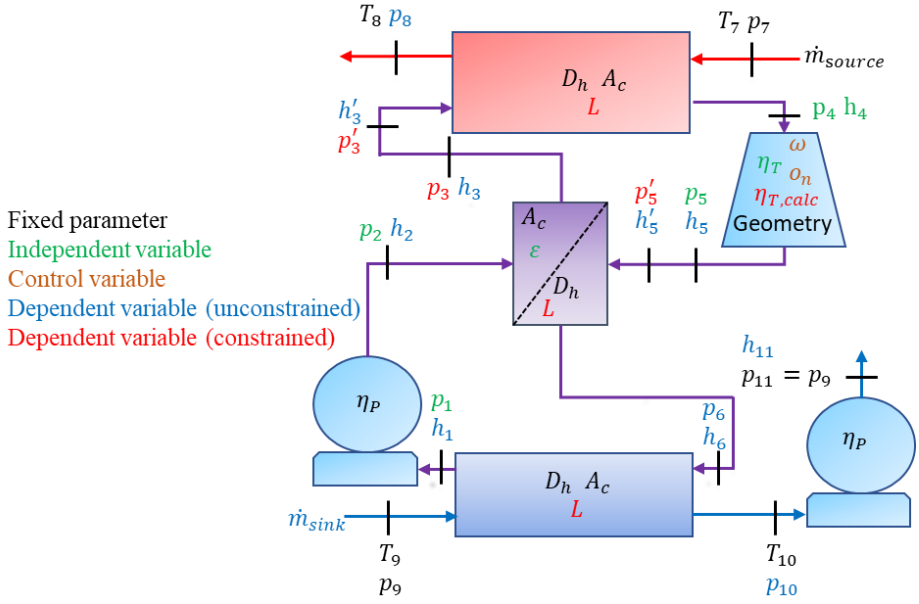

Figure 4.7: Overview of the problem formulation for the Rankine cycle performance optimization method.

The control variables indicated in Figure 4.7 enable a selection of four control approaches:

- The *sliding pressure* control approach occurs when both control variables are fixed parameters. This is a common approach for controlling Rankine cycles and involves changing the turbine inlet pressure to balance system parameters such as the working fluid mass flow rate [14].
- The variable rotational speed (VRS) control approach occurs when the turbine rotational speed is an independent variable while the nozzle throat opening is a fixed parameter. VRS assumes that the turbo-generator system can deliver electric power at the grid frequency despite the variable RIT rotational speed. This can be achieved by using a high-speed generator and a flexible frequency converter system adjusting the frequency of the produced power to the grid frequency [23].
- The variable inlet guide vane (VIGV) control approach occurs when the nozzle throat opening is an independent variable, and the RIT rotational speed is a fixed parameter. VIGV assumes that the RIT is equipped with movable nozzle blades, also referred to as VIGV, that modify the nozzle throat opening by rotating around a pivot point [26], [27].
- In the fourth control approach, in this work referred to as “VRS and VIGV”, both the nozzle throat opening, and the rotational speed are independent variables.

The present Rankine cycle performance optimization method can be regarded as a continuation of the work by Du et al. [14], who considered a constant pressure-, the sliding pressure-, and the VIGV control approaches for a *Kalina cycle* using an RIT. At least, I

believe the present performance optimization method is the first that considers the VRS and the “VRS and VIGV” control approaches for Rankine cycles using RIT

Chapter 5 Case study

This chapter demonstrates the capabilities of the Rankine cycle optimization methods through the design and performance prediction of a Rankine cycle. The application is the utilization of industrial surplus heat, and the industrial facility is a representative Norwegian ferroalloy plant with an annual ferrosilicon production of 100 000 tons. *Three* Rankine cycles were designed and analyzed for this application. This chapter presents selected results from *one* of them and the reader is referred to Paper IV for the remaining results.

5.1 The heat recovery system

The industrial process under consideration is batch-wise metal casting. Each "batch" consists of an amount of liquid metal that is distributed into multiple molds in which it solidifies and cools down to ambient temperature. The latent and sensible heat that is released in this process is significant but seldom utilized [47]. However, a concept for capturing and utilizing this heat is proposed, see Paper V. This heat recovery system consists of a cooling tunnel in which heat from the molds is transferred to a heat transfer fluid (HTF), thermal energy storage to smooth temperature variations, and a Rankine cycle as illustrated in Figure 5.1.

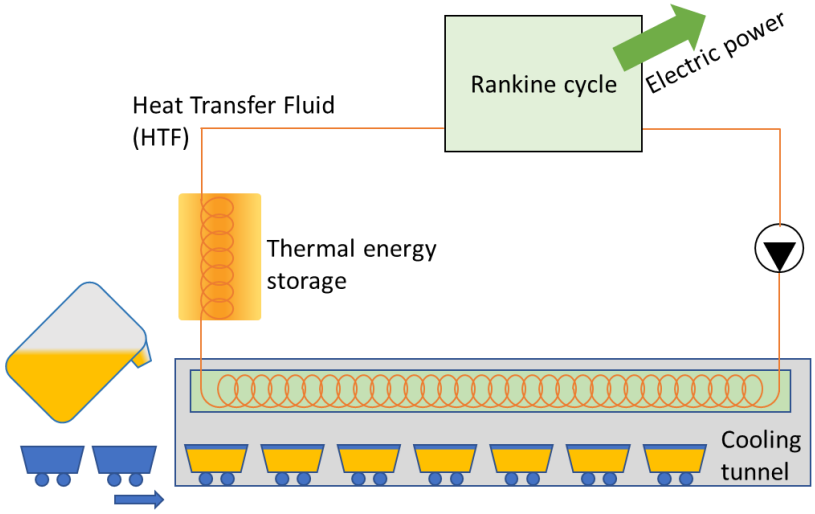

Figure 5.1: Concept diagram of the heat recovery system.

A dynamic model of the heat recovery system was used to generate the HTF characteristics over one hour at the inlet and outlet of the Rankine cycle that is shown in Figure 5.2. The

heat recovery system operates at a cyclic-steady state, meaning that the process depicted in Figure 5.2 repeats itself every hour. In the first half an hour, molds containing liquid metal enter the cooling tunnel one by one as illustrated by the stepwise increase in the HTF temperatures and the Primary HX duty. In the second half an hour there is no further heat input to the cooling tunnel and the heat delivered to the Rankine cycle is mainly provided by the thermal energy storage, illustrated by the constantly decreasing HTF temperatures. The reader is referred to Paper V for more details on the heat recovery system and the above-mentioned dynamic model.

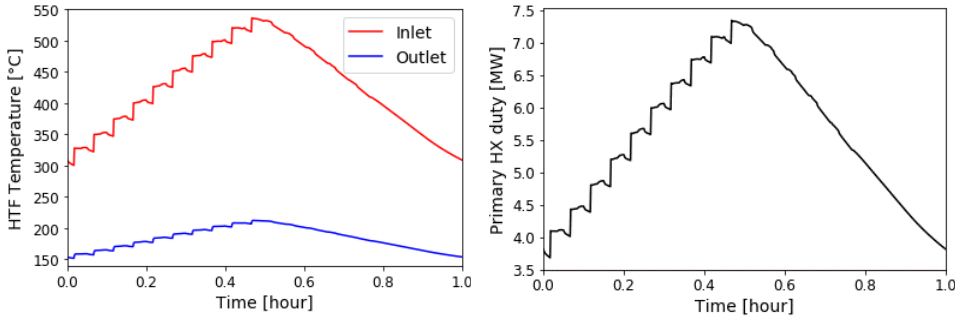

a) b)

Figure 5.2: Outcome of the dynamic model described in Appendix C: HTF temperatures at the inlet and outlet of the Rankine cycle (a) and the resulting Primary HX duty (b).

5.2 Optimization setup

The Ph.D. work focused on the Rankine cycle by considering the HTF as the heat source. More specifically, the Rankine cycle design optimization presented in this chapter used the heat source temperatures indicated by the design point marker in Figure 5.3, whereas the subsequent performance optimizations also considered the off-design points indicated by red markers. Other fixed parameters including the remaining heat source characteristics, the heat sink characteristics, and prescribed efficiencies are shown in Table 5.1.

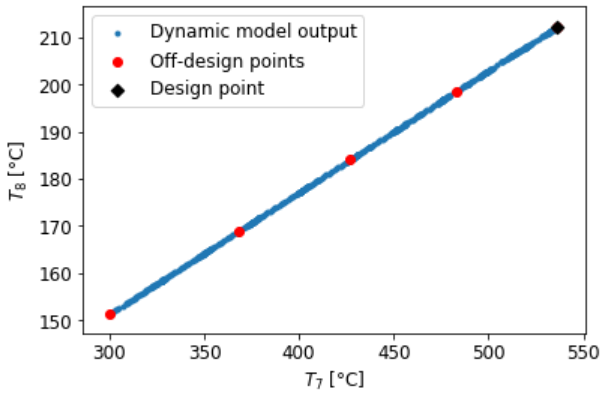

Figure 5.3: HTF temperatures at the inlet and outlet of the Primary HX.

Heat source temperatures above 500 °C limit the number of working fluid candidates due to thermal stability issues [48]. CO_2 was chosen as the working fluid because it can tolerate high temperatures and the relatively low-pressure ratio across the expander that can be handled by an RIT. Indeed, the single-stage RIT is regarded as a suitable expander architecture for CO_2 Rankine cycles of a few MW_e [49].

Table 5.1: Fixed parameters for the Rankine cycle optimizations.

HTF medium	CO_2
HTF mass flow rate	18.2 kg/s
HTF pressure, p_7	200 bar
Heat sink medium	Water
Heat sink inlet temperature, T_9	10 °C
Heat sink outlet temperature, T_{10}	20 °C
Working fluid medium	CO_2
Maximum working fluid pressure	200 bar
Hydraulic diameter, D_h	1.2 mm
Total heat transfer surface area	500 m^2 *
Pump efficiency, η_p	0.65
Electromechanical efficiency, η_{EM}	0.95

*Only relevant for design optimization

Compact HXs such as PCHE, Plate fin, or other HXs with microtubes are suggested for CO_2 Rankine cycles due to their high operating pressure [50]. A theoretical study that accounted for the turbomachinery design demonstrated that the working fluid pressure that maximized the performance of a CO_2 Rankine cycle to be up to 400 bar [51]. On the other hand, existing CO_2 Rankine cycle prototypes consider much lower working fluid pressures [10]. Considering this discrepancy, an upper bound was set on the working fluid pressure to avoid proposing something unrealizable. The pressure constraint indicated in Table 5.1 was indeed active at both design and off-design conditions. In addition, a low value for the hydraulic diameter was used such that the GHX model represented a generic compact HX. The value in Table 5.1 was used for the channels of both the hot and cold fluid in all HXs. Thus, the perimeter, or the heat transfer surface area per unit length of each channel were computed as

$$P_c = P_h = \frac{4A_c}{D_h}. \tag{5.1}$$

5.3 Rankine cycle design optimization

This section starts by presenting the results from *one* optimization before discussing the robustness and computational cost of the Rankine cycle design optimization method based on the outcome from *multiple* optimizations.

The optimized geometry of the HXs and the RIT is shown in Table 5.2 and Table 5.3, respectively. The reader is referred to Figure 3.5 and Figure 3.6 for visualization of the RIT geometry parameters. Notably, the size and channel geometry of the Primary HX,

recuperator, and condenser differ from each other. Although the HXs are compact, the RIT is much smaller. The diameter of the rotor of the RIT is only 17 cm.

Table 5.2: HX geometry obtained by the Rankine cycle design optimization.

		Primary HX	**Recuperator**	**Condenser**
L	[m]	1.59	1.06	1.04
A_c	[10^{-3} m^2]	12.5	23.7	30.3
A_s	[m^2]	130	164	205

Table 5.3: RIT geometry and rotational velocity obtained by the Rankine cycle design optimization.

Nozzle	r_3	[mm]	88.61
	b_3	[mm]	3.45
	s_3	[-]	28.74
	$o_{n,d}$	[mm]	10.26
	t_3	[mm]	0.46
	c_n	[mm]	38.22
Rotor	r_4	[mm]	86.15
	r_{6s}	[mm]	60.31
	r_{6h}	[mm]	43.25
	ω_d	[kRPM]	40.65
	b_4	[mm]	3.45
	Z_r	[-]	16
	t_6	[mm]	1.72
	$A_{c,5}$	[(cm)^2]	19.98
	L_z	[mm]	25.59
	c_r	[mm]	41.88
	ε_a	[mm]	0.40
	ε_r	[mm]	0.40
	ε_d	[mm]	4.31

The T-s diagram of the Rankine cycle at the design point is shown in Figure 5.4 (a). The relatively low temperature of the heat sink facilitates sub-critical condensation, illustrated by the working fluid line within the phase envelope. Thus, the process depicted in Figure 5.4 (a) can be characterized as trans-critical. Moreover, the relatively large heat source outlet temperature facilitates internal heat recovery. Indeed the use of a recuperator is justified since its duty is of similar magnitude as the Primary HX duty, see Figure 5.2(b) and Figure 5.4(b).

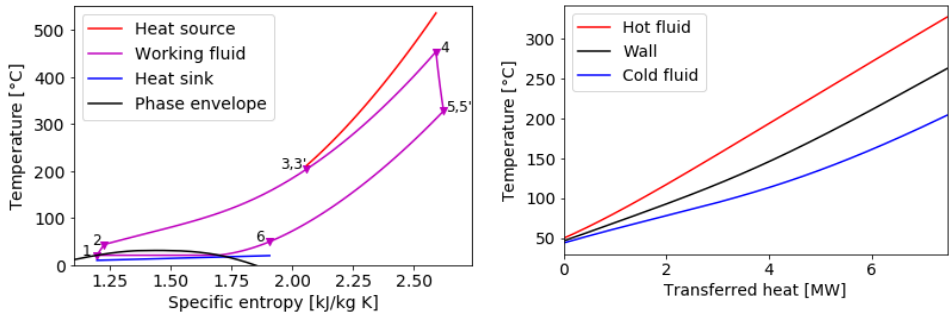

a) b)

Figure 5.4: Cycle T-s diagram (a) and recuperator T-Q diagram (b) obtained by the Rankine cycle design optimization.

Considering the limitations of gradient-based algorithms discussed in Section 2.2 it is impossible to assess the robustness of the Rankine cycle design optimization method based on one successful optimization. Thus, the proposed multi-start approach was carried out. More specifically, 100 design optimizations were carried out using random start values for the independent variables. Only two of these failed to converge to an optimum. This is an indication that the non-smooth functions within the mathematical models are not a major concern to convergency. The objective function value and the execution time obtained on a personal computer with an Intel Core i7-8650U processor from the remaining optimizations are shown in Figure 5.5.

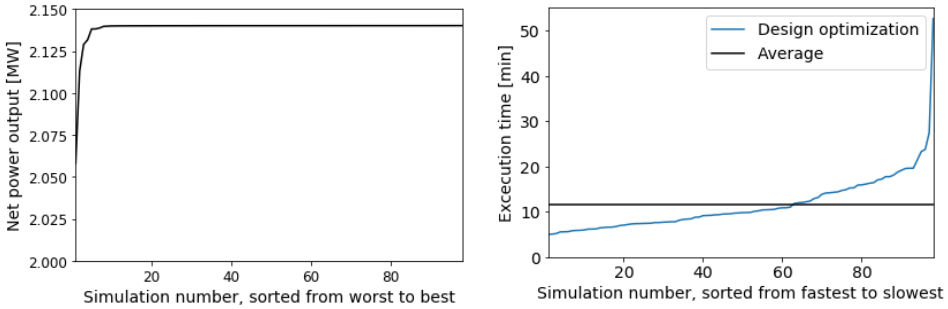

a) b)

Figure 5.5: Outcome from 100 Rankine cycle design optimizations using random start values for the independent variables: Objective function value (a) and execution time (b) from the 98 optimizations that converged to an optimum.

As seen in Figure 5.5(a), most of the optimizations yield almost the same maximized net power output. More specifically, the 88 best optimizations deviate with less than 0.01% in terms of net power output and 2% in terms of optimized values of the independent variables. The consistency in the optimization results is a strong indication that the optimization problem contains few local optima and that the gradient-based algorithm in most cases converged to the global optimum. The average execution time was 11.5 minutes and 53 % of the simulations spent less than 10 minutes to converge, see Figure 5.5(b).

5.4 Rankine cycle performance optimization

The Rankine cycle performance optimizations were carried out using the HX geometry in Table 5.2 and the RIT geometry in Table 5.3 as fixed parameters. Moreover, all four approaches for controlling the Rankine cycle described in Section 4.4 were considered.

The results from the performance optimizations are summarized in Figure 5.6. Each of the plots (a,b,c,d) governs a certain performance metric, whereas each colored line represents a certain control approach. The result from the design optimization is highlighted with a black diamond-shaped marker. Figure 5.6(a) shows that the working fluid mass flow rate decreases when the HTF inlet temperature is reduced from its design value. One option for reducing the turbine mass flow rate is to reduce the pressure ratio across the RIT, see Figure 4.4. Indeed, the sliding pressure and the VRS control approaches react with a lower value for the maximum working fluid pressure at off-design conditions, see Figure 5.6(b).

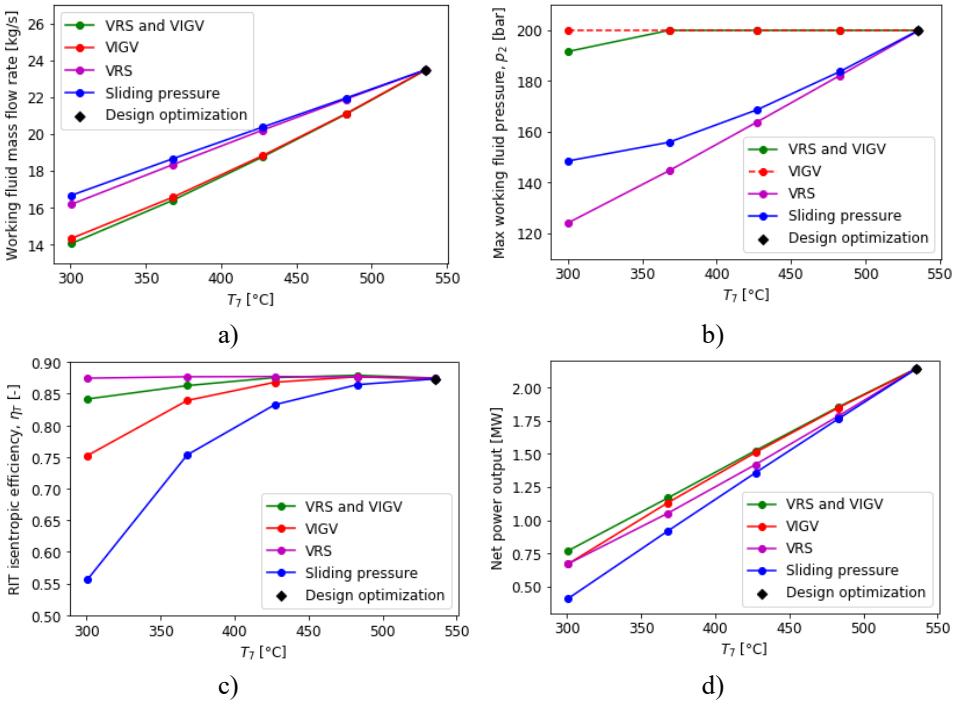

Figure 5.6: Main results from the Rankine cycle performance optimizations.

Alternatively, the mass flow rate may be reduced by reducing the nozzle throat opening [52]. The VIGV and "VRS and VIGV" control approaches react by reducing the nozzle throat opening (Figure 5.7(b)), while p_2 in most cases remains at its upper bound of 200 bar, see Figure 5.6(b). Figure 5.6(c) shows that the turbine isentropic efficiency drops dramatically from the design point value of 87.3% and down to 55.6% for the *sliding pressure* control approach and that the other control approaches improve the off-design RIT efficiency. Notably, the VRS and "VRS and VIGV" control approaches improve the RIT efficiency by reducing the rotational speed, see Figure 5.7(a).

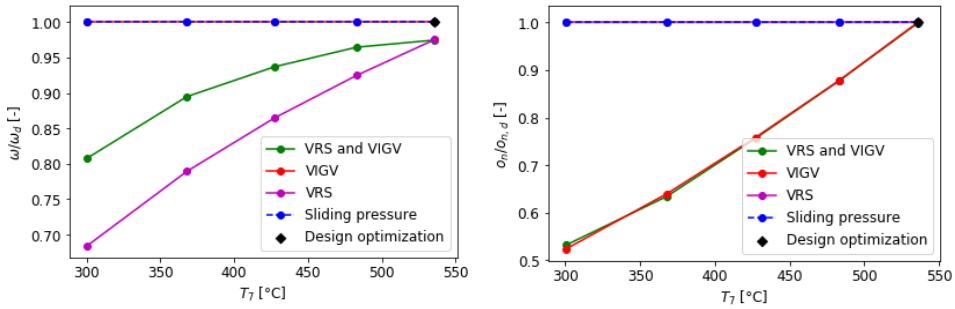

a) b)

Figure 5.7: Optimized values of the control variables obtained by the performance optimizations.

Figure 5.6(d) shows that all control approaches yield similar net power at the design point and that the novel control approaches outperform the sliding pressure control approaches at off-design conditions. T-s diagrams of the Rankine cycle processes at the most off-design operating point are shown in Figure 5.8 to illustrate the impact of each control approach on the process. The poor RIT performance for the sliding pressure control approach is visualized by the relatively large entropy difference (horizontal distance) between state points 4 and 5 in Figure 5.8(a). Moreover, the larger pressure ratio across the RIT for the VIGV control approach results in the relatively low temperature at state point 5 in Figure 5.8(c). Thus, VIGV yields a smaller mean temperature difference in the recuperator than the sliding pressure control approach, see Figure 5.9. Finally, the “VRS and VIGV” control approach utilizes the advantages of both the VRS and the VIGV control approaches and thus has superior thermodynamic performance.

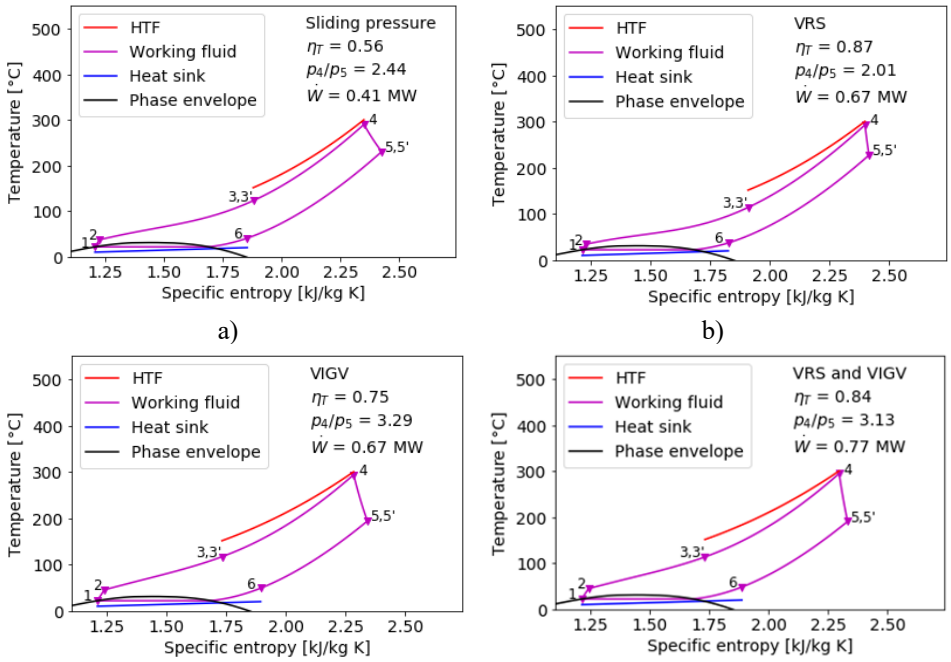

Figure 5.8: T-s diagrams of the Rankine cycle using different control approaches at the most off-design operating point.

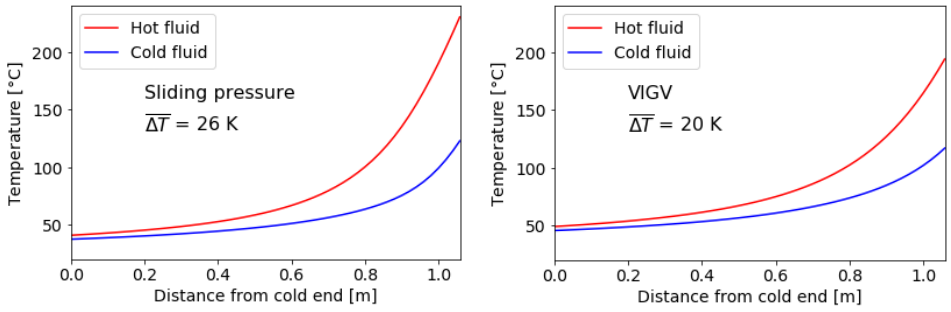

Figure 5.9: Temperature profiles in the recuperator of the Rankine cycle at the most off-design operating point. Sliding pressure control approach (a); VIGV control approach (b).

Chapter 6 Conclusions and further work

6.1 Conclusions

This Ph.D. work proposed a set of methods that can be used to design and analyze HXs and RITs, either as stand-alone components or as a part of a Rankine cycle. The methods are based on mathematical models that account for physics occurring within the RIT and the HXs. More specifically, they apply a library that generates accurate thermophysical properties of the fluids and uses physical principles such as conservation of energy and mass. In addition, the underlying HX model accounts for local heat transfer and pressure gradients using semi-empirical correlations, and the underlying RIT model accounts for irreversibilities using an empirical loss model. Moreover, the RIT model was validated against two comprehensive sets of experimental data. For these reasons, the methods can be used with confidence for performance prediction at both design and off-design operating conditions considering a variety of working fluids. A novelty of the methods is that they take the advantage of an efficient gradient-based optimization algorithm by replacing inner iteration loops with equality constraints. This means that the optimizer both solves a system of equations *and* finds the optimal solution, leading to a low computational cost.

A novel contribution from this work is the GHX model that is formulated as a system of three ODEs and supports any two-fluid HXs with a co-current or counter-current flow orientation. The solution procedure solves the ODEs numerically instead of applying an analytical solution that relies on constant fluid properties.

This work also introduced two methods for the design and performance prediction of an RIT whose capabilities were demonstrated for the RIT of a propane Rankine cycle. More specifically, the robustness of the RIT design optimization method was illustrated by verifying that the optimized RIT geometry was independent of the starting point used for optimization. In addition, the RIT performance analysis method predicted physically consistent RIT performance maps covering both sub-sonic and super-sonic flow velocities. Super-sonic flow velocities might indeed occur in Rankine cycle turbines and this work introduced an efficient and elegant treatment for such cases.

Finally, two methods were developed to design and predict the performance of Rankine cycles. These methods take the advantage of the GHX-model and the RIT model. A novelty of these methods is that the underlying models are included by means of equality constraints. Moreover, as far as found in the literature, the present Rankine cycle design optimization method is the only method that includes geometry parameters of both HX *and* RIT among the independent variables. In addition, the Rankine cycle performance optimization method supports four different approaches for controlling the cycle.

The capabilities of these methods were demonstrated for the Rankine cycle of a novel heat-to-power system utilizing heat released from the process of batch-wise metal casting. More

specifically, the proposed Rankine cycle optimization methods were used to design and analyze three CO_2 Rankine cycles. This case study demonstrated that the Rankine cycle design optimization problem contains few local optima and that the design optimization method converges to the global optimum with a high probability. The case study also demonstrated that the additional flexibility given by the novel control approaches yield improved thermodynamic performance over the "standard" sliding pressure control approach. The outcome of the Rankine cycle performance optimizations showed that the VIGV control approach enabled operation with a larger pressure ratio across the RIT by reducing the nozzle throat opening. Moreover, the VRS control approach improved the RIT efficiency at off-design conditions by adjusting the rotational speed such that the velocity ratio remains close to its value at the design point. Finally, the "VRS and VIGV" control approach utilized the advantages of both the VRS and the VIGV control approaches and thus had a superior thermodynamic performance.

The case study also gave estimates for the electricity production that can be obtained from the batch-wise casting process at a representative ferroalloy plant. The sliding pressure control approach yielded an annual electricity production of up to 11.6 GWh. Moreover, the case study also gave estimates for the increased annual electricity production that can be realized by adopting novel control approaches. For instance, the VRS and VIGV control approaches increased the estimates for the annual electricity production by up to 9.2% and 10.5%, respectively, compared to sliding pressure. Finally, the choice of design operating point also affected the annual electricity production as the annual electricity production obtained for the three Rankine cycles differed by up to 10% when using the sliding pressure control approach. Among these, the Rankine cycle that was designed for an average operating condition yielded the largest RIT off-design efficiency and annual electricity production.

Considering the flexibility, robustness, and computational cost of the methods proposed in the Ph.D. work, they can be regarded as powerful tools for generating the preliminary design of Rankine cycles and RITs and analyzing their performance at off-design operating conditions.

6.2 Suggestions for further research

The methods and results presented in this thesis leave several paths for future research.

The heat-to-power systems for the batch-wise casting process that was designed and analyzed in the Ph.D. case study can be further analyzed. For example, economic analysis can be performed to quantify the cost-efficiency (eg. payback time and net present value) of the proposed heat-to-power systems. The outcome of such an analysis could also confirm whether the improved thermodynamic performance obtained by the novel control approaches outweigh their additional cost or not and possibly quantify the cost-efficiency improvement. The heat source temperatures used for the Ph.D. case study were generated by a dynamic model that assumed a certain size of the thermal energy storage and a constant value for the flow rate of the heat transfer fluid. Hence, more efficient heat-to-power systems for the batch-wise casting process may be obtained by also optimizing the design

and operation of the heat recovery system. Further work on the coupling between the methods developed in this thesis and the dynamic model of the heat recovery system is therefore encouraged.

The methods proposed in this work may also be further developed. For example, the proposed Rankine cycle design optimization method may be extended to also consider economic aspects. In this case, the objective function would account for the cost of the equipment. The main benefit of this is that the constraint used to limit the total HX surface area below a certain value can be omitted. Instead, the total HX surface area would be a result of the optimization. The degradation of the pump efficiency at off-design conditions is relevant for cases where the pump work is a significant fraction of the net power output such as for CO_2 Rankine cycles. Making the proposed Rankine cycle performance optimization method capable of predicting the pump off-design efficiency should therefore be considered as future work.

Finally, the loss model used by the underlying RIT model should be updated in accordance with future experimental activity. Loss mechanisms associated with supersonic flow are poorly understood and further experimental activity on RITs operating with high-pressure ratios is therefore encouraged.

References

[1] "An official website of the Eurpean Union." https://ec.europa.eu/clima/policies/strategies/2030_en (accessed Jul. 16, 2021).

[2] H. Tian and G. Q. Shu, "Organic Rankine Cycle systems for large-scale waste heat recovery to produce electricity," *Org. Rank. Cycle Power Syst. Technol. Appl.*, pp. 613–636, 2017, doi: https://doi.org/10.1016/B978-0-08-100510-1.00017-X.

[3] A. Guercio and R. Bini, "Biomass-fired Organic Rankine Cycle combined heat and power systems," *Org. Rank. Cycle Power Syst. Technol. Appl.*, pp. 527–567, 2017, doi: https://doi.org/10.1016/B978-0-08-100510-1.00015-6.

[4] M. Orosz and R. Dickes, "Solar thermal powered Organic Rankine Cycles," *Org. Rank. Cycle Power Syst. Technol. Appl.*, pp. 569–612, 2017, doi: https://doi.org/10.1016/B978-0-08-100510-1.00016-8.

[5] C. Spadacini, L. G. Xodo, and M. Quaia, "Geothermal energy exploitation with Organic Rankine Cycle technologies," *Org. Rank. Cycle Power Syst. Technol. Appl.*, pp. 473–525, 2017, doi: https://doi.org/10.1016/B978-0-08-100510-1.00014-4.

[6] B. F. Tchanche, M. Pétrissans, and G. Papadakis, "Heat resources and organic Rankine cycle machines," *Renew. Sustain. Energy Rev.*, vol. 39, pp. 1185–1199, 2014, doi: https://doi.org/10.1016/j.rser.2014.07.139.

[7] S. C. Gülen, "Steam Turbine—Quo Vadis?," *Front. Energy Res.*, vol. 8, pp. 1–20, 2021, doi: https://doi.org/10.3389/fenrg.2020.612731.

[8] P. Colonna *et al.*, "Organic Rankine Cycle Power Systems: From the Concept to Current Technology, Applications, and an Outlook to the Future," *J. Eng. Gas Turbines Power*, vol. 137, no. 10, 2015, doi: https://doi.org/10.1115/1.4029884.

[9] E. Macchi, "Theoretical basis of the Organic Rankine Cycle," *Org. Rank. Cycle Power Syst.*, pp. 3–24, 2017, doi: https://doi.org/10.1016/B978-0-08-100510-1.00001-6.

[10] K. Brun, P. Friedman, and R. Dennis, *Fundamentals and Applications of Supercritical Carbon Dioxide (sCO_2) Based Power Cycles,*. Woodhead Publishing, 2017.

[11] M. Astolfi, E. Martelli, and L. Pierobon, "Thermodynamic and technoeconomic optimization of Organic Rankine Cycle systems," *Org. Rank. Cycle Power Syst.*, pp. 173–249, 2017, doi: https://doi.org/10.1016/B978-0-08-100510-1.00007-7.

[12] J. Song, C. Gu, and X. Ren, "Influence of the radial-inflow turbine efficiency prediction on the design and analysis of the Organic Rankine Cycle (ORC) system," *Energy Convers. Manag.*, vol. 123, pp. 308–316, 2016, doi: https://doi.org/10.1016/J.ENCONMAN.2016.06.037.

[13] Y. Li, W. Li, X. Gao, and X. Ling, "Thermodynamic analysis and optimization of organic Rankine cycles based on radial-inflow turbine design," *Appl. Therm. Eng.*, vol. 184, no. 116277, 2021, doi:

https://doi.org/10.1016/j.applthermaleng.2020.116277.

[14] Y. Du, K. Chen, and Y. Dai, “A study of the optimal control approach for a Kalina cycle system using a radial-inflow turbine with variable nozzles at off-design conditions,” *Appl. Therm. Eng.*, vol. 149, pp. 1008–1022, 2019, doi: https://doi.org/10.1016/J.APPLTHERMALENG.2018.12.117.

[15] S. Quoilin, M. Van Den Broek, S. Declaye, P. Dewallef, and V. Lemort, “Techno-economic survey of organic rankine cycle (ORC) systems,” *Renew. Sustain. Energy Rev.*, vol. 22, pp. 168–186, 2013, doi: https://doi.org/10.1016/j.rser.2013.01.028.

[16] M. Chys, M. van den Broek, B. Vanslambrouck, and M. De Paepe, “Potential of zeotropic mixtures as working fluids in organic Rankine cycles,” *Energy*, vol. 44, no. 1, pp. 623–632, 2012, doi: https://doi.org/10.1016/J.ENERGY.2012.05.030.

[17] G. Bamorovat Abadi and K. C. Kim, “Investigation of organic Rankine cycles with zeotropic mixtures as a working fluid: Advantages and issues,” *Renew. Sustain. Energy Rev.*, vol. 73, pp. 1000–1013, 2017, doi: https://doi.org/10.1016/j.rser.2017.02.020.

[18] M. Astolfi, “Technical options for Organic Rankine Cycle systems,” *Org. Rank. Cycle Power Syst.*, pp. 67–89, 2017, doi: https://doi.org/10.1016/B978-0-08-100510-1.00003-X.

[19] F. Capra and E. Martelli, “Numerical optimization of combined heat and power Organic Rankine Cycles – Part B: Simultaneous design & part-load optimization,” *Energy*, vol. 90, pp. 329–343, 2015, doi: https://doi.org/10.1016/J.ENERGY.2015.06.113.

[20] E. Martelli, F. Capra, and S. Consonni, “Numerical optimization of Combined Heat and Power Organic Rankine Cycles – Part A: Design optimization,” *Energy*, vol. 90, pp. 310–328, 2015, doi: https://doi.org/10.1016/J.ENERGY.2015.06.111.

[21] S. Quoilin, R. Aumann, A. Grill, A. Schuster, V. Lemort, and H. Spliethoff, “Dynamic modeling and optimal control strategy of waste heat recovery Organic Rankine Cycles,” *Appl. Energy*, vol. 88, no. 6, pp. 2183–2190, 2011, doi: https://doi.org/10.1016/j.apenergy.2011.01.015.

[22] S. Schuster, C. N. Markides, and A. J. White, “Design and off-design optimisation of an organic Rankine cycle (ORC) system with an integrated radial turbine model,” *Appl. Therm. Eng.*, vol. 174, no. 115192, 2020, doi: https://doi.org/10.1016/J.APPLTHERMALENG.2020.115192.

[23] S. Dong, X. Hu, J. F. Huang, T. Zhu, Y. Zhang, and X. Li, “Investigation on improvement potential of ORC system off-design performance by expander speed regulation based on theoretical and experimental exergy-energy analyses,” *Energy*, vol. 220, no. 119753, 2021, doi: https://doi.org/10.1016/j.energy.2021.119753.

[24] D. Walraven, B. Laenen, and W. D’haeseleer, “Comparison of shell-and-tube with plate heat exchangers for the use in low-temperature organic Rankine cycles,” *Energy Convers. Manag.*, vol. 87, pp. 227–237, 2014, doi: https://doi.org/10.1016/J.ENCONMAN.2014.07.019.

[25] S. Bahamonde, M. Pini, C. De Servi, A. Rubino, and P. Colonna, “Method for the Preliminary Fluid Dynamic Design of High-Temperature Mini-Organic Rankine Cycle Turbines,” *J. Eng. Gas Turbines Power*, vol. 139, no. 8, pp. 1–14, 2017, doi: https://doi.org/10.1115/1.4035841.

[26] P. Valdimarsson, “Radial inflow turbines for Organic Rankine Cycle systems,” *Org. Rank. Cycle Power Syst. Technol. Appl.*, pp. 321–334, 2017, doi: https://doi.org/10.1016/B978-0-08-100510-1.00010-7.

[27] H. Moustapha, M. F. Zelesky, N. C. Baines, and D. Japikse, *Axial and Radial Turbines*. Vermont, USA: Concepts NREC, 2003.

[28] I. H. Bell and E. W. Lemmon, “Organic fluids for Organic Rankine Cycle systems: Classification and calculation of thermodynamic and transport properties,” *Org. Rank. Cycle Power Syst.*, pp. 91–119, 2017, doi: https://doi.org/10.1016/B978-0-08-100510-1.00004-1.

[29] E. W. Lemmon, I. H. Bell, M. L. Huber, and M. O. McLinden, “NIST Standard Reference Database 23: Reference Fluid Thermodynamic and Transport Properties-REFPROP, Version 10.0, National Institute of Standards and Technology,” 2018, doi: https://doi.org/10.18434/T4JS3C.

[30] K. Schittkowski, “NLPQL: a FORTRAN subroutine solving constrained nonlinear programming problems,” *Ann. Oper. Res.*, vol. 5, pp. 485–500, 1986, doi: https://doi.org/10.1007/BF02022087.

[31] J. Nocedal and S. J. Wright, *Numerical optimization*, 2nd ed., 2006, doi: https://doi.org/10.1007/978-0-387-40065-5.

[32] M. Nikolaisen and T. Andresen, “System impact of heat exchanger pressure loss in ORCs for smelter off-gas waste heat recovery,” *Energy*, vol. 215, no. 118956, 2021, doi: https://doi.org/10.1016/j.energy.2020.118956.

[33] F. P. Incropera, D. P. Dewitt, T. L. Bergman, and A. S. Lavine, *Fundamentals of Heat and Mass Transfer*, Sixth edit. John Wiley & Sons, 2006.

[34] A. Cavallini, “Heat transfer and heat exchangers,” *Org. Rank. Cycle Power Syst. Technol. Appl.*, pp. 397–470, 2017, doi: https://doi.org/10.1016/B978-0-08-100510-1.00013-2.

[35] L. Yao and Z. Zou, “A one-dimensional design methodology for supercritical carbon dioxide Brayton cycles: Integration of cycle conceptual design and components preliminary design,” *Appl. Energy*, vol. 276, no. 115354, 2020, doi: https://doi.org/10.1016/j.apenergy.2020.115354.

[36] D. Walraven, B. Laenen, and W. D’haeseleer, “Optimum configuration of shell-and-tube heat exchangers for the use in low-temperature organic Rankine cycles,” *Energy Convers. Manag.*, vol. 83, pp. 177–187, Jul. 2014, doi: https://doi.org/10.1016/J.ENCONMAN.2014.03.066.

[37] E. Kreyszig, *Advanced Engineering Mathematics*, 9th ed. John Wiley & Sons, 2006.

[38] Y. Jaluria, *Design and Optimization of Thermal Systems*, 2nd ed. Taylor & Francis Group, 2008.

[39] G. Persico and M. Pini, “Fluid dynamic design of Organic Rankine Cycle turbines,” *Org. Rank. Cycle Power Syst.*, pp. 253–297, 2017, doi: https://doi.org/10.1016/B978-0-08-100510-1.00008-9.

[40] R. Agromayor, “Advancements in Automated Methods for Fluid-Dynamic Turbomachinery Design,” PhD thesis, NTNU, 2021.

[41] R. Agromayor and L. O. Nord, “Preliminary Design and Optimization of Axial Turbines Accounting for Diffuser Performance,” *Int. J. Turbomachinery, Propuls.*

Power, vol. 4, no. 3, 2019, doi: https://doi.org/10.3390/ijtpp4030032.

[42] S. L. Dixon and C. A. Hall, *Fluid Mechanics and Thermodynamics of Turbomachinery*, *Fluid Mech. Thermodyn. Turbomach.*, 7th ed., 2014, doi: https://doi.org/10.1016/C2009-0-20205-4.

[43] A. Meroni, M. Robertson, R. Martinez-Botas, and F. Haglind, "A methodology for the preliminary design and performance prediction of high-pressure ratio radial-inflow turbines," *Energy*, vol. 164, pp. 1062–1078, 2018, doi: https://doi.org/10.1016/J.ENERGY.2018.09.045.

[44] R. Agromayor and L. O. Nord, "Fluid selection and thermodynamic optimization of organic Rankine cycles for waste heat recovery applications," *IV Semin. ORC Power Syst.*, vol. 129, pp. 527–534, 2017, doi: https://doi.org/10.1016/J.EGYPRO.2017.09.180.

[45] H. I. H. Saravanamutto, G. F. C. Rogers, H. Cohen, and P. V. Straznicky, *Gas turbine theory*, 6th ed. Pearson Education, 2009.

[46] L. Zhai *et al.*, "An improved modeling for low-grade organic Rankine cycle coupled with optimization design of radial-inflow turbine," *Energy Convers. Manag.*, vol. 153, pp. 60–70, 2017, doi: http://dx.doi.org/10.1016/j.enconman.2017.09.063.

[47] M. T. Børset, "Energy dissipation and recovery in the context of silicon production," PhD thesis, NTNU, 2015.

[48] C. M. Invernizzi and D. Bonalumi, "Thermal stability of organic fluids for Organic Rankine Cycle systems," *Org. Rank. Cycle Power Syst. Technol. Appl.*, pp. 121–151, 2017, doi: https://doi.org/10.1016/B978-0-08-100510-1.00005-3.

[49] M. T. White, G. Bianchi, L. Chai, S. A. Tassou, and A. I. Sayma, "Review of supercritical CO2 technologies and systems for power generation," *Appl. Therm. Eng.*, vol. 185, 2021, doi: https://doi.org/10.1016/j.applthermaleng.2020.116447.

[50] G. Musgrove, S. Sullivan, D. Shiferaw, P. Fourspring, and L. Chordia, "Heat exchangers," *Fundam. Appl. Supercrit. Carbon Dioxide Based Power Cycles*, pp. 217–244, 2017, doi: https://doi.org/10.1016/B978-0-08-100804-1.00008-6.

[51] A. Uusitalo, A. Ameli, and T. Turunen-Saaresti, "Thermodynamic and turbomachinery design analysis of supercritical Brayton cycles for exhaust gas heat recovery," *Energy*, vol. 167, pp. 60–79, 2019, doi: https://doi.org/10.1016/j.energy.2018.10.181.

[52] S. W. Spence and D. W. Artt, "Experimental performance evaluation of a 99.0 mm radial in flow nozzled turbine with different stator throat areas," in *Proceedings of the Institution of Mechanical Engineers, Part A: Journal of Power and Energy*, 1997, vol. 211, pp. 477–488.

Appendix A Main publications

A.1 Paper I

A novel methodology for Rankine cycle analysis with generic heat exchanger models

Brede A. L. Hagen, Monika Nikolaisen, Trond Andresen, *Applied Thermal Engineering*, vol. 165, no. 114566, 2020.

DOI: https://doi.org/10.1016/j.applthermaleng.2019.114566

Applied Thermal Engineering 165 (2020) 114566

Contents lists available at ScienceDirect

Applied Thermal Engineering

journal homepage: www.elsevier.com/locate/apthermeng

A novel methodology for Rankine cycle analysis with generic heat exchanger models

Brede A.L. Hagen[a,*], Monika Nikolaisen[b], Trond Andresen[b]

[a] Department of Energy- and Process Engineering, NTNU – Norwegian University of Science and Technology, Kolbjørn Hejes vei 1B, NO-7491 Trondheim, Norway
[b] SINTEF Energy Research, Sem Sælands vei 11, 7034 Trondheim, Norway

HIGHLIGHTS

- A new methodology based on a generic heat exchanger model is proposed.
- This methodology is a more informative alternative to pure thermodynamic analyses.
- Optimize the trade-off between heat transfer coefficient and pressure drop.
- Optimal heat exchanger design depends on its allowed size and the working fluid.
- The new methodology can be applied to both design and off-design analysis.

ARTICLE INFO

Keywords:
Rankine cycle
ORC
Generic heat exchanger
Modelling
Optimisation

ABSTRACT

This study presents a novel approach for Rankine cycle (RC) analysis, introducing a generic counter current heat exchanger (HX) model to enable basic fluid thermal and flow behaviour in HXs to be considered in a cycle optimisation process. The generic HX model does not represent a certain HX-type or even a manufacturable design, but applies fluid properties and a minimum amount of generic geometry parameters to estimate local heat transfer coefficients and pressure gradients. The proposed methodology thus permits simultaneous optimization of process state points and the trade-off between overall heat transfer coefficient and pressure drop without relying on a specific HX-geometry concept. The proposed methodology is demonstrated for evaluation of single-stage recuperated RC's of different HX size and working fluids, and compared with more conventional thermodynamic analyses. The comparison showed that the novel analysis resulted in lower net power output than the thermodynamic analyses due to working fluid-depending pressure drop in heat exchangers, and a quantitative HX size estimate in terms of total HX area based on working-fluid depended heat transfer coefficients. We therefore suggest the novel analysis as a low effort and more informative alternative to pure thermodynamic approaches for initial RC analyses.

1. Introduction

The Rankine cycle (RC), conventionally referred to as ORC when it employs an organic working fluid, is a mature technology. It can be applied to for instance power production from industrial waste heat and from renewable energy sources such as geothermal energy, biomass and solar energy [1]. However, the full potential of RCs is far from reached as the power production potential from the above-mentioned energy sources alone could meet the worlds power demand [2]. One step towards increasing the utilization of RCs, and thus facilitate reduction of greenhouse gas emissions from fossil fuel power plants, is to optimise the RC for each application. This is a challenging task and research efforts on RCs typically focus on certain aspects such as application, expander technology, dynamics, working fluid, cycle architecture or optimization [3]. This paper focuses on the underlying methodology of the three last aspects, hereafter referred to as RC analysis.

Rankine cycle analysis can be classified into two approaches (thermodynamic and thermo-economic) [4], defined and exemplified in the following sections. A thermodynamic analysis consists of determining optimal operating conditions for a set of working fluid candidates or cycle layouts subjected to thermodynamic objective function(s) and constraints. A common assumption in these analyses is fixed pinch point temperature differences (PPTDs) in the heat exchangers (HXs), hereafter referred to as “PPTD analysis” [5–7].

* Corresponding author.
E-mail address: brede.hagen@ntnu.no (B.A.L. Hagen).

https://doi.org/10.1016/j.applthermaleng.2019.114566
Received 14 March 2019; Received in revised form 2 October 2019; Accepted 19 October 2019
Available online 21 October 2019

Nomenclature

A	HX surface area, m^2
A_{cross}	Flow cross-sectional area m^2
D	Hydraulic diameter, m
f	Friction factor
h	Specific enthalpy, J/kg
i	Integration step index
k	Thermal conductivity, W/mK
L	HX flow length, m
$\dot{m}$	Mass flow, kg/s
M	Molar mass, g/mol
n	Number of integration steps
p	Pressure, kPa
Δp	Pressure loss, Pa
P	Channel perimeter, m
Q	Heat transfer rate, W
R	Thermal resistance, mK/W
T	Temperature, K
$\Delta\bar{T}$	Mean temperature difference, K
U	Overall heat transfer coefficient, W/m^2K
UA	Product of overall HTC and HX area, W/K
v	Fluid velocity, m/s
W	Electric power, W
x	Position in HX flow direction, m, vapor quality

Greek symbols

α	Local heat transfer coefficient, W/m^2K
ρ	Fluid mass density, kg/m^3
η	Efficiency

Subscripts

1–11	State points in the cycle (Fig. 3)
c	Cold side
cond	Condenser
evap	Evaporator
exp	Expander
gen	Generator
h	Hot side
is	Isentropic
m	Motor
pump	Pump
recup	Recuperator
s	Heat sink
spec	Specification
tot	Total
w	HX channel wall
wf	Working fluid

Acronyms

GHX	Generic heat exchanger
HTC	Heat transfer coefficient
HX	Heat exchanger
LMTD	Log mean temperature difference
NPV	Net present value
ORC	Organic Rankine cycle
PPTD	Pinch point temperature difference
RC	Rankine cycle

PPTD analysis is often used for comparison of different RCs that operate under the same boundary conditions. For instance, previous PPTD analyses have demonstrated that the transcritical cycle has a better thermodynamic performance potential than the subcritical cycle [8–10]. Chys et al. [7] used a PPTD analysis to demonstrate up to 16% increase in thermodynamic performance by using zeotropic mixtures instead of pure working fluids. Wu et al. [11] confirmed the superior thermodynamic performance potential of zeotropic mixtures, but demonstrated that the ratio between net power output and the total HX UA-value decreased, indicating that improved performance with zeotropic mixtures comes at the cost of larger heat exchangers. PPTD analysis has also been applied to compare the subcritical cycle with the trilateral flash cycle [12] and for working fluid screening of RCs utilizing LNG cold energy [13]. Vivian et al. [14] performed a PPTD analysis of multiple working fluids for both recuperated and non-recuperated cycles. They demonstrated that for a heat source inlet temperature of 180 °C, adding a recuperator can give up to 9% increase in thermodynamic performance when the there is a lower limit on the heat source outlet temperature.

The main advantage of PPTD analysis is that it is fast and only requires PPTDs for defining the HXs. However, ranking a set of working fluids, cycle layouts or optimum operating conditions (i.e. subcritical vs. transcritical) from best to worst with a PPTD analysis alone is challenging, since heat exchangers of equal PPTDs does not necessarily correspond to equal HX sizes, costs, or fluid pressure drop. In addition, as several authors have pointed out, there is a trade-off between HX size and net power output when selecting PPTDs in the HXs [15–17], and the optimal values of PPTDs in each heat exchanger are not obvious [18].

Thermodynamic analysis can partly overcome the above-mentioned issues by optimizing the PPTD's in the heat exchangers with a constraint on the total HX UA-value, hereafter denoted UA-analysis. To the best of our knowledge, UA-analysis is rarely performed; the most relevant publication found was Ref. [19] where different CO_2 Brayton cycles with identical total UA-values were compared. A similar methodology was employed in Ref. [20], where total HX area (based on predefined values for overall HTC) was used as a basis for comparison between working fluids for both subcritical RC and the trilateral flash cycle. However, it has been stressed that UA-value is only a preliminary indicator of HX size due to its approximation of equal heat transfer coefficients [21].

Thermo-economic analyses include cost estimates, in addition to the thermodynamic performance, in the objective function or constraints. Thermo-economic analyses can therefore search for the optimal compromise between system cost and thermodynamic performance. One example is the study by Walraven et al. [22], who analysed RCs of different configurations and working fluids for geothermal heat sources. The authors used an air-cooled condenser model and a shell and tube model for the remaining heat exchangers. They simultaneously optimised process conditions and HX geometry parameters to maximize the net present value (NPV) of the installation, assuming a lifetime of 30 years. They found that the heat source inlet and outlet temperatures, as well as economic parameters such as electricity price and discount rate, had a strong influence on the NPV. The work illustrates that thermo-economic analysis gives detailed results but requires a larger amount of uncertain, application dependent input parameters compared to the thermodynamic analyses.

Other examples of thermo-economic studies are found in Refs. [23–25]. All these studies consider at least three working-fluid candidates, involve detailed heat exchanger models and both thermodynamic and economic performance are included in the objective function. The results from Refs. [24,25] did not show any economic advantage of using zeotropic mixtures instead of pure working fluids even though thermodynamic analyses has proven superior thermodynamic

performance potential of zeotropic mixtures [7]. A comparison between thermodynamic- and thermo-economic analysis was performed by Quoilin et al. [26] for working fluid selection of a small-scale RC for waste heat application. Their results demonstrated that the two methodologies gave different results in the ranking of the working fluid candidates from best to worst, as well as different evaporation temperature. The paper concludes that thermodynamic analysis may not identify the best working fluid in terms of economic profitability.

Thermo-economic analyses have also been applied for RC-optimization considering off-design performance [27,28]. Results in Ref. [28] demonstrated that the most economic design compensated slightly undersized heat exchangers and turbines, with good performance at off-design conditions. Although this approach is very promising for a realistic design optimisation, additional requirements for such analyses are the knowledge of the variations in the boundary conditions with time, and part-load models for the components.

Thermo-economic analyses provide quantitative results but are very specific and thus challenging to apply for an application where for instance the optimal set of component types are unknown. Furthermore, thermo-economic analyses are also computationally demanding for cases with multiple working fluid or cycle layout candidates. In such cases, the number of candidates can be reduced by using an initial screening analysis. Thermodynamic analysis is the traditional method for screening multiple working fluid candidates. However, the above-mentioned studies indicate that thermodynamic analysis might give misleading results, partly because the heat transfer coefficient depends on the working fluid, which is particularly true for two-phase flow of pure fluids vs. zeotropic mixtures, or for boiling vs. supercritical heating.

Using thermal-hydraulic heat exchanger models in the system optimization (without considering cost) is one way of obtaining realistic estimates of HX design and size. One example is the study by Dong et al. [29], who performed a PPTD analysis of pure and zeotropic working fluids mixtures followed by a heat exchanger area calculation based on concentric double pipe HXs with fixed diameters. The analysis showed that zeotropic mixtures increased net power production under the fixed PPTD assumption, but the ratio between net power production and total HX area was reduced. Walraven et al. [30] optimized Rankine Cycles of different pure working fluids and layouts considering both shell-and-tube and plate HX. They demonstrated that systems with plate HXs perform better that systems with shell and tube HXs. They also pointed out that a possible disadvantage of plate HX with equal number of fluid passes is that the fluid channels are of equal cross-sectional area, which might lead to an inefficient heat exchanger if the volume flow rate of the two fluids differ significantly. These studies solve the problem of determining realistic estimates of HX size, but still they rely on a predefined HX geometry concept.

With basis in existing literature on we believe there is a need for a new, low computationally demanding approach to RC analysis that gives more informative results than the thermodynamic analyses, without the need for pre-selecting component types. The novel methodology for RC analysis presented in this paper is a step towards such an approach and involves the use of a generic thermal-hydraulic HX model, hereafter referred to as the GHX-model. The idea of a generic HX model is not completely new. Some of the HX's in Refs. [31,32] were modelled by stacked layers of multiport tubes to represent a generic compact heat exchanger. However, this work takes this approach a step further since the GHX-model does not represent any manufacturable HX design. Instead, the HX geometry is defined by the generic geometry parameters required for applying thermal-hydraulic correlations for channel flow. This novel approach permits simultaneous optimization of process state points and the trade-off between overall heat transfer coefficient and pressure drop in the HX's. As such, this approach includes the effect of pressure drop on the net power output and provides a quantitative basis for HX size comparison in terms of total HX area. The proposed methodology thus permits comparison of different RCs of equal total HX area, without having to decide which specific HX types to use.

The paper is organised as follows: the proposed RC model and optimisation formulation is presented in detail in Section 2. Section 3 demonstrates the novel methodology by analysing Rankine cycles with different working fluids and HX sizes for a given heat source. The simulation results from the novel methodology are compared with results from the two thermodynamic analyses described. The most important results are discussed in Section 4, and conclusions drawn from this study are given in Section 5.

2. Methodology

2.1. The novel Rankine cycle analysis

The novel Rankine cycle analysis, hereafter denoted “GHX-analysis”, involves the use of a generic heat exchanger model (GHX-model), the development of a RC model that applies the GHX-model, and an optimisation formulation. These three elements are described in detail in the following three subsections.

2.1.1. The GHX-model

The GHX-model involves a somewhat abstract representation of heat transfer mechanisms, and does not require specification of heat exchanger type, i.e. shell and tube, plate or finned tube, etc. Only five generic HX parameters are required to specify the HX geometry; hydraulic diameter (both fluids), flow cross-sectional area (both fluids) and length (the same for both fluids).

These geometry parameters provide the information required to apply thermal-hydraulic correlations for heat transfer and pressure drop. Fig. 1 shows an example cross-section of the GHX-model under the assumption that the fluids flow in multiple circular channels. In this example the hydraulic diameter is the channel diameter and the cross-sectional flow area on the hot and cold side is represented by the red and blue areas, respectively.

The remainder of this section contains a detailed mathematical description of the GHX-model, which consists of three differential equations that have to be solved. The first differential equation (Eq. (1)) describes the heat transfer rate per unit length between the hot and cold fluids.

$$\frac{dQ}{dx} = \frac{T_h - T_c}{R} \tag{1}$$

The total thermal resistance between the hot and cold fluids, *R*,

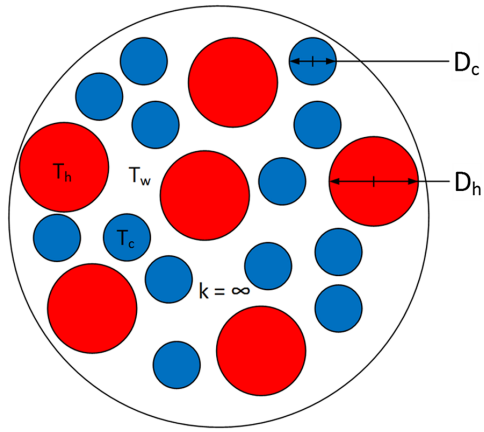

Fig. 1. Example cross-section of the generic HX model under the assumptions that the fluids flow in multiple circular channels.

Table 1
Heat transfer and pressure drop correlations employed in the GHX-model.

Flow	Heat transfer	Pressure drop
Single-phase	Gnielinski [33]	Selander [34]
Two-phase	Boyko and Kruhzilin [35] (condensation) Bennet & Chen [36] (evaporation) Silver [37] and Bell and Ghaly [38] for the mixture effects in multicomponent condensation and evaporation	Friedel [39] with single-phase formulation by Selander [34]

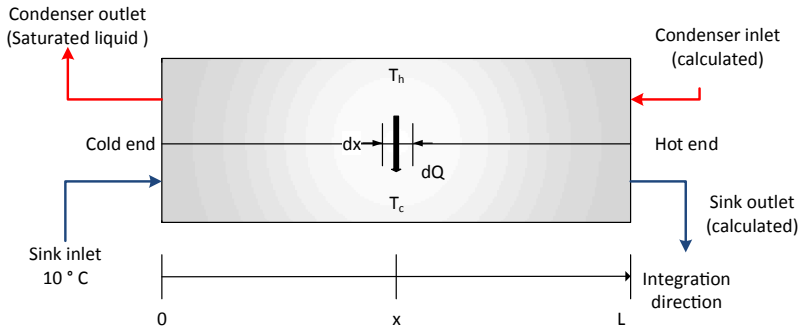

Fig. 2. Calculation of the condenser using the GHX-model.

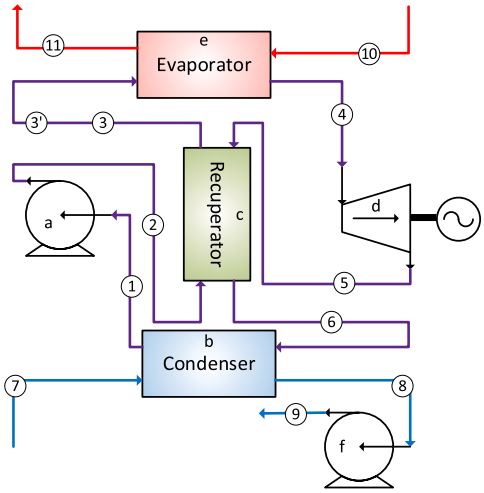

Fig. 3. The single-stage recuperated RC. Letters a-f indicate the component calculation sequence for the novel RC model using generic HX models. Numbers 1–11 indicate the state points (pressure and enthalpy) in the RC model.

includes thermal resistance from convection according to Eq. (2).

$$R = \frac{1}{\alpha_c P_c} + \frac{1}{\alpha_h P_h},\ P = \frac{4A_{cross}}{D} \tag{2}$$

The two remaining differential equations calculate the change in pressure per unit length of the hot and the cold fluids in the HX:

$$\frac{dp_j}{dx} = \pm f_j \frac{\rho_j v_j^2}{2D_j},\ j = c,\ h \tag{3}$$

The ± symbol in Eq. (3) indicates that pressure can either increase or decrease when integrating through the HX since the fluids flow in opposite directions.

Heat transfer coefficients and friction factors can either be set to constant values or calculated by thermal hydraulic correlations taking into account transport-properties such thermal conductivity and viscosity. There are multiple thermal-hydraulic correlations available for channel flow and the discussion of the optimal set of correlations are

Table 2
Optimization formulation for the three different analyses considered in this paper. In each column below the headings indicating the analysis type, "X" means that the variable or constraint is applied, while "-" means that it is not applied.

		Analysis method		
	Variable/Function	GHX	UA	PPTD
Process variables	p_1	X	X	X
	p_2	X	-	-
	p_4	X	X	X
	h_4	-	X	X
	$\dot{m}_{wf}$	X	X	X
	$\dot{m}_s$	X	X	X
	Q_{recup}	–	X	X
Evaporator geometry variables	L	X	–	–
	$A_{cross,wf}$	X	–	–
Condenser geometry variables	L	X	–	–
	$A_{cross,wf}$	X	–	–
Recuperator geometry variables	L	X	–	–
	$A_{cross,h}$	X	–	–
	$A_{cross,c}$	X	–	–
Equality constraints	$p_3 - p_3^{'} = 0$	X	–	–
	$h_3 - h_3^{'} = 0$	X	–	–
Inequality constraints	$T_{11} - T_{11,spec} \geq 0$	X	X	X
	$x_4 - 1 \geq 0$	X	X	X
	$x_5 - 1 \geq 0$	X	X	X
	$A_{tot,spec} - A_{tot} \geq 0$	X	–	–
	$UA_{tot,spec} - UA_{tot} \geq 0$	–	X	–
	$PPTD_{spec} - PPTD_{recup} \geq 0$	–	–	X
	$PPTD_{spec} - PPTD_{cond} \geq 0$	–	–	X
	$PPTD_{spec} - PPTD_{evap} \geq 0$	–	–	X
Objective function	W_{net}	X	X	X

Table 3
Heat source and heat sink parameters in simulation case.

	Case parameters	Unit	
Heat source	Fluid	–	Water
	Inlet temperature	[°C]	140
	Lower temperature limit (inequality constraint)	[°C]	70
	Mass flow	[kg/s]	2.9
	Pressure	[bar]	10
Heat sink	Fluid	–	Water
	Inlet temperature	[°C]	10

Table 4
Fixed parameters for the demonstration cases. Parameters for expander and pump are employed in both the thermodynamic and the novel GHX-analysis, while the HX parameters are only relevant for the GHX-analysis.

Component	Parameter	Unit	Value
Pumps	Isentropic efficiency	–	0.70
	Motor efficiency	–	0.95
Expander	Isentropic efficiency	–	0.85
	Generator efficiency	–	0.95
Evaporator	Hydraulic diameter, working-fluid side	[cm]	1.0
	HTC heat-source side	[kW/m^{2}K]	5.0
	Heat-source pressure drop	[kPa]	0.0
	Area ratio (hot/side)	–	1.0
Condenser	Hydraulic diameter, working-fluid side	[cm]	2.0
	Hydraulic diameter, sink side	[cm]	2.0
	Sink side cross-sectional area	[cm^2]	100
Recuperator	Hydraulic diameter, low-pressure side	[cm]	2.0
	Hydraulic diameter, high-pressure side	[cm]	1.0

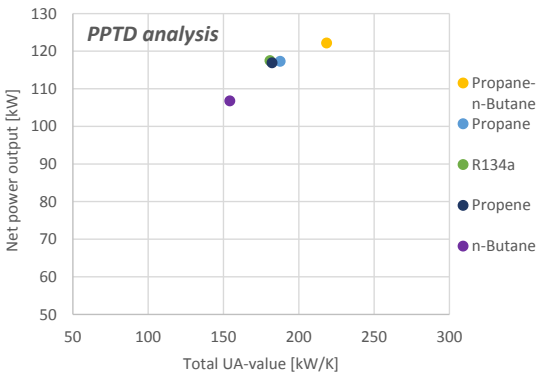

Fig. 4. Results of the PPTD analysis, showing maximized net power versus total UA-value for the different working fluids.

out of the scope of this article. The correlations applied in this work are widely used and based on experiments of flow in circular channels and cover both single-phase and two-phase flow of mixtures and pure fluids, Table 1. We believe that the chosen correlations are adequate for generic heat exchanger analysis, because they are mainly functions of physical properties and the Reynolds number and involves a minimum of regression coefficients. Therefore, these correlations are relatively safe with respect to extrapolation to fluids not being subjected to experimental activity during the correlation development.

The GHX-model requires the fluid states at either the hot or the cold end to be specified. These states are the *boundary conditions* for Eq. (1) and Eq. (3).

A calculation example for the condenser is presented, and calculations of the other HXs are similar. In the condenser, the states at the

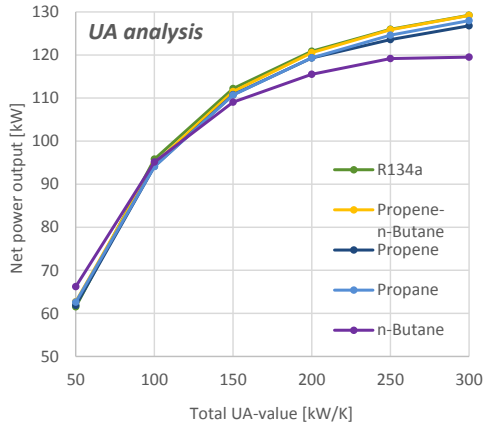

Fig. 5. Results of the UA-analysis, showing maximised net power versus total UA-value for the different working fluids.

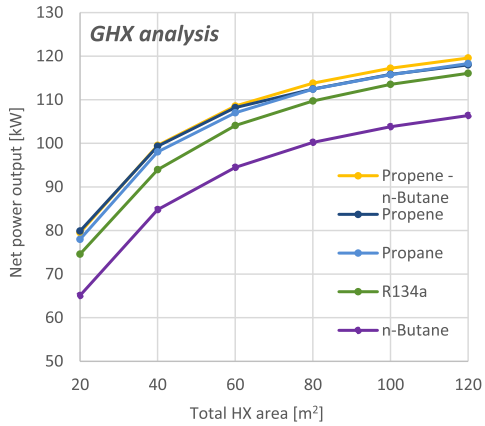

Fig. 6. Results of the GHX-analysis, showing maximized net power versus total HX area for the different working fluids.

cold end are specified, Fig. 2. The condenser is solved by n equidistant numerical integration steps, starting at the cold end. Eq. (1) is solved by a fourth-order Runge-Kutta method and gives the fluid enthalpies for the next step. Eq. (3) is solved by an explicit Euler method and gives the fluid pressures for the next step. Outputs from the GHX-model are the heat duty, HX area, pressure drop of both fluids and an estimate of the overall heat transfer coefficient $U = \frac{Q}{A\Delta\bar{T}}$, where $\Delta\bar{T} = \frac{1}{L}\int_0^L \Delta T dx$ is the mean temperature difference between the hot and cold fluids, and is approximated by the trapezoidal method for numerical integration, Eq. (4).

$$\Delta\bar{T} = \frac{1}{n}\sum_{i=1}^{n}\frac{\Delta T_i + \Delta T_{i-1}}{2} \tag{4}$$

The HX area for the condenser and evaporator, $A_{cond,evap} = P_{wf}\mathrm{L}$, is calculated as the surface area on the working-fluid side, while the recuperator area $A_{recup} = \frac{1}{2}(P_c + P_h)L_{recup}$ is calculated as the average value of the surface area on the high- and low-temperature sides of the recuperator.

2.1.2. The Rankine cycle model

A graphical illustration of the RC model is shown in Fig. 3, which represents the well-known single-stage recuperated RC. The non-

Table 5
Optimisation results from GHX-analysis with maximum total HX area of 60 m^2.

Working fluid		Propene/n-Butane	Propene	Propane	R134a	n-Butane
Net power	[kW]	108.5	108.2	107.0	104.1	94.5
Process parameters						
Pump inlet pressure	[bar]	9.6	10.6	8.6	6.3	2.5
Expander inlet pressure	[bar]	49.1	51.6	46.6	43.6	14.0
Working fluid mass flow	[kg/s]	2.0	2.0	2.0	3.8	1.9
Heat sink mass flow	[kg/s]	24.0	25.8	25.8	25.2	26.8
Evaporator						
Length	[m]	37.5	35.8	38.3	35.9	26.0
$A_{cross,wf}$	[cm^2]	19.1	19.9	18.7	19.5	25.8
Area	[m^2]	28.7	28.4	28.6	27.9	26.8
Heat duty	[kW]	860	862	862	862	862
Overall HTC	[W/m^2K]	2881	2853	2887	2730	2376
Working fluid pressure drop	[kPa]	148	148	153	194	77
PPTD	[K]	4.9	4.6	4.8	4.9	2.6
Condenser						
Length	[m]	29.2	29.3	29.7	23.4	17.5
$A_{cross,wf}$	[cm^2]	43.9	43.0	44.0	59.4	95.2
Area	[m^2]	25.6	25.2	26.1	27.8	33.3
Heat duty	[kW]	740	742	743	748	757
Overall HTC	[W/m^2K]	3047	3206	3052	2390	1638
Working fluid pressure drop	[kPa]	75	79	85	82	31
Heat sink pressure drop	[kPa]	90	103	104	79	66
PPTD	[K]	8.4	7.1	7.3	9.1	11.2
Recuperator						
Length	[m]	6.0	6.9	5.5	3.4	0.0
$A_{cross,h}$	[cm^2]	71.6	69.9	74.5	98.8	–
$A_{cross,c}$	[cm^2]	11.3	11.1	11.0	13.8	–
Area	[m^2]	5.7	6.4	5.3	4.3	–
Heat duty	[kW]	82	87	85	51	–
Overall HTC	[W/m^2K]	1012	1064	1024	745	–
Cold-side pressure drop	[kPa]	31.3	38.6	31.0	19.1	–
Hot-side pressure drop	[kPa]	8.3	9.6	7.6	5.7	–
PPTD	[K]	11.5	10.0	13.0	14.0	–
Optimization constraint						
Total HX area	[m^2]	60.0	60.0	60.0	60.0	60.0

recuperated cycle can also be analysed by the RC model by setting the recuperator length to zero. This means that when the recuperator length is a free optimisation variable, both non-recuperated and recuperated RC configurations are considered.

Numbers 1–11 in Fig. 3 represent the state points in the RC model and are defined by pressure and enthalpy. The thermodynamic properties and the transport properties were calculated using the NIST Standard Reference Database, Refprop version 9.1 [40].

Models for the expander and pumps require the inlet state and outlet pressure to be specified and are modelled with constant isentropic and mechanical efficiencies according to Eqs. (5) and (6).

Pump model:

$$\eta_{is} = \frac{h(p_{out}, s_{in}) - h_{in}}{h_{out} - h_{in}}$$

$$W_{pump} = \frac{1}{\eta_m}\dot{m}(h_{out} - h_{in}) \tag{5}$$

Expander model:

$$\eta_{is} = \frac{h_{in} - h_{out}}{h_{in} - h(p_{out}, s_{in})}$$

$$W_{exp} = \eta_{gen}\dot{m}(h_{in} - h_{out}) \tag{6}$$

The letters a-f in Fig. 3 indicate the component calculation sequence. Saturated liquid at state point 1 enters the pump and state point 2 is calculated with the pump model using the specified pump outlet pressure. The condenser is then solved from the cold to the hot end (as described in Section 2.1.1) and state points 6 and 8 are calculated. The state points at the cold end of the recuperator are thus defined, which is the next component to be solved, and state points 3 and 5 are calculated. The expander model is thereafter solved iteratively to find the expander inlet enthalpy using the specified expander inlet pressure and state point 5. Then the evaporator is solved from the hot to the cold end and state points 3′ and 11 are calculated. Finally, the heat sink pump is calculated with a pressure lift equal to the heat sink pressure drop in the condenser, such that the pressures at state points 7 and 9 are equal.

2.1.3. Rankine cycle optimisation

The purpose of the Rankine cycle optimisation is to find the optimal HX geometry and process design that maximizes the net power output (Eq. (7)), subject to a set of constraints that will guarantee a feasible process design.

$$W_{net} = W_{exp} - W_{pump,wf} - W_{pump,s} \tag{7}$$

The optimisation is performed using a gradient-based constrained optimisation solver, NLPQL[41]. The variables, constraint- and objective function for the optimisations are shown in Table 2. Note that expander inlet pressure is a free optimisation variable, which means that the solver can choose between subcritical and transcritical process designs.

Two equality constraints are imposed to ensure that the pressure and temperature at state points 3 and 3′ are identical. Two inequality constraints requiring dry vapour at expander inlet and outlet are also included. Hence, wet expansion cycles are excluded from this analysis. Without constraints on the HX size, the PPTDs in all heat exchangers will be infinitesimally small and the required HX area will increase towards infinity. A constraint on the maximum total HX area is

Table 6
Optimized process and HX geometry from the GHX-analysis for propene.

Total HX area	[m^2]	20	40	60	80	100	120
Net power	[kW]	79.9	99.5	108.2	112.4	115.8	118.0
Process parameters							
Pump inlet pressure	[bar]	11.6	11.0	10.6	10.8	10.7	10.6
Expander inlet pressure	[bar]	51.5	51.8	51.6	51.8	52.4	51.8
Working fluid mass flow	[kg/s]	2.1	2.0	2.0	2.0	2.0	2.1
Heat sink mass flow	[kg/s]	27.6	26.0	25.8	22.6	22.0	23.4
Evaporator							
Length	[m]	25.1	32.2	35.8	38.9	38.7	41.9
$A_{cross,wf}$	[cm^2]	11.8	16.3	19.9	20.6	27.9	27.0
Area	[m^2]	11.8	21.0	28.4	32.1	43.2	45.2
Heat duty	[kW]	845	860	862	862	862	862
Overall HTC	[W/m^2K]	3414	3060	2853	2824	2491	2496
Working fluid pressure drop	[kPa]	250	181	148	149	89	112
PPTD	[K]	13.8	7.8	4.6	3.3	1.6	1.4
Condenser							
Length	[m]	19.9	25.4	29.3	30.3	32.0	32.4
$A_{cross,wf}$	[cm^2]	20.6	32.5	43.0	65.6	67.8	81.6
Area	[m^2]	8.2	16.5	25.2	39.8	43.4	52.8
Heat duty	[kW]	755	749	742	738	735	732
Overall HTC	[W/m^2K]	6429	4028	3206	2159	2126	1837
Working fluid pressure drop	[kPa]	175	107	79	41	42	30
Heat sink pressure drop	[kPa]	80	91	103	83	84	95
PPTD	[K]	12.7	9.1	7.1	6.0	5.4	5.0
Recuperator							
Length	[m]	0.0	3.6	6.9	7.9	10.2	15.0
$A_{cross,h}$	[cm^2]	–	54.1	69.9	77.5	99.7	103.7
$A_{cross,c}$	[cm^2]	–	9.0	11.1	12.7	15.7	21.5
Area	[m^2]	–	2.6	6.4	8.1	13.4	22.0
Heat duty	[kW]	–	55	87	92	105	118
Overall HTC	[W/m^2K]	–	1334	1064	963	778	615
Cold-side pressure drop	[kPa]	–	29.4	38.6	34.6	30.5	25.0
Hot-side pressure drop	[kPa]	–	7.7	9.6	9.2	7.5	9.7
PPTD	[K]	–	14.0	10.0	8.6	6.7	4.1

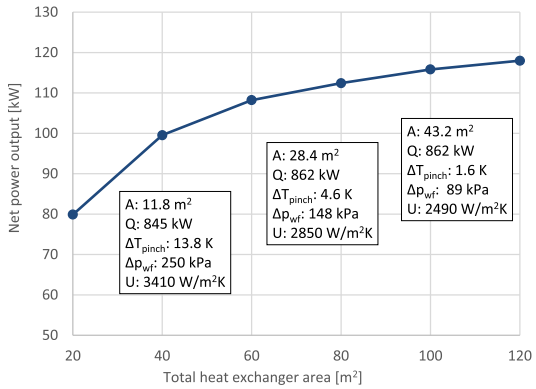

Fig. 7. GHX-analysis: Net power output with propene as working fluid, including selected optimisation results for the evaporator shown in data labels.

therefore imposed. In this case, the optimisation solver will search for the HX geometry that offers the best trade-off between overall HTC and pressure drop and the optimal HX area distribution between the three heat exchangers. In some cases, there are limitations on how far the heat source can be cooled down. We therefore imposed an optional constraint on the minimum heat source outlet temperature. Gradients of the objective function and the constraints were calculated using the second-order central difference approximation for numerical differentiation.

2.2. Thermodynamic analyses

The thermodynamic analyses presented in this work (referred to as PPTD- and UA-analysis) were performed by using a pure thermodynamic Rankine cycle model representing the same cycle layout as in Fig. 3. The thermodynamic model differs from the novel RC model only by using thermodynamic HX models. This HX model neglects working fluid pressure drop and calculates the UA-value and PPTD for given inlet and outlet states by discretising the HX into n sub-HXs of equal heat duty $Q_i = \frac{Q}{n}$. The UA-value was calculated as the sum of the UA-values of all n sub-HXs by the LMTD method given in Eq. (8).

$$UA = \sum_{i=1}^{n} \frac{Q_i}{LMTD_i} \tag{8}$$

The calculated PPTD is the smallest temperature difference between the hot and the cold fluid in all of the sub-HXs. The optimisation procedure for thermodynamic analyses resembles the procedure for the GHX-analysis described in Section 2.1.2, and is shown in detail in Table 2. The main difference is that the HX geometry variables are replaced by variables for expander inlet enthalpy and recuperator duty in order to have the same degrees of freedom on the process-variables as in the GHX-analysis. In addition, since pressure drop is neglected, the working fluid pump outlet pressure and expander inlet pressure refer to the same variable. The last difference in the optimisation procedure is the constraint on HX size. The PPTD analysis has three inequality constraints for minimum PPTDs of 5 K in each heat exchanger, while the UA-analysis has a constraint on the total UA-value in the HXs.

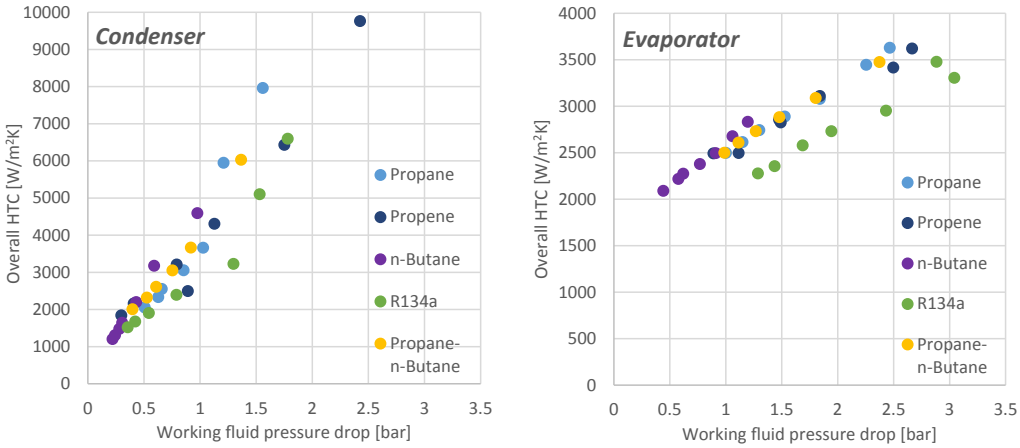

Fig. 8. Overall HTCs and working fluid pressure drops in optimised HXs from the GHX-analysis for different working fluids and total permitted HX area.

3. Demonstration of the novel Rankine cycle analysis

3.1. Description of simulation case

We have defined a simulation case, Table 3, to demonstrate the novel methodology. The case considers pressurised water at 140 °C as the heat source, with a constrained minimum temperature of 70 °C.

3.2. Fixed parameters

The fixed parameters for the optimisations performed in this work are shown in Table 4. Parameters for the expander and pumps are applied for both the thermodynamic and the novel GHX-analysis, while the remaining parameters are only relevant for the GHX-analysis.

To limit the number of free optimisation variables in the GHX-analysis, but at the same time enable optimizing the trade-off between overall HTC and pressure drop, the hydraulic diameters in the heat exchangers are kept constant. Their values might not be the optimal one from a thermal-hydraulic point of view. However, the fixed values at least ensure that the hydraulic diameter are within a reasonable size with respect to for instance validity of the thermal-hydraulic correlations. We also assumed that the high-pressure channels (working fluid side of evaporator and high-pressure side of recuperator) prefer a lower hydraulic diameter than the remaining channels. In addition, the cross-sectional flow area of the sink channel in the condenser was fixed to 100 cm^2. This resulted in a heat sink velocity of 2–3 m/s.

The evaporator calculation is somewhat simplified, as there is no geometry-based calculation on the heat source side. Instead, the heat-source pressure drop is neglected, a fixed heat transfer coefficient is assumed on the heat source side, and an area ratio of unity is set. The reason for this simplification is to reduce the number of free optimisation variables and thus model complexity, but also to avoid having to describe an objective function penalty caused by pressure loss in the heat source fluid, which is regarded here as being part of an industrial process. Geometry-based calculations of the heat-sink side of the condenser were included in the demonstration of the GHX-analysis, and the heat-sink pressure drop relates directly to the sink pump work.

3.3. Working fluids

International legislation, such as the Montreal and the Kyoto Protocols, place restrictions on the use of certain working fluids, and call for a shift from artificial refrigerants towards natural working fluids with low global-warming and ozone-depletion potential [21]. Hence, the natural propene, propane and n-Butane are selected for the demonstration of the GHX-analysis, in addition to the conventional refrigerant R134a as a baseline.

A mixture of 94.1 mol percent propene and 5.9 mol percent n-Butane was included to provide comparison between pure working fluids and a mixture. For simplicity, the composition of the mixture was optimised for a total UA-value of 150 kW/K and was used throughout the UA- and GHX-analysis.

3.4. Simulation results

The main results of the PPTD-, UA-, and GHX-analysis are shown in Fig. 4-Fig. 6, respectively. In the PPTD analysis, maximized net power output was plotted against total UA-value for the different working fluids; the UA-value was calculated based on the results of the cycle optimisation.Fig. 5.

The results of the UA-analysis are shown on the same axis, but power output has been optimised for a range of equal total UA-values, resulting in a “performance landscape” showing how the working fluids compare across a range of total UA-values, indicating the total size of the heat exchangers. The simulation points from the PPTD analysis are not necessarily located on the curves from the UA-analysis, since optimal PPTD's in the HXs could be different from the 5 K used in the PPTD analysis. Finally, results from the GHX-analysis are presented in a similar form to the UA-analysis, but note that net power is plotted against total HX area instead of total UA-value. The optimised n-Butane cycle is subcritical, and the remaining cycles are transcritical in all analyses.

In the PPTD analysis the mixture results in the highest net power, but simultaneously requires the largest UA-values. This illustrates that equal PPTD does not translate to equal UA or other expressions of HX size. The UA-analysis shows that all fluids achieve fairly similar net power outputs when given the same total UA budget. The exception is that the subcritical fluid n-Butane is slightly better for low UA-values, but starts to fall behind the others for larger UA budgets.

The general level of net power output is lower in the GHX-analysis than the UA-analysis and the working fluids rank differently compared to the UA-analysis. For instance, R134a is no longer one of the fluids with highest net power, and n-Butane shows poorer performance compared to the UA-analysis. Furthermore, the relative difference in net power between the fluids increased from the UA to the GHX-analysis.

Table 5 shows detailed optimisation results for all working fluid candidates with a total HX area of 60 m^2. The table shows that n-Butane

produces the lowest net power, but the optimised process is simpler than for the other working fluids since the recuperator is eliminated (i.e. the optimized recuperator length is zero). The table also shows that the optimized HX geometry differs with respect to working fluid. In particular, the condenser and evaporator for n-Butane are shorter, but designed with larger cross-sectional area compared to the corresponding HXs' with other fluids, resulting in a lower pressure drop and overall HTCs.

Table 6 shows detailed optimisation results for propene subjected to different constraint values for total HX area. The table shows that the optimised process has a larger expander pressure ratio and net power production as total HX area increases. The table also shows that the HX design and the HX area distribution are highly dependent on the total permitted HX area. For a total HX area of 20 m^2, the recuperator is not prioritised at all, while in the other cases the recuperator area is around 10% of the total HX area. Obviously, HX size (length and flow area) increases with increasing total HX area. However, for larger total HX areas, the condenser and evaporator are designed with lower pressure drops and overall HTCs.

4. Discussion

The previous section showed simulation results from the novel GHX-analysis and traditional thermodynamic analyses. The PPTD analysis predicted the largest thermodynamic performance for transcritical cycles of pure fluids and the zeotropic mixture, but these cycles also had the largest total UA-value. This in agreement with the results from Refs. [11,21]. The UA-analysis compared RCs at equal total UA-values across a wide range of HX sizes, represented by total UA-values, and demonstrated that the optimal working fluid depends on the permitted HX size.

The contribution of this work is the novel GHX-analysis, based on generic HX models and simultaneous optimisation of overall HTC vs. pressure drop trade-off and process parameters. The results from the GHX-analysis demonstrated that the trans-critical R134a and the sub-critical n-Butane cycle both were outperformed by the other options for the whole range of considered system sizes. In contrast, the thermodynamic analysis predicted a relatively better performance of the two solutions. The fact that the outcome of an analysis depends in the underlying methodology have already been confirmed by Quoilin et al. [26]. If this hypothetical demonstration case instead were an initial part of a system design procedure; the next step could be to exclude the R134a and n-Butane solutions and perform a thermo-economic analysis of the remaining promising solutions. In addition, the optimized HX parameters such as pressure drop, cross-sectional flow area and surface area ratio could be used to give a flying start on the HX design, with respect to geometric configuration, thermal-hydraulic design or HX type. Such information cannot be provided by a thermodynamic analysis alone. The GHX analysis also demonstrated that adding a recuperator is beneficial only when a sufficient large total HX area is permitted. This is a new criterion for the selection of recuperated vs. non-recuperated cycle since previous literature mentions a constrained outlet heat source temperature and a sufficient high heat source inlet temperature as the main criterions for adding a recuperator [10,14].

Fig. 7 shows selected results from the GHX-analysis for propene as working fluid. Evaporator duty, PPTD, working fluid pressure drop and overall HTC are given in data labels for total HX areas of 20 m^2, 60 m^2 and 100 m^2. The figure illustrates how the cycle optimisation effectively finds the best trade-off between different component and cycle losses subject to the active constraints. For the lowest total HX area, the optimisation chooses a fairly high pressure drop to obtain high overall HTC. In the trade-off between quantity (duty) and quality (temperature) of recovered energy, a small fraction of the available heat source is not captured. When the total HX area "budget" increases, a shift in both these trade-offs can be observed. Pressure drop and heat transfer coefficients decrease, and all the available heat in the heat source is recovered at higher exergy, as the average temperature differences are reduced, as reflected in decreasing PPTD.

The overall HTCs and working fluid pressure drops in the optimised condensers and evaporators from the GHX-analysis are shown in Fig. 8. The figure illustrates strong positive correlations between pressure drop and overall HTC in the evaporator and condenser when the total permitted HX area is changed, indicating that the optimal trade-off between heat transfer and pressure drop depends on the total permitted HX size.

Fig. 8 can also be used to understand the difference between the results of the UA- and GHX-analysis. The GHX-analysis includes exergy losses due to working fluid pressure drop, resulting in lower net power output compared to the UA-analysis, which neglects working fluid pressure drop. In addition, the GHX-analysis calculates the UA-value as the product of HX area and overall HTC. Hence, the RCs are not necessarily compared at equal total UA-values in the GHX-analysis, as is the case for the UA-analysis. Therefore, discrepancies between the results of the thermodynamic- and GHX-analyses are to be expected for fluids with different overall HTCs. As an example, consider the overall HTCs of R134a in Fig. 8. When the overall HTCs in the evaporator at equal total pressure drops are compared, all hydrocarbons have relatively similar values, which are larger than overall HTCs for R134a. R134a also has lower HTCs than the hydrocarbons in the condenser. This effect is the main reason why R134a (the best pure fluid from the UA-analysis) was outperformed by several hydrocarbons in the GHX-analysis.

A reason behind the poor performance of the n-Butane cycle is also indicated here. n-Butane had significantly lower operating pressures than the other fluids, and cycle performance is thus more sensitive to working fluid pressure drop. As shown in Table 5, the n-Butane evaporator and condenser were designed with larger cross-sectional area and shorter length compared to the other fluids. This results in a lower pressure drop and overall HTC for the butane heat exchangers as can be seen in Fig. 8.

The GHX-model represents an abstract heat exchanger that cannot be manufactured, which implicates that experimental verification of the GHX-model, other than experimental verification of the thermal-hydraulic correlations, is impossible. However, the optimised operating conditions and the pressure drops from the GHX-analysis could be applied as input for a HX type-specific design optimisation. In this case, the resulting heat transfer area from such an analysis could be compared with the HX area predicted by the GHX-model for evaluating the accuracy of the GHX-model with respect to estimating size of real heat exchangers. Whether the use of thermal-hydraulic correlations for circular channels are realistic for the final application, also depends on choice of HX technology at the later stage. However, the presented approach is based on the assumption that the trade-off between overall HTC and pressure is similar in nature across common HX types. Validation this assumption is suggested for future work.

The isentropic efficiency of the expander has a strong influence on the expander power and thereby the performance of the Rankine cycle. Further development of a generic RC analysis should therefore include a more detailed expander model capable of predicting performance based on fluid properties and operating conditions.

The accuracy of the optimisation in terms of finding the global optimal solution should also be discussed. The GHX-analysis included 12 optimisation variables and six non-linear constraints, which is obviously a challenging optimisation problem. Some of the optimisation variables in

Table 6 do not change monotonically with increasing total HX area. For instance, an increase in the evaporator length was expected when the total HX area was increased from 80 m^2 to 100 m^2 for propene. The decrease in the evaporator length for this case is due to the optimiser "getting stuck" in a local optimum in at least one of the two "total HX area" cases. However, the smooth monotonic curves of the net power output vs. total HX area in Fig. 6 indicate that the maximised net power

output is at least very close to the global maximum.

In this paper the GHC-analysis was applied to analyse different RC-systems at design conditions. However, the GHX-analysis can also be applied for "quasi steady-state" off-design analysis with, for instance, a heat source with time-dependent operating conditions. Such an analysis can be performed by optimising HX geometry for a given design condition and fixing this geometry in the off-design analysis.

5. Conclusions

Selection of fluid, cycle layout and component types are important issues when designing a Rankine cycle and the optimal outcome is very dependent on the target application. Thermodynamic analysis is a common methodology for screening multiple Rankine cycle options in terms of thermodynamic performance potential, but additional assumptions are required to estimate component sizes such as HX area. The GHX-analysis is presented as a more informative alternative method for screening or initial Rankine cycle analysis by introducing a generic heat exchanger (GHX) model. The GHX model does not represent a certain HX-type or even a manufacturable design, but applies fluid properties and a minimum amount of generic geometry parameters to estimate local heat transfer coefficients and pressure gradients. The GHX-analysis thus permits simultaneous optimization of process state points and the trade-off between overall heat transfer coefficient and pressure drop without relying on a certain HX-geometry concept. The GHX-analysis was demonstrated for analysing a single stage recuperated RC with different working fluids and HX sizes, and compared with pure thermodynamic approaches. The main conclusions drawn from this work are the following:

- Both thermodynamic- and GHX-analysis can be applied independently of the HX-type(s) under consideration. However, GHX-analysis provides a quantitative measure of HX size in terms of HX area, instead of the qualitative UA-value from the thermodynamic analysis.
- The optimal HX design predicted by the GHX-analysis (e.g. pressure drop and flow cross-sectional area) gives a "flying start" for designing heat exchangers for the target application.
- The trade-off between overall HTC and pressure drop is a compromise between exergy losses due to pressure drop and finite temperature difference between two fluids. The GHX-analysis demonstrates that the optimal trade-off is highly depended on the working fluid and on the total permitted HX area. Hence, the optimal pressure drop is an important parameter for determining the overall HTC, in addition to working fluid properties and flow-regimes.
- The present study focuses on presenting a methodology, rather than designing a Rankine cycle for a target application. However, it should be noted that the GHX-analysis is not limited to analysis at design operating conditions, but can also be applied to predict off-design behaviour in heat exchangers.

Declaration of Competing Interest

The authors declared that there is no conflict of interest.

Acknowledgement

The authors gratefully acknowledge the financial support from the Research Council of Norway (EnergiX grant no. 255016) for the COPRO project, and the user partners Equinor, Norway; Hydro Norway; Alcoa, Norway; GE Power Norway and FrioNordica, Norway.

Appendix A. Supplementary material

Supplementary data to this article can be found online at https://doi.org/10.1016/j.applthermaleng.2019.114566.

References

[1] S. Quoilin, et al., Techno-economic survey of Organic Rankine Cycle (ORC) systems, Renew. Sustain. Energy Rev. 22 (2013) 168–186.
[2] F. Tchanche, B.M. Pétrissans, G. Papadakis, Heat resources and organic Rankine cycle machines, Renew. Sustain. Energy Rev. 39 (2014) 1185–1199.
[3] M. Imran, et al., Recent research trends in organic Rankine cycle technology: A bibliometric approach, Renew. Sustain. Energy Rev. 81 (2018) 552–562.
[4] M. Astolfi, E. Martelli, L. Pierobon, Thermodynamic and technoeconomic optimization of Organic Rankine Cycle systems, Organic Rankine Cycle (ORC) Power Systems, Elsevier, 2017, pp. 173–249, , https://doi.org/10.1016/B978-0-08-100510-1.00007-7.
[5] K.H. Kim, H.J. Ko, K. Kim, Assessment of pinch point characteristics in heat exchangers and condensers of ammonia–water based power cycles, Appl. Energy 113 (2014) 970–981.
[6] J. Sarkar, Generalized pinch point design method of subcritical-supercritical organic Rankine cycle for maximum heat recovery, Energy 143 (Supplement C) (2018) 141–150.
[7] M. Chys, et al., Potential of zeotropic mixtures as working fluids in organic Rankine cycles, Energy 44 (1) (2012) 623–632.
[8] A. Schuster, S. Karellas, R. Aumann, Efficiency optimization potential in supercritical Organic Rankine Cycles, Energy 35 (2) (2010) 1033–1039.
[9] C. Vetter, H.-J. Wiemer, D. Kuhn, Comparison of sub- and supercritical Organic Rankine Cycles for power generation from low-temperature/low-enthalpy geothermal wells, considering specific net power output and efficiency, Appl. Therm. Eng. 51 (1) (2013) 871–879.
[10] R. Agromayor, L.O. Nord, Fluid selection and thermodynamic optimization of organic Rankine cycles for waste heat recovery applications, Energy Procedia 129 (Supplement C) (2017) 527–534.
[11] Y. Wu, Y. Zhu, L. Yu, Thermal and economic performance analysis of zeotropic mixtures for Organic Rankine Cycles, Appl. Therm. Eng. 96 (2016) 57–63.
[12] N.A. Lai, J. Fischer, Efficiencies of power flash cycles, Energy 44 (1) (2012) 1017–1027.
[13] H. Yu, D. Kim, T. Gundersen, A study of working fluids for Organic Rankine Cycles (ORCs) operating across and below ambient temperature to utilize Liquefied Natural Gas (LNG) cold energy, Energy 167 (2019) 730–739.
[14] J. Vivian, G. Manente, A. Lazzaretto, A general framework to select working fluid and configuration of ORCs for low-to-medium temperature heat sources, Appl. Energy 156 (2015) 727–746.
[15] Y.R. Li, et al., Effect of pinch point temperature difference on cost-effective performance of organic Rankine cycle, Int. J. Energy Res. 37 (15) (2013) 1952–1962.
[16] D. Maraver, et al., Systematic optimization of subcritical and transcritical organic Rankine cycles (ORCs) constrained by technical parameters in multiple applications, Appl. Energy 117 (2014) 11–29.
[17] A.A. Lakew, O. Bolland, Working fluids for low-temperature heat source, Appl. Therm. Eng. 30 (10) (2010) 1262–1268.
[18] J. Wang, M. Diao, K. Yue, Optimization on pinch point temperature difference of ORC system based on AHP-Entropy method, Energy 141 (2017) 97–107.
[19] H.-H. Zhu, K. Wang, Y.-L. He, Thermodynamic analysis and comparison for different direct-heated supercritical CO2 Brayton cycles integrated into a solar thermal power tower system, Energy 140 (2017) 144–157.
[20] Rohde, D., et al. Comparison of rankine cycle and trilateral flash cycle for power production from low temperature heat sources, in: Refrigeration Science and Technology, 2018.
[21] K. Braimakis, et al., Low grade waste heat recovery with subcritical and supercritical Organic Rankine Cycle based on natural refrigerants and their binary mixtures, Energy 88 (2015) 80–92.
[22] D. Walraven, B. Laenen, W. D'Haeseleer, Economic system optimization of air-cooled organic Rankine cycles powered by low-temperature geothermal heat sources, Energy 80 (2015) 104–113.
[23] D. Walraven, B. Laenen, W. D'haeseleer, Minimizing the levelized cost of electricity production from low-temperature geothermal heat sources with ORCs: Water or air cooled? Appl. Energy 142 (2015) 144–153.
[24] V.L. Le, et al., Thermodynamic and economic optimizations of a waste heat to power plant driven by a subcritical ORC (Organic Rankine Cycle) using pure or zeotropic working fluid, Energy 78 (Supplement C) (2014) 622–638.
[25] Y. Feng, et al., Thermoeconomic comparison between pure and mixture working fluids of organic Rankine cycles (ORCs) for low temperature waste heat recovery, Energy Convers. Manage. 106 (Supplement C) (2015) 859–872.
[26] S. Quoilin, et al., Thermo-economic optimization of waste heat recovery Organic Rankine Cycles, Appl. Therm. Eng. 31 (14) (2011) 2885–2893.
[27] S. Lecompte, et al., Part load based thermo-economic optimization of the Organic Rankine Cycle (ORC) applied to a combined heat and power (CHP) system, Appl. Energy 111 (2013) 871–881.
[28] F. Capra, E. Martelli, Numerical optimization of combined heat and power Organic Rankine Cycles – Part B: Simultaneous design & part-load optimization, Energy 90 (2015) 329–343.
[29] B. Dong, et al., Thermodynamic and economic analysis of zeotropic mixtures as working fluids in low temperature organic Rankine cycles, Appl. Therm. Eng. 132 (2018) 545–553.
[30] D. Walraven, B. Laenen, W. D'haeseleer, Comparison of shell-and-tube with plate heat exchangers for the use in low-temperature organic Rankine cycles, Energy Convers. Manage. 87 (2014) 227–237.
[31] H.T. Walnum, et al., Modelling and simulation of CO2 (carbon dioxide) bottoming cycles for offshore oil and gas installations at design and off-design conditions,

Energy 59 (2013) 513–520.
[32] D. Rohde, et al., Heat recovery from export gas compression: Analyzing power cycles with detailed heat exchanger models, Appl. Therm. Eng. 60 (1) (2013) 1–6.
[33] V. Gnielinski, New equations for heat and mass transfer in turbulent pipe and channel flow, Int. Chem. Eng. 16 (2) (1976) 359–368.
[34] W.N. Selander, Explicit formulas for the computation of friction factors in turbulent pipe flow. 1978: Chalk River, Ontario, Canada: Chalk River Nuclear Labs.
[35] L.D. Boyko, G.N. Kruzhilin, Heat transfer and hydraulic resistance during condensation of steam in a horizontal tube and in a bundle of tubes, Int. J. Heat Mass Transf. 10 (3) (1967) 361–373.
[36] D.L. Bennet, J.C. Chen, Forced convective boiling in vertical tubes for saturated pure components and binary mixtures, AIChE J. 26 (3) (1980) 454–461.
[37] L. Silver, Gas cooling with aqueous condensation, Trans. Inst. Chem. Eng. 25 (1947) 30–42.
[38] J.K.G. Bell, M. A., An approximate generalized design method for multicomponent/partial condensers. AIChE Symp. Ser., vol. 69, 1973, pp. 72–79.
[39] L. Friedel, Improved friction pressure drop correlations for horizontal and vertical two-phase pipe flow, vol. 18, 1979, pp. 485–491.
[40] E. Lemmon, M. Huber, M. M., NIST reference database 23: reference fluid thermodynamic and transport propeties-REFPROP, version 9.1, Standard Reference Data Propgram, 2013.
[41] K. Schittkowski, NLPQL: A fortran subroutine solving constrained nonlinear programming problems, Ann. Oper. Res. 5 (2) (1986) 485–500.

A.2 Paper II

Gradient Based Design Optimization of a Radial Inflow Turbine

Brede A. L. Hagen, Matteo Cavo, Trond Andresen, Petter Nekså, in *IIR Rankine 2020 Conference*, 2020.

PAPER ID: 1143
DOI: 10.18462/iir.rankine.2020.1143

Gradient Based Design Optimization of a Radial Inflow Turbine

Brede A. L. Hagen[(a)], Matteo Cavo[(b)], Trond Andresen[(c)], Petter Nekså[(c,a)]

[(a)] Norwegian University of Science and Technology – Department of Energy and Process Engineering
Trondheim, 7034, Norway, brede.hagen@ntnu.no
[(b)] University of Genoa
Genoa, 16126, Italy, matteo.cavo@edu.unige.ito
[(c)] SINTEF Energy Research
Trondheim, 7034, Norway, petter.neksa@sintef.no

ABSTRACT

The expander is one of the key components of an ORC as the cycle efficiency strongly depends on the expander efficiency. This paper presents a method for design optimization of a radial inflow turbine (RIT) using a mean-line model. The novelty of this work lies in the equation-based formulation of the mathematical problem, which enables the use of an efficient gradient based method for optimization. This means that there is no distinction between real decision variables such as specific speed and velocity ratio, and parameters that are unknown a priori such as rotor outlet entropy and velocity. Constraints are imposed to ensure conservation of mass, and to ensure a feasible and consistent design, and the objective is to maximize the total-to-static efficiency. The main results showed an average CPU time less than one second and a success rate of 80% for converging to the global optimum when the independent variables were given random start values. We therefore recommend the proposed method for preliminary RIT-design or to be integrated into an ORC system design model enabling for instance working fluid screening with fluid-dependent expander efficiency.

Keywords: Radial Inflow Turbine; Mean-line model; Optimization; ORC; Preliminary design

1. INTRODUCTION

The Radial inflow turbine (RIT) is a promising expander technology for Organic Rankine Cycles (ORCs). Advantages of the RIT compared to the more common axial turbine is the ease of manufacturing, fewer stages and robustness (Dixon and Hall, 2014).

The traditional ORC analysis involves using a fixed, pre-defined expander efficiency (Song et al., 2016), (Lazzaretto and Manente, 2014). However, this might lead to misleading result because the attainable expander efficiency depends on the expander technology, the operating conditions and the working fluid (Da Lio et al., 2017). Song et al. (2016) performed two separate working fluid screening analyses; One analysis with constant expander efficiency and one analysis using a mean-line RIT model for predicting the expander efficiency. Their results demonstrated that inclusion of the mean-line model significantly changed the result compared to the fixed-efficiency analysis since the RIT efficiency differed by up to 11 percentage point among the considered working fluids.

Predicting expander efficiency based on working fluid properties can be performed in a less computationally expensive way by using a generic efficiency map created by a mean-line model assuming an ideal gas as the working fluid. Lazzaretto and Manente (2014) used efficiency maps from (Perdichizzi and Lozza, 1987) and (Macchi and Perdichizzi, 1981) for predicting the design performance of RITs and axial turbines respectively in their ORC analyses. Although, these maps predict a consistent trend in the attainable expander efficiency with respect to turbine size and pressure ratio, the accuracy with respect to real gas behavior could be questioned because the expansion in an ORC often starts close to the critical pressure of the working fluid. Another limitation of these maps is that they provide the design point efficiency only and are therefore not suitable for preliminary RIT design or off-design analyses.

Several mean-line models for the RIT exist, and the reader is referred to text books on turbine design such as (Moustapha et al., 2003), (Aungier, 2005), or (Dixon and Hall, 2014) for a complete overview of the topic.

Recent literature on RIT mean-line models for ORC application focus accuracy because most existing loss-correlations rely on data for low pressure-ratio RITs. Persky and Sauret (2019) evaluated more than 1.5 million different sets of rotor loss correlations for RITs expanding CO_2 and R143a and identified the set that gave the best agreement with corresponding CFD-simulations. Meroni et al. (2018) calibrated a given set of loss-correlations towards published experimental data on six high pressure ratio RITs with relevance to ORC operating conditions.

Little attention is paid in the open literature to the various options for solving the preliminary RIT design optimization problem. Based on the above-mentioned literature we believe the conventional approach involves treating the mean-line model as a "black box" that takes the real decision variables such as specific speed and velocity ratio as input and solves the remaining unknown parameters to ensure conservation of mass and a consistent design. The optimization is performed by multiple evaluation of the "black box" model; either by manually adjusting the design variables or by using a direct search algorithm for optimizing the design variables. A well-documented example of such an approach is described in (Da Lio et al., 2017).

The intention of this work is to present an alternative and more efficient treatment of the preliminary RIT design optimization problem. The method is inspired by the work by Agromayor and Nord (2019) for design optimization of axial turbines. The method involves optimizing the real decision variables and the unknown parameters simultaneously using a gradient based optimization algorithm. This means for instance that conservation of mass is ensured by imposing equality constraints and that a consistent design only occurs when the optimization algorithm is finished with a feasible result.

2. METHODOLOGY

The proposed method for RIT design optimization consists of a single non-linear constrained optimization problem to be solved by a gradient based optimization algorithm, as is illustrated in Figure 1. Details on the components of this method is outlined in the remainder of this section.

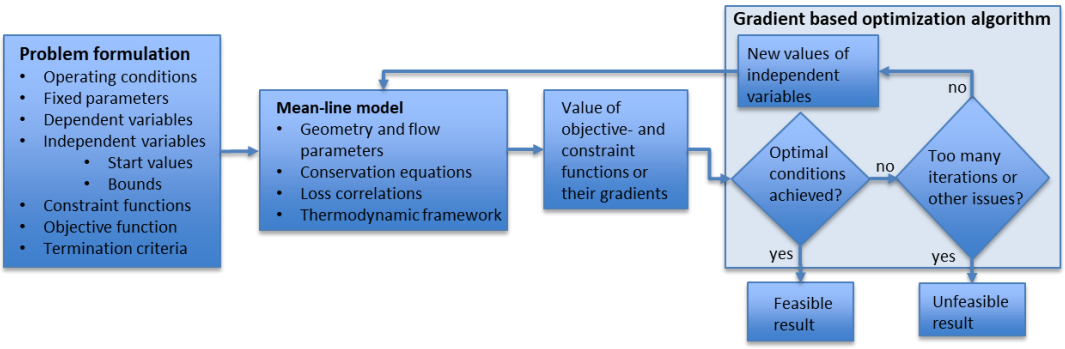

Figure 1: Overview of the proposed method for gradient based RIT design optimization

2.1. Mean-line model

The mean-line model is implemented in the programming language C and consider the nozzle, interspace and the rotor as illustrated in Figure 2. The figure also indicates the involved geometry parameters. The mean-line model also requires knowledge of the flow parameters and thermophysical properties along the mean-line through the turbine. The flow parameters consist of the nozzle outlet velocity (angle and absolute value), and the velocity triangles at rotor inlet and outlet illustrated in Figure 3. Blockage factors are neglected, which means that blade-blockage and boundary layer effects are neglected for mass flow rate calculations. The effective cross-sectional flow areas can thus be computed by Eq. (1).

$$A_i = 2\pi r_i b_2, \quad \text{i=2,3}$$
$$A_4 = \pi\left(r_{4s}^2 - r_{4h}^2\right) \qquad \text{Eq. (1)}$$

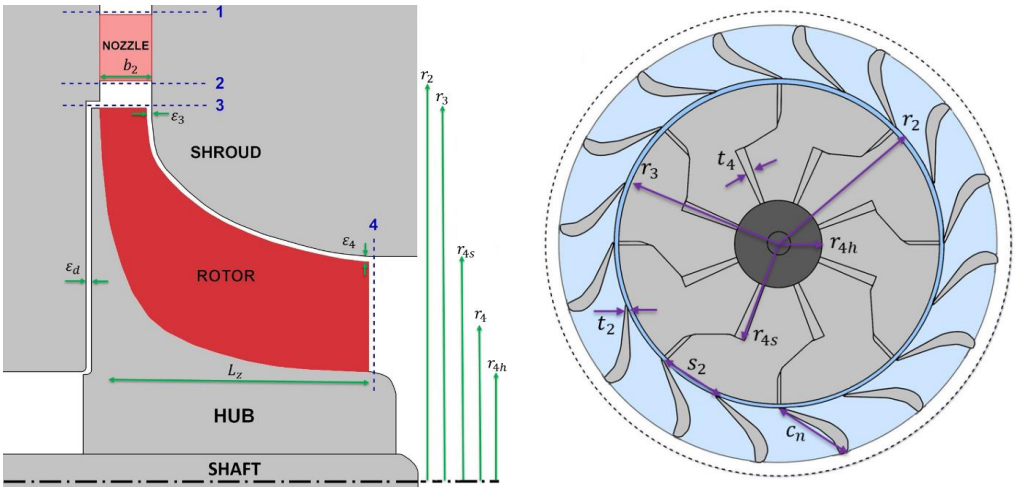

a) View of the meridional channel **b) View in the axial direction**

Figure 2: Geometry parameters used in the mean-line model

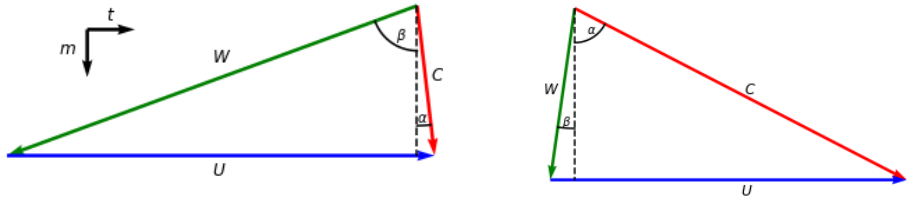

a) Rotor outlet **b) Rotor inlet**

Figure 3: Flow parameters used in the mean-line model except for the nozzle outlet velocity, which is very similar to the absolute velocity at rotor inlet (no rotational velocity U)

The enthalpy distribution through the turbine is calculated by conservation equations. Nozzle outlet enthalpy is calculated by conservation of energy through the nozzle, Eq. (2)

$$h_2 = h_{01} - \frac{1}{2}C_2^2 \qquad \text{Eq. (2)}$$

The rotor inlet enthalpy and velocity are calculated by conservation of angular momentum (Eq. (3)) and energy (Eq. (4)) through the interspace.

$$C_{3t} = \frac{r_2}{r_3}C_{2t} \qquad \text{Eq. (3)}$$

$$h_3 = h_{01} - \frac{1}{2}(C_{3m}^2 + C_{3t}^2) = h_{01} - \frac{1}{2}C_3^2 \qquad \text{Eq. (4)}$$

The rotor outlet enthalpy is calculated by conservation of rothalpy through the rotor, Eq. (5).

$$h_4 = h_3 + \frac{1}{2}(W_3^2 - U_3^2) - \frac{1}{2}(W_4^2 - U_4^2) \qquad \text{Eq. (5)}$$

The thermophysical properties of the working fluid are calculated with Refprop 10.0 (Lemmon et al., 2018).

Many configurations of loss-correlations are possible in a mean-line model because there exist multiple correlations for each loss-mechanism occurring in the RIT. This work employs the set of loss-correlations presented by Meroni et al. (2018) because it was calibrated against experimental data for high pressure ratio

RITs. This set consist of 10 correlations considering loss-mechanisms occurring in the nozzle, interspace and the rotor, including post expansion which activates when the nozzle and/or rotor outlet velocity exceeds speed of sound. Since a diffuser model is not included, it is assumed that all the kinetic energy leaving the rotor is lost. The rotor incidence loss is neglected because it is assumed that the turbine can be designed with zero incidence, as suggested in (Moustapha et al., 2003).

2.2. Problem formulation

The main novelty of the proposed method is the optimization formulation shown in Table 1. The independent variables govern geometry, flow and thermodynamic parameters and finding the optimal value of these is the only mathematical problem to be solved (except explicit calculations and numerical routines within the thermodynamic framework), because the imposed equality constraints ensure conservation of mass and a consistent design. All independent variables are constrained between a lower and an upper bound to ensure a feasible design. In addition, an inequality constraint is imposed to avoid a too large increase in the rotor cross-sectional flow area, as suggested by Da Lio et. al (2017). For numerical reasons it is an advantage to bring all the variables and constraints to the same order of magnitude. Therefore, the spouting velocity $c_0 = (2\Delta h_{is})^{0.5}$ is used as a velocity scale, the angles are unit-converted to radians, and the constraint- and objective functions are written in a non-dimensional form.

Table 1. Formulation of the RIT design optimization problem

Independent variables			
Nozzle outlet velocity	C_2/c_0	$\in$	$[0.1,\ 0.8]$
Nozzle outlet flow angle	α_2	$\in$	$[30°,\ 80°]$
Rotor inlet meridional velocity	C_{3m}/c_0	$\in$	$[0.02,\ 0.4]$
Normalized rotor outlet velocity	W_4/c_0	$\in$	$[0.1,\ 0.9]$
Rotor outlet flow angle	β_4	$\in$	$[-70°, -20°]$
Specific speed	$\omega_s = \omega\dot{V}_{4,is}^{1/2}/\Delta h_{is}^{3/4}$	$\in$	$[0.3, 0.8]$
Velocity ratio	$v_s = U_3/c_0 = \omega r_3/c_0$	$\in$	$[0.5, 0.8]$
Rotor radius ratio (shroud/inlet)	r_{4s}/r_3	$\in$	$[0.4,\ 0.7]$
Rotor radius ratio (hub/shroud)	r_{4h}/r_{4s}	$\in$	$[0.4,\ 0.8]$
Blade height to radius ratio	b_2/r_3	$\in$	$[0.04,\ 0.34]$
Outlet entropy[a,b]	s_{out}/s_1	$\in$	$[1.0, s_{ref}/s_1]$
Constraint functions			
Consistent outlet pressure	$1.0 - p(h_4, s_4)/p_4 = 0$		
Consistent outlet enthalpy[a]	$\dfrac{h_{out} - h(p_{out}, s_{in}) - \sum\Delta h_{loss}}{0.5\ W_{out}^2} = 0$		
Conservation of mass[c]	$1.0 - \rho(h, s)W_m A/\dot{m} = 0$		
Maximum rotor area ratio	$2.5 - A_4/A_3 \geq 0$		
Objective function			
Maximize total-to-static efficiency	$\eta_{ts} = \dfrac{h_{01} - h_{04}}{\Delta h_{is}}$		

[a] *Two values (nozzle and rotor)*

[b] *Reference entropy, s_{ref}, is the resulting outlet entropy when* $\eta_{ts} = 0.5$

[c] *Three values (Nozzle outlet, rotor inlet and rotor outlet)*

Some parameters are not suitable for optimization because the total-to-static efficiency is a monotonic function of them, and/or because their values are constrained by factors not included in the model, such as manufacturing limits. Instead, these parameters are either fixed or calculated from the set of independent variables during the optimization. The value of the fixed parameters and formulas for the dependent variables are shown in Table 2, and most of these were suggested default values from Aungier (2005).

2.3. Optimization algorithm and termination criterion

The optimization problem presented in the previous section contains 12 independent variables and 7 non-linear constraints, which is a challenging mathematical problem. However, since the mean-line model is written in an equation-oriented fashion (inner iterations are limited to thermodynamic calculations only) an efficient gradient based method can be applied (Astolfi et al. 2017).

Table 2. Value of fixed parameters and formulas for the dependent variables

Parameter	Symbol	Value	Source
Nozzle blade trailing edge thickness	t_2	$0.012c_n$	(Aungier, 2005)
Rotor blade trailing edge thickness	t_4	$0.02r_4$	(Aungier, 2005)
Rotor axial length	L_z	$1.5(r_{4s} - r_{4h})$	(Aungier, 2005)
Blade tip clearances	ε_i (i=3,4)	$\max(0.4\,mm, 0.02b_i)$	
Disc clearance	ε_d/r_3	0.05	
Nozzle chord to pitch ratio	c_n/s_2	1.33	(Aungier, 2005)
Interspace distance	$r_2 - r_3$	$2b_2 \cos\alpha_2$	(Aungier, 2005)
Number or rotor blades	Z_r	$12 + 0.03(\alpha_2 - 57°)^2$	(Aungier, 2005)
Number of nozzle blades	Z_n	$Z_r + 3$	

The optimization algorithm applied in this work is the Sequential Quadratic Programming (SQP) method, NLPQL (Schittkowski, 1985). Gradients are calculated using a second order central difference approximation for numerical differentiation. The KKT optimal criterion is set to 1.0E-7. The maximum number of iterations are set to 80. This means that NLPQL return an unfeasible result if the KKT optimal criterion have not been met within 80 iterations or other issues occurs, see (Schittkowski, 1985) for details.

3. RESULTS

A design optimization of a RIT for a hypothetical ORC have been performed. The working fluid is propane and the 862-kW heat source enter the heat recovery heat exchanger at 150 °C. The turbine operating conditions are obtained from (Hagen et al., 2020) and showed in Table 3 together with selected result from the optimization.

Table 3. Operating conditions and selected results from the RIT design optimization

Operating conditions		Optimized geometry and performance					
T_{01} [C]	131.57	r_2	43.5 mm	t_2	0.19 mm	v_s	0.62
$\dot{m}$ [kg/s]	1.99	c_n	16.3 mm	t_4	0.84 mm	ω_s	0.41
p_{01} [bar]	46.62	Z_n	22	ε_d	2.11 mm	η_{ts}	0.849
p_4 [bar]	9.58	α_2	72.6°	ω	57142 rpm	Shaft power	142 kW

Loss distribution, rotor geometry and velocity triangles from the design optimization are shown in Figure 4. The single most important loss-mechanism is the rotor clearance loss which accounts for around 4 percentage point reduction in the total-to-static efficiency. The absolute velocity at the nozzle outlet and rotor inlet are supersonic, which resulted in a post expansion loss at the nozzle outlet. The ratio between the rotor shroud and inlet radius (r_{4s}/r_3) was the only independent variable with an active variable bound. This variable went to its upper bound of 0.7, which was suggested by Aungier (2005).

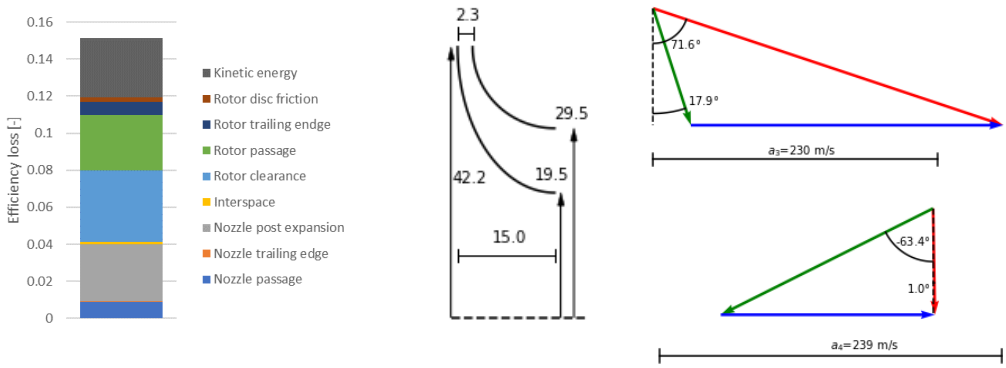

Figure 4: Loss distribution, rotor geometry (values in mm) and velocity triangles for the optimized RIT

A total of 100 optimizations, each with random start values of the independent variables were carried out to evaluate the risk of converging to local optimum and to assess the robustness of the optimization formulation. The optimized variable values and maximized efficiency from the 80 optimizations that returned a feasible result are shown in Figure 5. The feasible optimization results are quite consistent since all optimized variable values are within ± 0.1 % and the variation in the objective function is smaller than 1E-7. This is a strong indication that all feasible optimizations converged very close to the global optimum, i.e. that the mathematical optimization problem contains none or few local optimums.

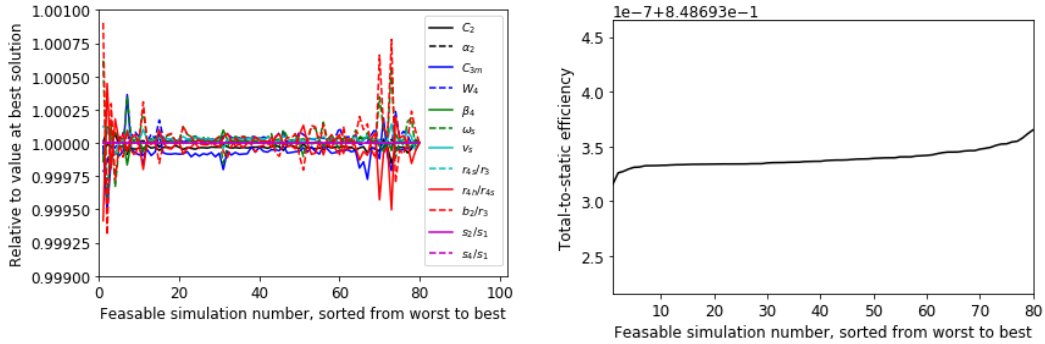

a) Independent variables **b) Objective function**

Figure 5: Results from 80 of the 100 optimizations with random start value of the independent variables that converged to a feasible solution. Average CPU time per optimization is 0.83 s

A comparison between maximized RIT efficiency from the presented methodology and results from the open literature has also been performed. Figure 6 shows two RIT performance maps with R245fa as working fluid and an outlet pressure of 1.976 bar. Both maps were generated by performing multiple RIT optimizations with different inlet conditions. Figure 6a shows the maximized total-to-static efficiency using the presented methodology for different size parameters, $SP = \dot{V}_{4s}^{0.5}/\Delta h_s^{0.25}$ and isentropic volume ratios, $VR = \dot{V}_{01}/\dot{V}_{4s}$. Figure 6b shows a similar performance map that are taken from (Da Lio et al., 2017). Both maps predict an increasing efficiency with increasing SP. Otherwise there are some notable differences. Both maps show a VR that maximizes the efficiency (at a constant SP), but the proposed method predict a much lower value of this optimum VR. The proposed method gives larger efficiency for VR less than 3.5-4 and a lower efficiency for larger VRs, i.e. a larger penalty of the attainable total-to-static efficiency for increasing VR.

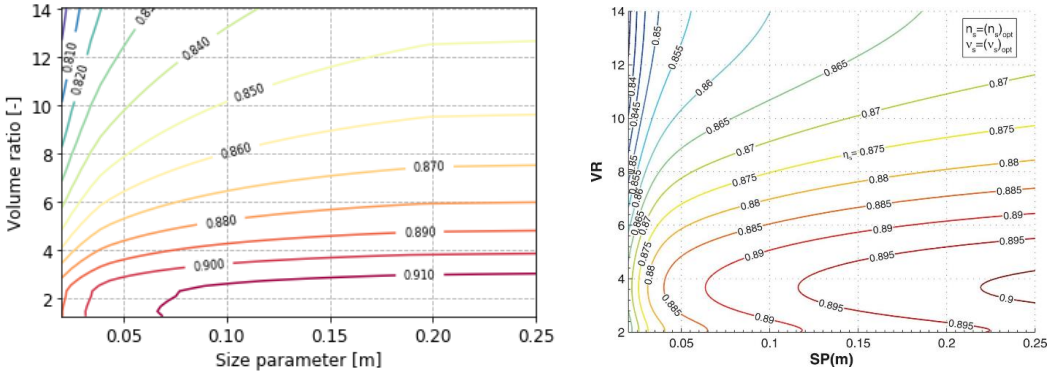

a) This work **b) Figure from Da Lio et al. (2017)**

Figure 6: Maximized total-to-static efficiency with R245fa as working fluid and outlet pressure of 1.976 bar for different design inlet conditions

4. DISCUSSION

The results show that the presented methodology for RIT design optimization is fast, robust and converges to the global optimum. The main limitation is the uncertainty which is at least as much as the discrepancy between the two performance maps in Figure 6, which is largest for the largest VRs and smallest SPs (up to 4%). One source of uncertainty is the fixed parameters and the dependent variables from Table 2. In particular, the blade tip clearances contribute to uncertainty because they directly affect one of the most important loss mechanisms in the RIT and because their lower bound is constrained by manufacturing difficulty (Dixon and Hall, 2014). We believe that the main source of uncertainty is related to the accuracy of the loss correlations, which is an issue for all mean-line models. Meroni et al. (2018) reports a maximum deviation in efficiency of 2.83% between their calibrated mean-line model and the experimental data used for calibration, and highlights that a larger uncertainty is expected for turbines operating with different characteristics (geometry and operating conditions) than those used for calibration. A logical next step is therefore to validate the applied loss-correlations towards more experimental data. This requires modifications of the optimization formulation from Table 1 in such a way that the mass flow rate and the efficiency is predicted for a given turbine geometry and operating conditions (working fluid, inlet state, and pressure-ratio). This will also enable the calculation of RIT off-design behavior and performance and is left for future work.

5. CONCLUSION

Estimating the expander efficiency considering both fluid properties and operating conditions is a requirement for performing realistic ORC analyses. This paper presents an effective method for preliminary design and performance estimation of a Radial inflow turbine (RIT) using a mean-line model. The novelty of this work is the equation-oriented formulation of the mean-line model that enables use of an efficient gradient based algorithm for optimization. The demonstration of the proposed method showed an average optimization time less than one second and a success rate of 80% of hitting the global optimum when the independent variables were given random start values. We therefore recommend the proposed method for preliminary RIT-design or to be integrated into an ORC system design model for predicting the expander design efficiency. Future work involves extending the presented methodology to also predict RIT performance and behavior for a given geometry and operating conditions. This will enable further experimental validation of the mean-line model and RIT off-design analysis.

ACKNOWLEDGEMENTS

This publication has been funded by HighEFF - Centre for an Energy Efficient and Competitive Industry for the Future, an 8-years' Research Centre under the FME-scheme (Centre for Environment-friendly Energy Research, 257632/E20). The authors gratefully acknowledge the financial support from the Research Council of Norway and user partners of HighEFF.

The authors also greatly acknowledge the discussions with Roberto Agromayor regarding formulation of the Radial Inflow turbine design optimization problem.

NOMENCLATURE

a	Speed of sound ($m \times s^{-1}$)	s	Specific entropy; Blade pitch ($J \times kg^{-1} \times K^{-1}$); (m)
A	Cross sectional flow area (m^2)	SP	Size parameter (m)
b	Blade height (m)	t	Blade thickness (m)
c	Blade chord length (m)	T	Temperature (K)
c_0	Spouting velocity ($m \times s^{-1}$)	U	Rotational velocity ($m \times s^{-1}$)
C	Absolute velocity ($m \times s^{-1}$)	v_s	Velocity ratio (-)
h	Specific enthalpy ($J \times kg^{-1}$)	VR	Volume ratio (-)
$\dot{m}$	Mass flow ($kg \times s^{-1}$)	$\dot{V}$	Volume flow rate ($m^3 \times s^{-1}$)
p	Pressure (Pa)	W	Relative velocity ($m \times s^{-1}$)
r	Radial distance from shaft center (m)	Z	Number of blades (-)
		Greek	
α	Absolute flow angle (rad)	η_{ts}	Total-to-static efficiency (-)
β	Relative flow angle (rad)	ρ	Working fluid density ($kg \times m^{-3}$)
ε	Clearance (m)	ω	Rotational speed ($rad \times s^{-1}$)
		Subscripts	
0	Total state	m	Meridional component
1-4	Positions along the mean-line, Figure 2a	n	Nozzle
h	Hub	out	Outlet
in	Inlet	s	Specific or shroud
is	Isentropic	t	Tangential component

REFERENCES

Agromayor, R., and Nord, L. O. (2019). Preliminary Design and Optimization of Axial Turbines Accounting for Diffuser Performance. International Journal of Turbomachinery, Propulsion and Power, 4(3), 32.

Astolfi, M., Martelli, E., Pierobon, L. (2017). Thermodynamic and technoeconomic optimization of Organic Rankine Cycle systems. Organic Rankine Cycle (ORC) Power Systems, 173–249.

Aungier, R. H. (2005). Turbine aerodynamics: Axial-flow and radial-inflow turbine design and analysis. New York: ASME Press.

Da Lio, L., Manente, G., Lazzaretto, A. (2017). A mean-line model to predict the design efficiency of radial inflow turbines in organic Rankine cycle (ORC) systems. Applied Energy, 205, 187–209.

Dixon, S. L., and Hall, C. A. (2014). Fluid Mechanics and Thermodynamics of Turbomachinery. In Fluid Mechanics and Thermodynamics of Turbomachinery. Oxford, UK: Butterworth-Heinemann.

Hagen, B. A. L., Nikolaisen, M., Andresen, T. (2020). A novel methodology for Rankine cycle analysis with generic heat exchanger models. Applied Thermal Engineering, 165, 114566.

Lazzaretto, A., Manente, G. (2014). A new criterion to optimize ORC design performance using efficiency correlations for axial and radial turbines. International Journal of Thermodynamics, 17(3), 173–181.

Lemmon, E. W., Bell, I. H., Huber, M. L., McLinden, M. O. (2018). NIST Standard Reference Database 23: Reference Fluid Thermodynamic and Transport Properties-REFPROP, Version 10.0, National Institute of Standards and Technology.

Macchi, E., Perdichizzi, A. (1981). Efficiency Prediction for Axial-Flow Turbines Operating with Nonconventional Fluids. Journal of Engineering for Power, 103(4), 718–724.

Meroni, A., Robertson, M., Martinez-Botas, R., Haglind, F. (2018). A methodology for the preliminary design and performance prediction of high-pressure ratio radial-inflow turbines. Energy, 164, 1062–1078.

Moustapha, H., Zelesky, M. F., Baines, N. C., Japikse, D. (2003). Axial and Radial Turbines. Vermont, USA: Concepts NREC.

Perdichizzi, A., Lozza, G. (1987). Design Criteria and Efficiency Prediction for Radial Inflow Turbines. Gas Turbine Conference and Exhibition, 1–9. Anaheim: ASME.

Persky, R., Sauret, E. (2019). Loss models for on and off-design performance of radial inflow turbomachinery. Applied Thermal Engineering, 150, 1066–1077.

Schittkowski, K. (1985). NLPQL: a FORTRAN subroutine solving constrained nonlinear programming problems. Annals of Operations Research, 5(1–4), 485–500.

Song, J., Gu, C., Ren, X. (2016). Influence of the radial-inflow turbine efficiency prediction on the design and analysis of the Organic Rankine Cycle (ORC) system. Energy Conversion and Management, 123, 308–316.

A.3 Paper III

Equation-Oriented Methods for Design Optimization and Performance Analysis of Radial Inflow Turbines

Brede A. L. Hagen, Roberto Agromayor, Petter Nekså, *Energy*, vol. 237, no. 121596, 2021.

DOI: https://doi.org/10.1016/j.energy.2021.121596

Energy 237 (2021) 121596

Contents lists available at ScienceDirect

Energy

journal homepage: www.elsevier.com/locate/energy

Equation-oriented methods for design optimization and performance analysis of radial inflow turbines

Brede A.L. Hagen [a, *], Roberto Agromayor [a], Petter Nekså [a, b]

[a] Department of Energy and Process Engineering, NTNU – Norwegian University of Science and Technology, Kolbjørn Hejes Vei 1B, NO-7491, Trondheim, Norway
[b] SINTEF Energy Research, Sem Sælands 11, NO-7465, Trondheim, Norway

ARTICLE INFO

Article history:
Received 22 January 2021
Received in revised form
10 June 2021
Accepted 23 July 2021
Available online 28 July 2021

Keywords:
Mean-line model
Gradient-based optimization
Choked flow
Organic Rankine cycle
Model validation

ABSTRACT

This paper presents methods for design optimization and performance analysis of radial inflow turbines. Both methods are formulated in an equation-oriented manner and involve a single mathematical problem that is solved by an efficient, gradient-based optimization algorithm. In addition, the comparison of the model output with experimental data showed that the underlying mean-line flow model accurately predicts the variation of mass flow rate and isentropic efficiency as a function of the pressure ratio, rotational speed, and nozzle throat area. Moreover, the capabilities of the proposed methods were demonstrated by carrying out the preliminary design and performance prediction of the radial inflow turbine of an organic Rankine cycle. The results indicate that the design optimization method converges to the global optimum solution, regardless of the start values for the independent variables. In addition, the performance maps generated by the performance analysis method are physically consistent and agree with general findings from experimental data reported in the open literature. Considering the accuracy, robustness and low computational cost of the proposed methods, they can be regarded as a powerful tool for the preliminary design and performance prediction of radial inflow turbines, either as a standalone component or as part of a larger system.

1. Introduction

The Rankine cycle using an organic working fluid, conventionally referred to as the Organic Rankine Cycle (ORC), is an attractive technology for power production from low-temperature heat sources [1]. The ORC is currently applied for power production from waste heat [2] and renewable energy sources such as biomass combustion [3], concentrated solar energy [4] and geothermal energy [5]. Despite these energy sources could provide a significant fraction of the world's power demand [6], the full potential of ORC power systems has not yet been realized because the specific investment cost of this technology is relatively high compared with that of conventional power plants based on the combustion of fossil fuels [7]. Therefore, a key factor to enable further utilization of the ORC technology, and thus facilitate a reduction of CO_2 emissions, is to increase its cost-effectiveness.

One way to achieve this in applications for which the heat source or sink characteristics vary with time is to account for the off-design performance of the system during the design phase. For instance, Capra and Martelli [8] demonstrated that a design optimization that takes into account the off-design performance of the Rankine cycle can significantly increase the cost-effectiveness of the system with respect to a conventional design approach that only accounts for the system performance at the nominal operating point. More specifically, Capra and Martelli [8] applied the two aforementioned methods to design a combined heat and power Rankine cycle and showed that the former resulted in up to 22 % higher annual profit than the latter [8].

In order to account for the off-design performance of the Rankine cycle during the design phase, it is necessary to resort to accurate performance prediction methods for each of its components. In this context, the expander model is of key importance because the performance of this component has a strong influence on the mass flow rate and efficiency of the system. The importance of the expander efficiency prediction for ORC design optimization is illustrated by Song et al. [9], who performed two separate working fluid screening analyses; one using a prescribed expander efficiency and the other using a mean-line turbine model to predict the

* Corresponding author.
E-mail address: brede.hagen@ntnu.no (B.A.L. Hagen).

https://doi.org/10.1016/j.energy.2021.121596

Nomenclature

Latin symbols

a	Speed of sound [m/s]
A	Cross sectional flow area [m^2]
b	Blade height [m]
c	Blade chord length [m]
C	Absolute velocity [m/s]
C_0	Spouting velocity [m/s]
c_i	Rankine cycle state points
h	Specific enthalpy [J/kg]
k	Ratio of specific heat capacities [−]
$K_{p1}, K_{p2}, K_{p3}, K_{in}$	Loss model calibration coefficients [−]
L_z	Rotor axial length [m]
Ma	Relative Mach number, $Ma = W/a$ [−]
o	Throat opening [m]
p	Pressure [Pa]
r	Radial distance from shaft [m]
s	Specific entropy [J/kg K], Blade pitch [m]
t	Blade thickness [m]
U	Rotational velocity [m/s]
W	Relative velocity [m/s]
x_0	Independent variable − start value [−]
x_l	Independent variable − lower bound [−]
x_u	Independent variable − upper bound [−]
Z	Number of blades [−]

Greek symbols

α	Absolute flow angle [rad]
β	Relative flow angle [rad]
δ	Deviation angle [rad]
Δh	Specific work reduction due to loss [J/kg]
η	Total-to-static efficiency [−]
ε	Clearance [m]
ε	Convergence criterion [−]
ν	Velocity ratio [−]
μ	Dynamic viscosity [Pa s]
ρ	Density [kg/m^3]
ω	Rotational speed [rad/s]

Subscripts

0	Total state
1−6	RIT expansion state points
b	Blade
cl	Clearance loss
corr	Corrected
d	Design value
df	Disc friction loss
h	Hub
i	Incidence loss; State point index
int	Interspace loss
l	Loss
m	Meridional direction
n	Nozzle
opt	Optimal
out	Outlet of a blade row
p	Passage loss
r	Rotor
ref	Reference
s	Shroud; Specific
su	Supersonic loss
t	Tangential direction
te	Trailing edge loss
th	Throat of a blade row

Abbreviations

KKT	Kerush Kuhn Tucker
ORC	Organic Rankine Cycle
RIT	Radial Inflow Turbine
RMS	Root mean square

expander efficiency at its design point. Their results showed that the inclusion of the mean-line model can change the optimal working fluid in terms of net power output and that the predicted expander efficiency can differ up to 11% points among the working fluids considered. Expander performance prediction is arguably even more important for off-design analyses because both the expander efficiency and mass flow rate can change when the operating conditions are modified. As an example of this, Chatzpoulou et al. [10] performed off-design analyses of an ORC converting heat from an internal combustion engine into power. They considered a constant expander efficiency and a variable efficiency predicted by a piston expander model, and they found that the analyses that assumed a constant expander efficiency led to a net power underestimation of up to 17 %.

Among the different architectures available for ORC expanders, the Radial Inflow Turbine (RIT) is particularly promising thanks to its high-compactness and its capability to accommodate a large pressure ratio in a single stage [11]. In addition, the RIT can be equipped with movable nozzle blades, known as variable guide vanes, that can modify the nozzle throat area and the nozzle exit flow angle by rotating around a pivot point [12,13]. As a result, variable-geometry RITs offer more flexibility during off-design operation than fixed-geometry turbines [14].

From the point of view of a Rankine cycle system analysis, using a mean-line flow model to predict the performance of a RIT can be regarded as a satisfactory compromise between model complexity and prediction accuracy. A selection of RIT mean-line models developed for Rankine cycle applications and documented in the open literature is summarized in Table 1. The methods differ on whether they can be applied for design optimization, performance analysis, or both. In addition, some of the methods considered RITs with movable nozzle blades, whereas most of them are limited to fixed-geometry turbines. Moreover, the mean-line models also differ with respect to which loss mechanisms are included. In particular, the losses associated with supersonic flow conditions in the nozzle or rotor blade rows, such as shock waves and intense mixing, are especially relevant in Rankine cycle turbines due to the potential combination of high-pressure ratio and low speed of sound of the working fluid. However, only a limited number of RIT mean-line models account for these complicated loss mechanisms and, to the knowledge of the authors, the only correlations available in the open literature are simple functions of the Mach number whose generality and accuracy could be questioned [15,16](p. 82).

As seen in Table 1, most of the RIT mean-line models documented in the open literature have been validated against experimental data or CFD simulations. In most cases, the model validation only considered data from one turbine operating at its design pressure ratio. Indeed, the model predictions from Refs. [17,23,24] showed a good agreement with the experimental data by Jones [27] at the design pressure ratio of 5.7. However, these authors did not

Table 1
Selection of RIT mean-line models applied for Rankine cycle analyses in the open literature.

Reference		Variable geometry	Design optimization/Performance analysis	Supersonic loss mechanisms	Validation
Hu et al. (2015)	[17]	No	Both	No	Exp.
Demierre et al. (2015)	[18]	No	Performance analysis	No	Exp.
Song et al. (2016)	[19]	No	Both	No	No
Da Lio et al. (2017)	[20]	No	Design optimization	Yes	No
Meroni et al. (2018)	[21]	No	Both	Yes	Exp./CFD
Alshammari et al. (2018)	[22]	No	Performance analysis	No	Exp.
Du et al. (2019)	[23]	Yes	Both	No	Exp
Liu and Gao (2019)	[24]	Yes	Both	No	Exp
Zhou et al. (2020)	[25]	No	Design optimization	No	CFD
Schuster et al. (2020)	[14]	Yes	Both	No	Exp.
Lee et al. (2021)	[26]	No	Performance analysis	No	CFD
Present work		Yes	Both	Yes	Exp.

present a comparison between experimental data and model predictions for the other 7 pressure ratios reported in Ref. [27]. Therefore, the accuracy of their models for off-design operation at other pressure ratios or for other turbine geometries is unknown.

The mean-line model presented by Meroni et al. [21] is arguably the most accurate for high-pressure ratio applications. The reason for this is twofold. First, the loss model that they adopted considers various loss mechanisms occurring in the nozzle and the rotor blade rows, including supersonic losses that are present when the flow velocity exceeds the speed of sound. Secondly, they calibrated some of the fitting constants of the loss model to minimize the deviation between the experimental data from six high pressure-ratio RITs and the corresponding model predictions. However, the performance prediction method proposed by Meroni et al. [21] requires an a priori numerical solution strategy to identify the choked nozzle mass flow rate, which is followed by an evaluation of whether the nozzle or the rotor chokes first as the pressure ratio increases. The remaining calculation procedure depends on the results from the initial analysis and it involves the solution of several systems of nonlinear equations. Although their method appears suitable for generating RIT performance maps, Meroni et al. [21] did not report the execution time required to compute each operating point and, therefore, it is not clear if their method is suitable for system-level analyses.

In fact, the robustness and computational cost of the methods for RIT design optimization and performance analysis documented in the open literature is overlooked in the majority of cases. As a notable exception, Hagen et al. [28] proposed an equation-oriented RIT design optimization method and applied it to a case study to show that the optimization problem is well-behaved and that the design optimization reliably converged to the global optimum in about 1 s.

Considering the limitations of the methods surveyed in Table 1, the aim of the present paper is to extend the work presented in Hagen et al. [28] and document the development of two robust and computationally efficient methods for the design optimization and performance analysis of RITs. The methods proposed in this work are based on a mean-line flow model and contain the following novel aspects: (1) the design optimization method uses a gradient-based optimization algorithm and relies on equality constraints to search for the optimal solution and close the model equations; (2) the performance prediction method uses a new numerical treatment of flow choking that is valid for subsonic and supersonic conditions and does not require an a priori solution strategy to identify whether the nozzle or the rotor are choked; and (3) each of the methods only requires the solution of a single mathematical problem, namely, a constrained optimization problem (design optimization) or a system of nonlinear equations (performance analysis).

The paper is organized as follows. The mean-line model and the mathematical formulation of the design optimization and performance analysis methods are described in Sec. 2. After that, the experimental data by Jones [27] and Spence et al. [29,30] are used to validate the mean-line flow model in Sec. 3. Finally, the capabilities of the proposed methods are demonstrated in Sec. 4 through a case study. First, a preliminary design for a RIT for an ORC power system is obtained using the design optimization method. Thereafter the RIT performance analysis method is applied to predict the performance maps of the designed turbine for various rotational speeds and nozzle throat areas. The conclusions drawn from this study are summarized in Sec. 5.

2. Methodology

The proposed methods for RIT design optimization and performance analysis consist of a problem formulation, a mean-line flow model and a gradient-based optimization algorithm. The illustration of the methods shown in Fig. 1 is valid for both design optimization and performance analysis.

The main difference between the two methods is the *problem formulation* step, where the RIT parameters are divided into three categories:

1. The *fixed parameters* are predefined by the user and do not change during the simulation. The RIT inlet state and outlet pressure are examples of fixed parameters in both the design optimization and performance analysis.
2. The *independent variables* are adjusted by the optimization algorithm to find the numerical values that optimize a certain objective function subject to constraints.
3. The *dependent variables* are computed using the independent variables and fixed parameters and they include the objective function and constraints.

A major part in the development of the problem formulation is grouping the RIT parameters into the three above-mentioned parameter categories and defining corresponding constraints and an objective function. A detailed presentation of methods for design optimization and performance analysis is presented in the following two subsections.

2.1. Design optimization

The problem formulation for RIT design optimization is shown in Table 2 (independent variables, constraints and objective function) and Table 3 (fixed and dependent RIT geometry variables). The optimization objective is to maximize the total-to-static isentropic efficiency. This objective function was selected because it is

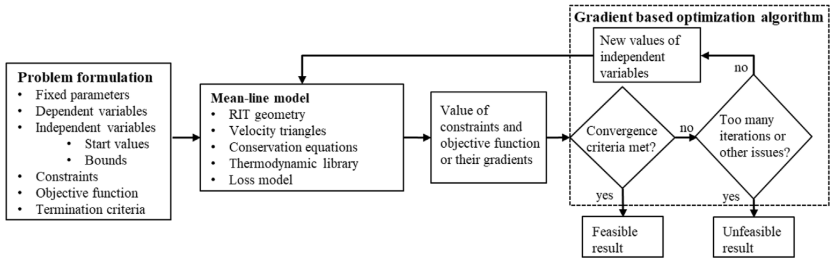

Fig. 1. Overview of the proposed methods for RIT-design optimization and performance analysis.

Table 2
Independent variables, constraints and objective function for design optimization.

Description	Symbol/formula	x_l	x_0	x_u
Nozzle outlet velocity	C_2/C_0	0.1	0.7	0.9
Nozzle outlet flow angle	α_3	40°	60°	80°
Rotor inlet meridional velocity	C_{4m}/C_0	0.02	0.20	0.40
Rotor outlet velocity	W_6/C_0	0.1	0.3	0.9
Rotor outlet flow angle	β_6	−70°	−68.5°	−20°
Specific speed	$\omega_s = \omega\dot{V}_{6,is}^{1/2}/\Delta h_{is}^{3/4}$	0.2	0.4	0.8
Velocity ratio	$\nu = U_4/c_0 = \omega r_4/C_0$	0.5	0.65	0.8
Rotor radius ratio (shroud/inlet)	r_{6s}/r_4	0.4	0.65	0.7
Rotor radius ratio (hub/shroud)	r_{6h}/r_{6s}	0.4	0.7	0.8
Blade height to radius ratio	b_3/r_4	0.04	0.1	0.34
Blade row outlet entropy[a,b]	s_{out}/s_1	1.0	1.0	s_{ref}/s_1
Constraints				
Consistent outlet pressure	$1.0 - p_6/p_{out} = 0$			
Consistent nozzle outlet enthalpy	$\frac{h_3 - h(p_3, s_{01}) - \sum_l \Delta h_{n,l}}{0.5C_3^2} = 0$			
Consistent rotor outlet enthalpy	$\frac{h_6 - h(p_6, s_4) - \Delta h_{int} - \sum_l \Delta h_{r,l}}{0.5W_6^2} = 0$			
Conservation of mass[c]	$1.0 - \rho WA\cos\beta/\dot{m} = 0$			
Minimum degree of reaction	$\frac{h_4 - h_6}{h_{01} - h_{06}} - 0.45 \geq 0$			
Objective function				
Maximize total-to-static efficiency	$\eta = \frac{h_{01} - h_{06}}{\Delta h_{is}}$			

[a] Two variables (nozzle and rotor).
[b] Reference entropy, s_{ref}, is the resulting outlet entropy when $\eta = 0.5$.
[c] Three constraints (nozzle outlet, rotor inlet and rotor outlet).

assumed that the kinetic energy leaving the rotor outlet is not recovered. The independent variables that govern the geometry, flow and thermodynamic parameters include both engineering decision variables, such as specific speed and velocity ratio, and parameters that are unknown a priori, such as the entropy distribution. The upper and lower bounds used to constrain the independent variables, as well as typical start values, are indicated in Table 2. The bounds on the independent RIT geometry and flow angle variables were set in accordance with the limits suggested in Refs. [16,17,31]. More specifically, this work applies the most conservative values from the above-mentioned references to ensure a feasible design. The normalized velocity variables cannot, due to conservation of energy, exceed the range between 0 and 1. However, a slightly smaller range of those variable were applied to limit the domain of the design space. In addition, the bounds for the specific speed and velocity are based on the results obtained by Da

Table 3
Value of fixed parameters and formulas of the dependent RIT geometry variables for design optimization.

Parameter	Symbol	Value	Source
Nozzle blade trailing edge thickness	t_3	$0.012c_n$	[16] (p. 256)
Rotor blade trailing edge thickness	t_6	$0.02r_4$	[16] (p. 240)
Rotor axial length	L_z	$1.5(r_{6s} - r_{6h})$	[16] (p. 240)
Blade tip clearances	ϵ_a, ϵ_r	0.4 mm	[33]
Disc clearance	ϵ_d/r_4	0.05	
Nozzle chord to pitch ratio	c_n/s_3	1.33	[16](p. 256)
Interspace distance	$r_3 - r_4$	$2b_3\cos\alpha_3$	[16](p. 256)
Number or rotor blades	Z_r	$12 + 0.03(\alpha_3 - 57°)^2$	[16,32], (p. 240)
Number of nozzle blades	Z_n	$Z_r + 3$	
Blade height, rotor inlet	b_4	b_3	

Lio et al. [20], who found that the maximum efficiency predicted by their model occurs when the specific speed is around 0.4 and the velocity ratio is in the range of 0.6–0.7.

When formulating the design problem, it was realized that some RIT geometry parameters are not suitable for optimization. For instance, the number of blades and the nozzle chord to pitch ratio always reached either their lower or upper bounds during initial design optimization tests. Consequently, fixing these parameters to the value of their active bound reduces the complexity of the mathematical problem without affecting the outcome of the optimization. In addition, other parameters, such as blade edge thicknesses and rotor tip clearances, are constrained due to factors not included in the model (e.g., manufacturing requirements or stress considerations).

Consequently, all these parameters are either fixed or calculated from the set of independent variables during the optimization. The value of the fixed parameters and formulas for the dependent RIT geometry variables are shown in Table 3, and most of these were suggested default values from Aungier [16]. The empirical formula used to compute the number of rotor blades was developed by Rohlik [32] and recommended by Aungier [16]. Several scientific works report or assume rotor blade tip clearances, ε_a, ε_r, in the range 0.21–0.50 mm [14,20,27,29,31]. However, extensive development of small gas turbines have shown that it is difficult to maintain clearances less than about 0.4 mm [33,34](p. 354). For this reason, a conservative value of 0.4 mm is assumed for the rotor tip clearances. Finally, the disc clearance and the number or nozzle blades were assigned arbitrary, yet realistic, values. The influence of these two variables on the design efficiency is negligible in comparison to that of other parameters, as demonstrated in the sensitivity analysis shown in Fig. 9.

The design optimization starts by computing the isentropic enthalpy change, $\Delta h_{is} = h_{01} - h(p_{out}, s_{01})$, using the prescribed inlet state and outlet pressure. This enables the calculation of the spouting velocity, $C_0 = \sqrt{2\Delta h_{is}}$. Thereafter the rotational speed and the rotor inlet radius can be computed from the independent specific speed and velocity ratio variables. After that, the remaining geometry parameters can be calculated using the independent geometry variables and the fixed- and dependent geometry parameters. The geometry parameters involved in the mean-line model are illustrated in Fig. 2.

Once the RIT geometry is described, the dependent variables required to evaluate the objective function and constraints are computed by means of the mean-line model. This model assumes that the flow is uniform along the blade span and evaluates the velocity triangles and thermophysical properties at the inlet, throat, and outlet of the nozzle and rotor blade rows, see Fig. 2. As usually done in the context of mean-line modelling [14,21], the presence of boundary layers near the surfaces of the blades, hub, and shroud was neglected. Consequently, the mass flow rate constraints of Table 2 were evaluated using the geometrical cross-section area given by Eqs. (1) and (2).

$$A_i = 2\pi r_i b_i, \quad i = 3, 4 \tag{1}$$

$$A_6 = \pi\left(r_{6s}^2 - r_{6h}^2\right) \tag{2}$$

The mean-line model starts by computing the nozzle outlet enthalpy by conservation of energy, Eq. (3).

$$h_3 = h_{01} - \frac{1}{2}C_3^2 \tag{3}$$

The enthalpy and velocity at the inlet of the rotor are calculated by conservation of angular momentum, Eq. (4), and energy, Eq. (5), through the interspace.

$$C_{4t} = \frac{r_3}{r_4}C_{3t} \tag{4}$$

$$h_4 = h_{01} - \frac{1}{2}\left(C_{4m}^2 + C_{4t}^2\right) = h_{01} - \frac{1}{2}C_4^2 \tag{5}$$

The rotor outlet enthalpy is then calculated by conservation of rothalpy through the rotor, Eq. (6).

$$h_6 = h_4 + \frac{1}{2}\left(W_4^2 - U_4^2\right) - \frac{1}{2}\left(W_6^2 - U_6^2\right) \tag{6}$$

A simplification is performed regarding the computation of the thermodynamic state and velocity at the throat of the blade rows (state points 2 and 5). Namely, the thermodynamic state at the throat is assumed to be equal to the blade row outlet state and the relative velocity at the throat is computed according to Eq. (7).

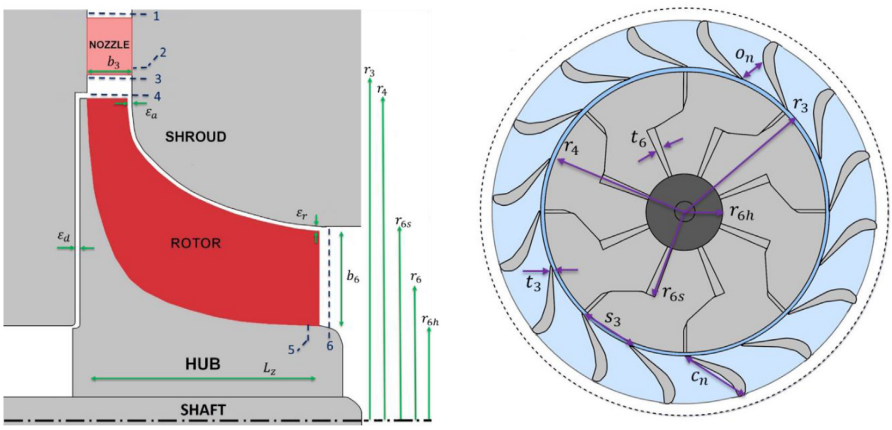

a) View at the meridional plane **b) View in the axial direction**

Fig. 2. Illustration of the radial inflow turbine and the geometry parameters involved in the mean-line model.

$$W_{th} = \begin{cases} W_{out}, \ Ma_{out} < 1 \\ a(h_{out}, s_{out}), \ Ma_{out} \geq 1 \end{cases} \tag{7}$$

The thermodynamic states except the inlet state are defined by enthalpy and entropy. The remaining relevant thermophysical properties in these states are calculated by enthalpy-entropy function calls, Eq. (8).

$$\rho_i, \ T_i, \ p_i, \ \mu_i, a_i = f(h_i, s_i), \ i = \{2, 6\} \tag{8}$$

The mean-line model is compatible with any thermodynamic library that supports enthalpy-entropy function calls. In this work, the thermodynamic calculations were performed using REFPROP v10.0 [35].

Furthermore, the losses due to irreversibilities within the turbine are estimated using an empirical loss model. The loss model adopted in this work, Table 4, was proposed by Meroni et al. [21] and considers loss mechanisms in the nozzle, interspace and the rotor, including the losses related to supersonic flow conditions.

The coefficients K_{in}, K_{p1}, K_{p2} and K_{p3} were introduced by Meroni et al. [21] to calibrate the loss model. More specifically, they adjusted the calibration coefficients by means of a genetic algorithm with the aim to minimize the average root mean square (RMS) deviation between experimental data from six high-pressure ratio RITs and corresponding model predictions. The model validation presented in this work consider both the original- and the calibrated loss model defined in Table 5. A more complete account of the equations and parameters involved in the loss model is presented in Appendix A.

Table 5
Values of the calibration coefficients in the loss models [21].

	Calibrated loss model	Original loss model
K_{p1}	1.3881	1.0
K_{p2}	0.6370	1.0
K_{p3}	0.1042	1.0
K_{in}	0.8952	1.0

The proposed design strategy takes advantage of equality constraints to ensure that the mathematical model is consistent. For example, two equality constraints are imposed to ensure that the calculated enthalpy distribution is consistent with the predicted enthalpy losses and three equality constraints are imposed to ensure that the mass flow rate is conserved and its value is equal to the design specification. In addition, other equality- or inequality constraints may be readily imposed to ensure that the outcome of

Table 4
Summary of the loss model from Meroni et al. [21] that is applied in this work.

Mechanism	Correlation	
Nozzle passage[a]	$\Delta h_{n,p} = K_{p1} \frac{0.05}{Re_2^{0.2}} \left[\frac{3 \tan \alpha_2}{s_3/c_n} + \frac{s_3 \cos \alpha_2}{b_3} \right] \frac{1}{2} C_2^2$	(9)
Nozzle trailing edge[a]	$\Delta h_{n,te} = \left(\frac{t_3}{s_3 \cos \alpha_2} \right)^2 \frac{1}{2} C_2^2 Y_2$	(10)
Nozzle supersonic	$\Delta h_{n,su} = \left(\frac{M_3 - M_2}{M_3} \right)^2 \frac{1}{2} C_3^2 Y_3$	(11)
Interspace	$\Delta h_{int} = C_f \frac{L}{D} \frac{1}{2} \left(\frac{C_3 + C_4}{2} \right)^2$	(12)
Rotor incidence	$\Delta h_{r,i} = K_{in} \frac{1}{2} W_4^2 \sin^2 (\beta_4 - \beta_{4,opt})$	(13)
Rotor passage[a]	$\Delta h_{r,p} = 0.11 \left\{ K_{p2} \frac{L_H}{D_H} + 0.68 K_{p3} \left[1 - \left(\frac{r_6}{r_4} \right)^2 \right] \frac{\cos \beta_{6b}}{b_6/c_r} \right\} \frac{1}{2} \left(W_4^2 + W_5^2 \right)$	(14)
Rotor trailing edge[a]	$\Delta h_{r,te} = \left(\frac{Z_r t_6}{\pi (r_{6s} + r_{6h}) \cos \beta_5} \right)^2 \frac{1}{2} W_5^2 Y_5$	(15)
Rotor clearance	$\Delta h_{r,cl} = \frac{U_4^3 Z_r}{8\pi} \left\{ 0.4 \varepsilon_a K_a + 0.75 \varepsilon_r K_r - 0.3 \sqrt{\varepsilon_a \varepsilon_r K_a K_r} \right\}$	(16)
Rotor disc friction[a]	$\Delta h_{r,df} = 0.25 K_f \frac{\rho_4 + \rho_5}{2} \frac{U_4^3 r_4^2}{\dot{m}}$	(17)
Rotor supersonic	$\Delta h_{r,su} = \left(\frac{M_6 - M_5}{M_6} \right)^2 \frac{1}{2} W_6^2 Y_6$	(18)

[a] The point indices corresponding to the blade row throat states (points 2 or 5) do not match with the indices stated in Ref. [21] who, instead, adopted the blade row outlet states (points 3 or 6). However, a personal communication with Andrea Meroni confirmed that Ref. [21] actually used the throat velocity (and not the row outlet velocity) to compute the passage- and trailing edge losses because they believed it to be the most consistent way to express the losses.

the optimization satisfies additional design requirements such as a given degree of reaction or a maximum rotational speed.

The gradient-based algorithm applied in this work was NLPQL [36], which is a sequential quadratic programming (SQP) method that can be applied for solving both constrained optimization problems and systems of nonlinear equations. Gradients are calculated using a second order central difference approximation for numerical differentiation. The step length used to perturb the independent variables during the gradient estimation is shown in Table 6 and is approximately three orders of magnitude smaller than the value of the independent variables. The Kerush Kuhn Tucker (KKT) optimal criterion is set to 1.0E-7 and the maximum number of iterations is set to 80. This means that NLPQL returns an unfeasible result if the KKT optimal criterion is not met within 80 iterations or other issues occur, see Ref. [36] for details.

2.2. Performance analysis

The independent variables and constraints for the RIT performance analysis are summarized in Table 7. The independent variables include the unknown velocities and entropy distribution, and several equality constraints are imposed to ensure internal consistency. The number of independent variables equals the number of equality constraints, meaning that there are zero degrees of freedom for optimization and the mathematical problem is a system of nonlinear equations.

The calculation procedure for performance analysis is very similar to that for design optimization. However, in the performance analysis method, the RIT geometry and rotational speed are defined as fixed parameters. In addition, instead of being independent variables, the blade row outlet flow angles are calculated using the throat area and the equation of conservation of mass as indicated in Fig. 3. The only inner iteration in the mean-line model activates when outlet velocity of a blade row is supersonic. In such case, the throat velocity is first guessed as the speed of sound at the outlet. Thereafter multiple successive substitutions are performed until the throat Mach number converges to 1.0. A relatively strict convergency criterion ($\varepsilon = 10^{-10}$) is set to ensure accurate numerical gradient estimations. In the case of subsonic outlet velocity, no iteration is required to compute the thermodynamic state at the throat. Instead, the thermodynamic state at the throat and outlet are assumed to be equal. In this case, the formula for computing the outlet flow angle becomes equivalent to the well-known cosine rule since the density and velocity factors cancel each other out.

In contrast with the design optimization formulation, the performance analysis also uses the entropy at the throat of each blade row as independent variables. The reason for this additional complexity is to ensure physically consistent results in the case when the flow in either of the blade rows is choked. A reliable RIT performance analysis should predict a mass flow rate that increases with pressure ratio (by reducing the outlet pressure) until it converges to a limiting value that corresponds to the case when the flow velocity in either of the blade rows reaches the speed of sound. At this point the blade row is choked and a further increased pressure ratio will not affect the mass flow rate, or the thermodynamic states and velocity triangles upstream of the throat [37] (p. 264–265) The additional entropy variables and corresponding constraints ensure that, once a blade row is choked, a further increase in pressure ratio will not affect the thermodynamic state at the throat or any points upstream of the throat. Instead the additional entropy production due to supersonic losses is assigned at the outlet of the blade row. Thus, the mass flow rate, which depends on the density at the throat, will remain constant beyond the choking point.

Table 6
Step lengths for numerical differentiation used in the model validation and the case study.

Independent variable	Step length for numerical differentiation
$C_3/\ c_0$, $C_{4m}/\ c_0$, $W_6/\ c_0$	10^{-3}
ω_s	
r, $r_{6s}/\ r_4$, $r_{6h}/\ r_{6s}$	
$b_3/\ r_4$	10^{-4}
α_3, β_6	10^{-3} rad
Entropy variables	$(1 - s_{ref}/s_{01})\cdot 10^{-3}$

2.3. Model implementation and compilation

The mean-line model, problem formulations and interfaces with the Fortran source code of the optimization algorithm and the thermodynamic library are written in the C programming language. The executable files for running the design optimization and performance analysis were built using the GNU [38] compilers *gcc* and *gfortran*.

2.4. Discussion of the problem formulations

Developing a simple and effective problem formulation is a challenging task that requires creativity and a solid understanding of the underlying mathematical models and the numerical algorithms used to solve the problem. We believe that the proposed design optimization and performance analysis problem formulations have some advantages that are worth highlighting:

1. The independent variables, constraints and the objective function are written in non-dimensional form. For instance, the velocity variables are scaled by the spouting velocity and the angular variables are converted to radians. A non-dimensional problem formulation is not only advantageous from a numerical point of view, but it is also advantageous from a practical standpoint because the initial guess and bounds of the independent variables can be defined using physical principles and general design guidelines instead of being tailored to each specific application.
2. The use of a predefined outlet pressure in the performance analysis ensures a unique solution of the problem. In the case of predefined mass flow rate (as in Schuster et al. [14] and Meroni et al. [21]), care must be taken to specify a problem with a unique and feasible solution. This is because, once the flow is choked, there is an infinite number of values for the outlet pressure that yield the same mass flow rate, see Fig. 11. Schuster et al. avoided numerical problems by considering subsonic turbines only, while the approach in Ref. [21] involved use of a numerical method to detect the choked mass flow rate. In addition, in the case of a choked turbine, Meroni et al. [21] provided a predefined outlet pressure together with the mass flow rate to ensure a unique solution.
3. The use of blade row outlet velocities as independent variables avoids the need for an a priori numerical solution strategy for identifying whether any blade rows are choked as in Meroni et al. [21]. Instead, the choked flow calculation activates every time the blade row outlet flow velocity is supersonic. However, whether the blade row actually chokes depends solely on the magnitude of the outlet Mach number at the last iteration before a feasible solution is found.
4. In contrast with other published methods, see Table 1, the equation-oriented formulation of the design optimization avoids the use of inner iterations. Instead, the model equations

Table 7
Independent variables and constraints for performance analysis.

Description	Symbol
Nozzle outlet velocity	C_3/c_0
Rotor inlet meridional velocity	C_{4m}/c_0
Rotor outlet velocity	W_6/c_0
Blade row throat entropy[a]	s_{th}/s_{01}
Blade row outlet entropy[a]	s_{out}/s_{01}
Constraints	
Consistent outlet pressure	$1.0 - p_6/p_{out} = 0$
Consistent nozzle throat enthalpy	$\frac{h_2 - h(p_2, s_{01}) - \sum_{l \neq su} \Delta h_{n,l}}{0.5C_3^2} = 0$
Consistent nozzle outlet enthalpy	$\frac{h_3 - h(p_3, s_{01}) - \sum_{l} \Delta h_{n,l}}{0.5C_3^2} = 0$
Consistent rotor throat enthalpy	$\frac{h_5 - h(p_5, s_4) - \Delta h_{int} - \sum_{l \neq su} \Delta h_{r,l}}{0.5W_6^2} = 0$
Consistent rotor outlet enthalpy	$\frac{h_6 - h(p_6, s_4) - \Delta h_{int} - \sum_{l} \Delta h_{r,l}}{0.5W_6^2} = 0$
Conservation of mass[b]	$1.0 - \rho W A \cos\beta / \rho_3 C_3 A_3 \cos\alpha_3 = 0$

[a] Two variables (nozzle and rotor).
[b] Two constraints (Rotor inlet and rotor outlet).

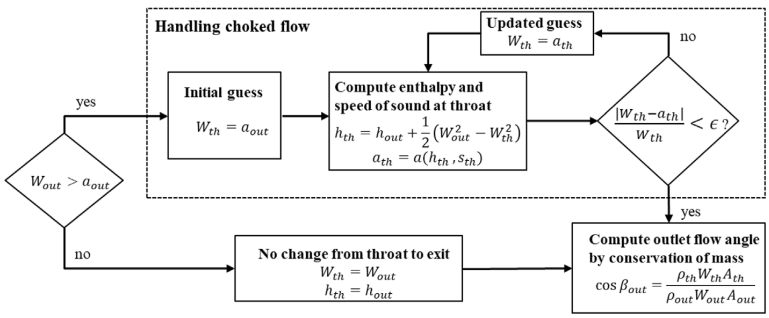

Fig. 3. Method used to compute the velocity and thermodynamic state at the throat and the outlet flow angle of a blade row in the performance analysis method.

are closed by means of equality constraints that are processed at once by the gradient-based optimization algorithm. As a result, the model equations do not have to be converged at each optimization iteration and the computational cost of the problem is reduced.

5. The optimization algorithm used in the performance analysis method could be replaced by a nonlinear equation solver because the number of equality constraints equals the number of independent variables. However, using the same algorithm for design optimization and performance analysis yields a smooth transition between the two methods. In addition, the optimization algorithm gives the additional flexibility of formulating the performance analysis as an optimization problem. For instance, little additional effort is required to modify the proposed performance analysis method to automatically find the rotational speed that maximizes the off-design efficiency.

3. Model validation

Several sets of experimental RIT data have been published in the open literature, but only a few of them are of sufficient quality to be applied for model validation [39]. A high-quality set of experimental data should contain measurements taken at different pressure ratios and rotational speeds. In addition, the RIT geometry should be documented such that it can be replicated within the

Table 8
RIT operating conditions and geometry for model validation.

			Spence et al. [29,30]	Jones [27]
Operating conditions	Fluid		Air	Air
	p_{01}	[bar]	1.3–3.6	4.136
	T_{01}	[°C]	126.85	204.45
	p_{out}	[bar]	1.01325	0.44–1.36
Nozzle	r_3	[mm]	55.5	63.5
	b_3	[mm]	10.2	6.0
	Z_n	[–]	16	19
	A_2	[mm^2]	653–1387[b]	491
	t_3	[mm]	1.0	0.51
	c_n	[mm]	37.4	22.9
Rotor	ω	[RPM]	30000–60000[a]	56000–83000
	r_4	[mm]	49.5	58.2
	r_{6s}	[mm]	39.5	36.8
	r_{6h}	[mm]	15.0	15.2
	b_4	[mm]	10.2	6.35
	Z_r	[–]	11	16
	t_6	[mm]	1.60	0.76
	A_5	[mm^2]	2317	1910
	L_z	[mm]	41.0	38.9
	c_r	[mm]	47.8[c]	45.7
	ε_a	[mm]	0.40	0.40
	ε_r	[mm]	0.40	0.21
	ε_d	[mm]	0.25	0.33

[a] Corrected speed, $\omega_{corr} = \omega\sqrt{T_{01}/T_{ref}}$, $T_{ref} = 288$ K.
[b] Computed as $A_2 = Z_n b_3 o_n$.
[c] Computed by Eq. (A.6) using $\beta_{6b} = -50.1°$.

mean-line model. In this work, the proposed mean-line model was validated against two comprehensive data sets whose geometric parameters and operating conditions are listed in Table 8. The reader is referred to Refs. [12,17] for an overview of other experimental data sets that could be used for RIT mean-line model validation.

3.1. Experimental data

The first data set is by Spence et al. [29,30], who performed experiments on 10 different turbine configurations. All cases consisted of the same rotor surrounded by a ring of nozzle blades operating at different setting angles. Consequently, the geometric characteristics of the turbines only differ in nozzle throat opening [29,30]. Hence, this data set is ideal for validating a variable-geometry RIT model. To the best of our knowledge, the experimental data of Spence et al. has rarely been used for model validation. The only study found in which data from Ref. [29] were used for model validation was Ref. [22]. However, only data for the turbine with the smallest nozzle throat opening was considered in that study. The experimental data from Spence et al. covers efficiency and corrected mass flow rate measured at different pressure ratios and rotational speeds. To facilitate comparison of predicted mass flow rates with experimental data, the corrected mass flow rate was calculated by Eq. (19). The reference pressure and temperature were set to standard atmospheric conditions in accordance with Ref. [29].

$$\dot{m}_{corr} = \dot{m}\sqrt{T_{01}/T_{ref}}\cdot p_{ref}/p_{01} \tag{19}$$

The second data set is by Jones [27], who performed measurements at 8 different pressure ratios, ranging from 3 to 9. Hence, this data set is ideal for validating a RIT mean-line models for high-pressure ratio applications, such as Rankine cycle power systems. Data from Ref. [27] has been widely used for model validation after it was rediscovered by Sauret [39], who also published more geometry information regarding Jones' turbine. However, to the best of our knowledge, only the data at the design pressure ratio of 5.7 have previously been used for model validation. The turbine analyzed by Jones had an exhaust diffuser to recover some of the kinetic energy leaving the rotor. In order to account for this, we modeled the diffuser with a fixed recovery coefficient, $c_d = 0.55$, (value given in Ref. [27]). This means that the computed rotor outlet pressure had to be replaced by the diffuser outlet pressure in the equality constraint used to ensure a consistent outlet pressure, see Table 7.

3.2. Results

A qualitative comparison of experimental data from three of the turbines from Spence et al. [29,30] and the corresponding mean-line model predictions with the original and calibrated loss models, as defined in Table 5, is shown in Fig. 4. As seen in Fig. 4(b,d,f), the mean-line model slightly overpredicts the mass flow rate in both cases. Part of this overprediction could be attributed to the neglection of boundary layer effects. Indeed, an approximate flat-plate boundary layer analysis indicated that the combined displacement thickness in the nozzles might be about 2–3% of the throat opening. The loss model also affects the predicted mass flow rate illustrated by the larger mass flow rates predicted by the calibrated loss model. In any case, the mean-line model is able to predict that the mass flow rate increases with increasing pressure ratio, decreasing rotational speed, and increasing nozzle throat opening, which agrees with the experimental data. Concerning the efficiency, Fig. 4(a,c,e), the mean-line model generally overestimates its value except for some pressure ratios at the lowest rotational speed. Despite this, the model captures the main trends; the rotational speed has a strong effect on the efficiency and lower rotational speeds yield better efficiency at lower pressure ratios and vice versa. In addition, the pressure ratio in which the peak efficiency occurs is predicted reasonably well for different rotational speeds and nozzle throat openings. Moreover, it can be observed that the predictions obtained using the calibrated loss model deviate more from the experimental data in Fig. 4 than those obtained using the original loss model.

A comparison of experimental efficiency data from Jones [27] and corresponding model predictions are shown in Fig. 5. Each plot (a,b,c,d) represents data at a single pressure ratio and the x-axis corresponds different rotational speeds expressed as the velocity ratio. The calibrated loss model predicts a higher efficiency than the original loss model in all cases. In addition, the original loss model agrees better with the experimental data at the lower pressure ratios, while the calibrated loss model agrees better with the experimental data at the larger pressure ratios. Moreover, both loss models predict the velocity ratio in which the peak efficiency occurs to be around 0.7. This agrees quite well with the experimental data at pressure ratio of 4.0, see Fig. 5(a). However, at larger pressure ratios, the experimental data indicates that the maximum efficiency is achieved at a slightly higher velocity ratio (about 0.75).

Figs. 4 and 5 only represent a fraction of the experimental data from the 10 turbine configurations in Spence et al. [29,30] and the 8 pressure ratios in Jones [27]. Nonetheless, the trends observed in these figures also hold for the remaining test conditions and they were not plotted for the sake of brevity. Instead, the Root Mean Square (RMS) deviation between experimental data and model prediction in terms of mass flow rate and isentropic efficiency was computed for all test conditions and summarized in Table 9. The results indicate that the original loss model, on average, agrees better with the experimental data of Spence et al. [29,30] than the calibrated loss model does. However, this situation is reversed for the experimental data by Jones [27]. In this case, the calibrated loss model yields a lower RMS efficiency-deviation and predicts the design point mass flow rate with a deviation below one percent. The calibrated loss model was trained using data from high-pressure ratio RITs and it is not surprising that it is more accurate than the original loss model for such cases.

4. Case study

In this section the proposed design optimization and performance analysis methods were applied to design and analyze a RIT for the transcritical ORC considered in Ref. [40], see Fig. 7. As the design pressure ratio for this case study is relatively low (4.87), the calculations were carried out using the more conservative *original* loss model.

4.1. Design optimization

The design optimization was performed using the problem formulation from Tables 2 and 3 and the operation conditions indicated in Fig. 6. The main results obtained from the design optimization are summarized in Table 10. The values of the specific speed and velocity ratio agree well with the values reported by Da Lio et al. [20]. The design optimization performed by Hu et al. [17] obtained almost the same specific speed (0.42) as in this work, but a slightly larger velocity ratio (0.7). Moreover, two independent RIT geometry variables had an active variable bound. Namely, the ratio r_{6s}/r_4 reached its upper bound of 0.7 and the ratio b_3/r_4 reached its

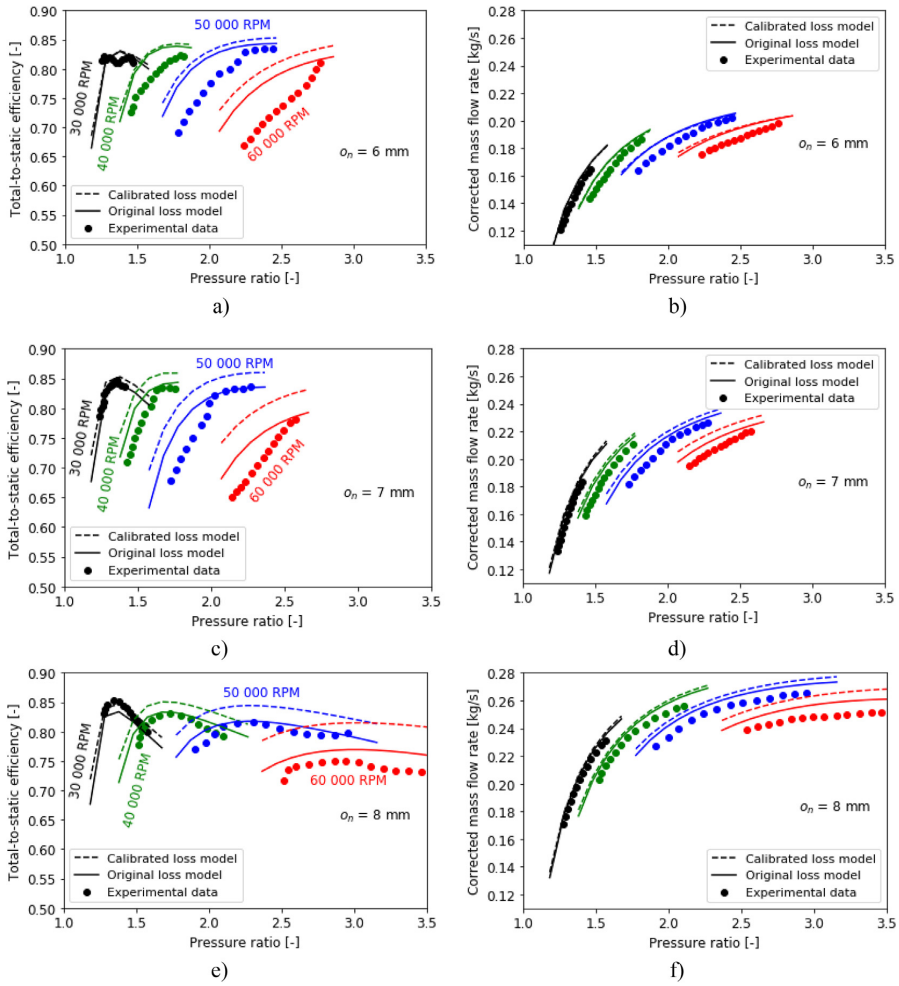

Fig. 4. Qualitative comparison between experimental data by Spence et al. [29,30] and corresponding model predictions: Total-to-static efficiency (a, c, e) and corrected mass flow rate (b, d, f).

lower bound of 0.04. These bounds were suggested by Aungier [16](p. 243) and Hu et al. [17], respectively. In addition, the inequality constraint for minimum degree of reaction, whose lower limit was proposed by Aungier [16](p. 243), was active.

The *T-s* diagrams of the ORC process and the expansion within the RIT are illustrated in Fig. 7. It can be observed that the working fluid enters the turbine at supercritical conditions and leaves as superheated vapor. In addition, the close-up view of the expansion process indicates that most of the entropy generation occurs in the rotor row and that the kinetic energy leaving the turbine is small. These results are confirmed by the loss distribution, rotor geometry, and velocity triangles illustrated in Fig. 8. More specifically, the sum of the rotor clearance, passage, and trailing edge losses leads to a reduction in the total-to-static efficiency of about 11% points, which represents 70 % of the losses. By contrast, the kinetic energy loss only penalizes the turbine total-to-static efficiency by 2.6% points, which is explained by the large flow area ($A_6/A_4 = 3.5$) and small flow angle ($\alpha_6 = 2.8°$) at the exit of the rotor. The rest of the entropy generation can be attributed to the rotor disc friction loss, the interspace loss and the losses in the nozzle ring. Notably, the nozzle operates at supersonic conditions, $Ma_3 = 1.22$, which leads to a supersonic loss that penalizes the total-to-static isentropic efficiency about one percentage point.

A one-at-a-time sensitivity analysis was performed to illustrate the sensitivity of the design efficiency to some of the assumptions used in the design problem formulation. In particular, the lower limit of the degree of reaction and values of selected parameters from Table 3 were modified up and down by 20 % of their nominal value, and a design optimization was carried out for each parameter configuration. The results from the sensitivity analysis, see Fig. 9, show that a higher design efficiency can be obtained by allowing a lower degree of reaction and that the sensitivity of the design efficiency to the number of nozzle blades and the disc clearance are negligible in comparison with the sensitivity to the degree of reaction.

One drawback of gradient-based optimization algorithms is that they may converge to a local optima close to the starting point used for the optimization. In addition, the convergence to a feasible

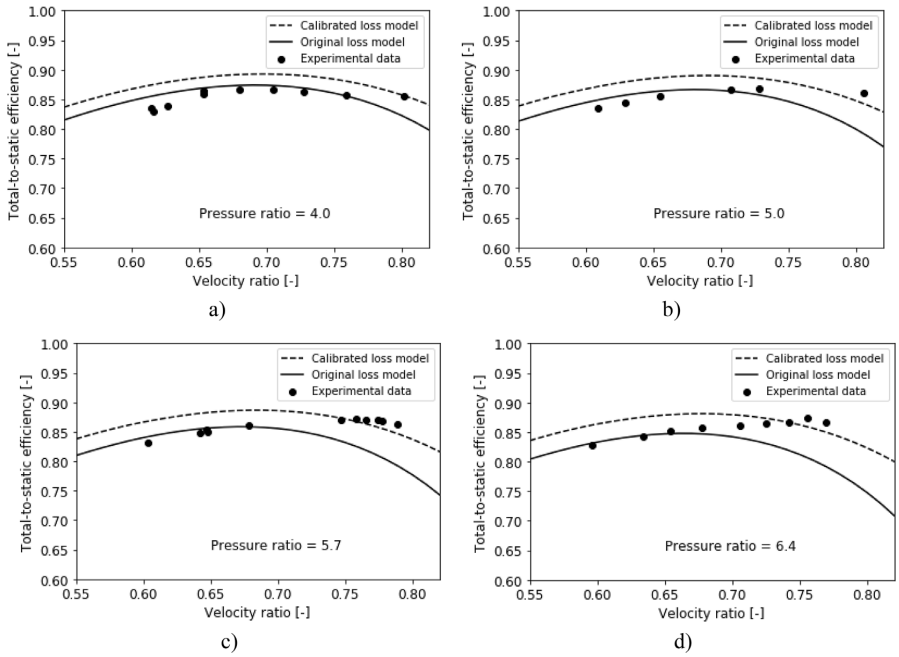

Fig. 5. Qualitative comparison between experimental data by Jones [27] and corresponding model predictions.

Table 9
Average RMS deviation between experimental data and corresponding model predictions.

Experimental data	Jones [27]		Spence et al. [29,30]	
Parameter	η_{ts}	$\dot{m}^a$	η_{ts}	$\dot{m}$
Original loss model	3.4 %-points	2.1%	4.0 %-points	3.2%
Calibrated loss model	2.5 %-points	0.9%	5.3 %-points	3.8%

[a] Experimental data available at design point (pressure ratio of 5.78, $\nu = 0.70$) only.

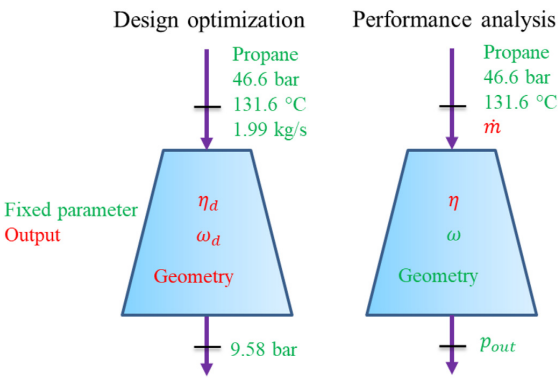

Fig. 6. Fixed operating conditions for the case study and indication of the main output parameters for the design optimization and performance analysis.

solution is only guaranteed if the objective- and the constraint functions are twice continuously differentiable. In this work, the robustness of the proposed design optimization method was assessed by carrying out 100 design optimizations starting from random initial values for the independent variables. As seen in Fig. 10(a), essentially all optimizations converged to the same solution as the optimal value of the independent variables differed by less than ± 0.06 %. The consistency in the optimization results is a strong indication that the proposed design optimization method reliably converges to the global optimum solution despite the non-smooth transition between subsonic and supersonic flow velocities in Eq. (7). The average execution time on a personal computer with an Intel Core i7-8650U CPU of 2.11 GHz was 0.97s and 76 % of the optimizations spent less than 1 s to converge, see Fig. 10(b).

4.2. Performance analysis

The off-design performance analyses were carried out using the problem formulation from Table 7 and the operating conditions indicated in Fig. 6. To this aim, the RIT geometry obtained during the design optimization, see Table 11, was provided as fixed parameters and the influence of the rotational speed, pressure ratio, and nozzle throat area on the isentropic efficiency and mass flow rate was analyzed. More specifically, the rotational speed was varied between 70 % and 110 % of its design value, the outlet pressure was varied such that the pressure ratio varied between 1.8 and 8.0, and the nozzle throat area was varied between 60 % and 120 % of its design value.

The mass flow rates predicted by the mean-line model are shown in Fig. 11. Each of the plots (a,b,c,d) corresponds to a certain nozzle throat area, whereas each colored line represents a certain rotational speed. The design condition is indicated with an “x” in the figures. It can be observed that the mass flow rate increases with the pressure ratio until choking occurs and then remains constant. Moreover, the model predicts that the pressure ratio in

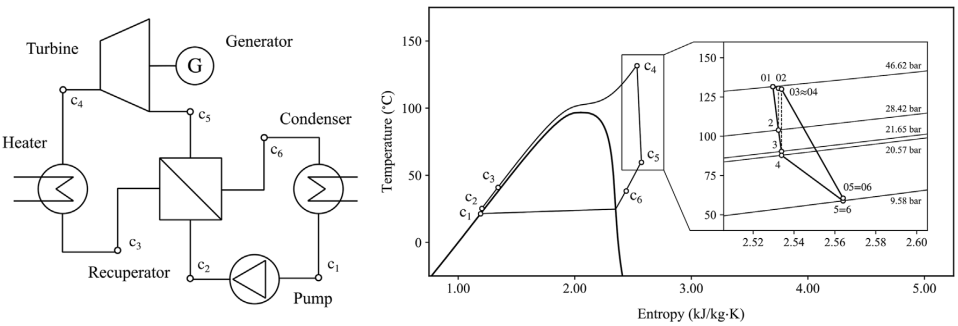

Fig. 7. Process flow diagram of the ORC considered in Ref. [40] and ***T*-*s*** diagrams of the ORC process and the expansion within the RIT obtained from the design optimization.

Table 10
Main results from the design optimization.

Parameter	Symbol	Value
Specific speed	ω_s	0.41
Velocity ratio	ν	0.65
Degree of reaction	R	0.45
Nozzle outlet flow angle	α_3	69.3°
Rotor outlet flow angle	α_6	2.8°
Rotor area ratio	A_6/A_4	3.5
Design rotational speed	ω_d	57 579 RPM
Design efficiency	η_d	0.841
Shaft power	$\dot{W}$	140 kW

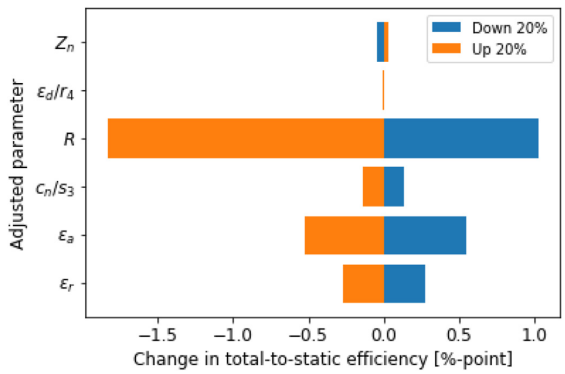

Fig. 9. Sensitivity of design efficiency to input parameters.

which choking occurs is higher for higher rotational speeds. In most cases, the value of the choked mass flow rate is unaffected when the rotational speed changes. This is an indication that the flow in the nozzle is the first to choke, because in case the flow in the rotor was the first to choke, an increase in rotational speed would lead to a reduction in the mass flow rate [12] (p. 24). However, for the case when $A_2 = 1.2A_{2d}$ and $\omega = 1.1\omega_d$ the mean-line model predicts that only the rotor is choked, see Fig. 12. Indeed, as seen in Fig. 11(d), the red line is lying slightly below the other curves.

The results depicted in Fig. 11 also indicate that the nozzle throat area strongly affects the mass flow rate. Indeed, the results shown in Fig. 13 demonstrate that the mass flow rate is roughly proportional to the nozzle throat area. This trend agrees well with the experimental data of Spence et al. [30], which also suggests a relationship between mass flow rate and nozzle throat area that is roughly proportional.

The total-to-static efficiencies predicted by the mean-line model are shown in Fig. 14. These results indicate that the rotational speed has a strong influence on the efficiency and that, for each rotational speed, there is a pressure ratio that maximizes the efficiency. In addition, the results illustrated in Fig. 14(c) suggest that using a rotational speed lower than the design one is advantageous when the pressure ratio is lower than the design value.

The nozzle throat area also affects the total-to-static efficiency.

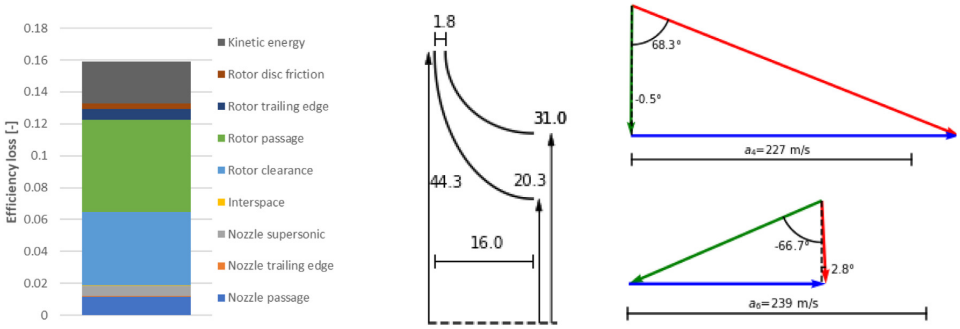

Fig. 8. Loss distribution, rotor geometry (values in mm) and rotor inlet and rotor outlet velocity triangles from the design optimization.

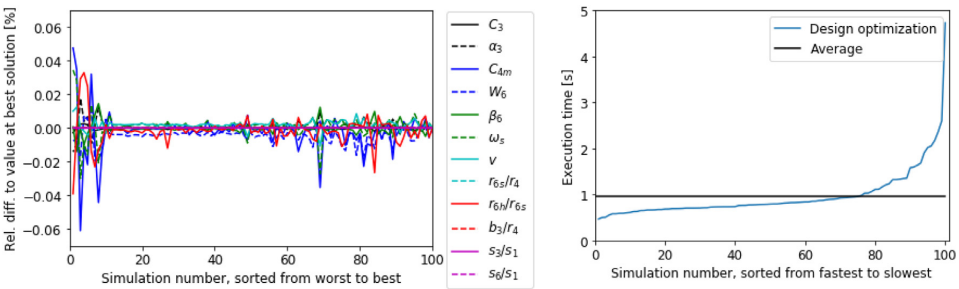

Fig. 10. Results and execution time of 100 design optimizations with random start values of the independent variables.

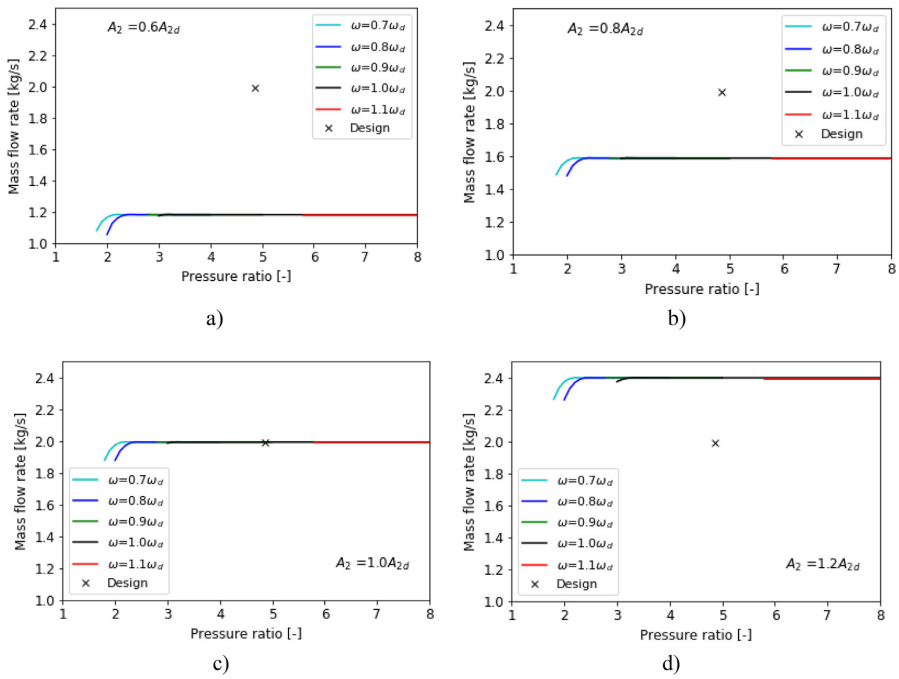

Fig. 11. Predicted mass flow rate vs. pressure ratio for different rotational speeds and nozzle throat areas.

For instance, when comparing Fig. 14(a) and (d) it is clear that, for small nozzle throat areas, the highest efficiencies occur at larger pressure ratios, while, for large nozzle throat areas, the highest efficiencies occur at the lowest pressure ratios. This trend agrees well with the experimental data concerning variable-geometry RIT measured by Spence et al. [30]. The efficiency penalization at high pressure ratios and large nozzle throat opening can be attributed to increased kinetic energy loss due to larger rotor outlet velocities [30]. Indeed, a comparison between Fig. 15(a) and (b) shows that the reduction in the total-to-static efficiency due to the kinetic energy loss for the case $A_2 = 1.2A_{2d}$ is up to five percentage points higher than that of the case $A_2 = A_{2d}$. This is not surprising because the flowrate and flow velocity leaving the rotor are larger when the nozzle throat area is increased.

The efficiency trends depicted in Fig. 14 also provide information about the pressure ratio in which the rotor chokes. In the cases when $A_2 = 0.6A_{2d}$ and $A_2 = 0.8A_{2d}$ the flow in the nozzle is the first to choke and the rotor remains unchoked. However, when $A_2 = A_{2d}$ and $A_2 = 1.2A_{2d}$ the rotor chokes at a pressure ratio about 7 and 6, respectively. The transition between unchoked and choked rotor can be observed as a kink point in the efficiency vs. pressure ratio curves in Fig. 14(c and d). After this point, all the losses upstream the rotor throat remain constant in terms of enthalpy change, see Table 4, and any additional losses are due to the rotor supersonic loss and the kinetic energy at the exit of the rotor. In fact, as illustrated by the loss distribution in Fig. 15, the predicted supersonic loss is almost negligible in comparison with the other losses and the decrease in efficiency as the pressure ratio increases can be

Table 11
RIT geometry obtained from the design optimization.

Nozzle	r_3	[mm]	45.5
	b_3	[mm]	1.77
	Z_n	[−]	20
	A_{2d}	[mm^2]	167[a]
	t_3	[mm]	0.23
	c_n	[mm]	19.4
Rotor	r_4	[mm]	44.3
	r_{6s}	[mm]	31.0
	r_{6h}	[mm]	20.3
	b_4	[mm]	1.77
	Z_r	[−]	17
	t_6	[mm]	0.89
	A_5	[mm^2]	681[a]
	L_z	[mm]	16.0
	c_r	[mm]	24.6
	ϵ_a	[mm]	0.40
	ϵ_r	[mm]	0.40
	ϵ_d	[mm]	2.21

[a] Computed such that the performance analysis at the design point and the design optimization predict equal flow angles.

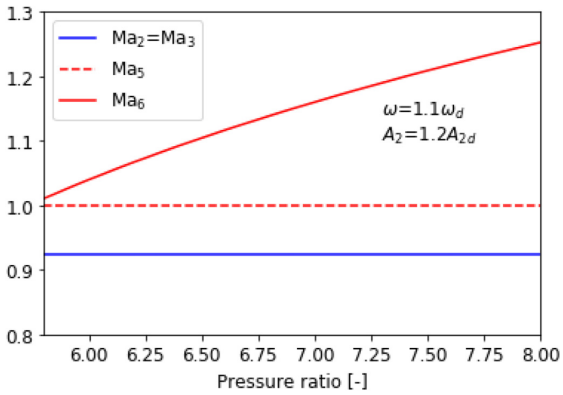

Fig. 12. Mach number at the throat and outlet of the blade rows from the performance analyses with the largest rotational speed and nozzle throat area.

attributed almost exclusively to the kinetic energy loss. The reason why some of the losses depicted in Fig. 15 (e.g., rotor passage and clearance losses) seem to decrease when the pressure ratio increases beyond the rotor choking point is that they are expressed in terms of efficiency loss, rather than as a change in enthalpy.

In order to assess the computational efficiency and robustness of the performance analysis method, all performance analyses applied the same set of start values for the independent variables. The start values of the velocity variables were equal to the corresponding optimized values from the design optimization, whereas the start values of the entropy variables were equal to 1.0. All performance analyses converged to the feasible solution at the first attempt within less than 2.5 s, see Fig. 16. This is a strong indication that the performance analysis method reliably converges to the feasible solution despite the non-smooth transition between subsonic and supersonic flow. Although the performance analysis involves fewer independent variables and constraints than the design optimization, the computational cost of the two methods is comparable. The main reason for this is that the performance analysis requires an inner iteration to compute the thermodynamic state at the throat of the blade rows when the flow conditions are supersonic. Indeed, as depicted in Fig. 16, there is a positive correlation between the execution time and the nozzle outlet Mach number.

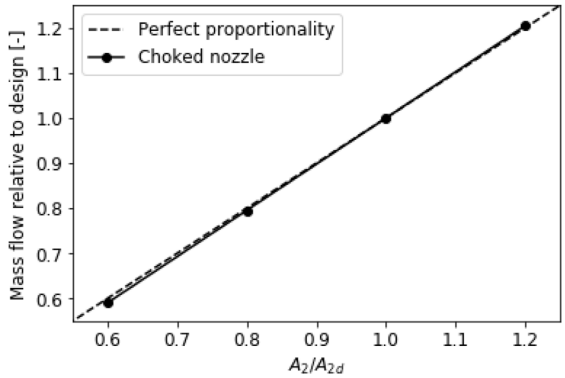

Fig. 13. Relationship between mass flow rate and nozzle throat area from the performance analyses.

5. Conclusion

This paper presented a method for the design optimization of RITs. In contrast with other design methods documented in the open literature, the proposed method was formulated following an equation-oriented approach and it uses equality constraints, rather than inner iteration loops, to close the model equations. As a result, the gradient-based algorithm used to solve the problem does not need to satisfy the model equations at each intermediate optimization iteration and the computational cost of the problem is reduced significantly. In addition, the present paper also presented a method to analyze the performance of RITs. The novelty of the proposed performance analysis method lies in the numerical treatment of choked flow conditions. Indeed, the method uses a predefined outlet pressure, rather than a predefined mass flow, to guarantee that the underlying mathematical problem has a unique solution, and it automatically detects whether the nozzle and rotor blade rows are choked. This is different from other performance analysis methods documented in the open literature, which are only suitable for subsonic flow conditions or need an a priori numerical solution strategy to identify whether any blade rows are choked.

Both the design optimization and performance analysis methods are based on a mean-line flow model and use an empirical loss model to account for the irreversibilities occurring within the turbine. The mean-line model was validated against two comprehensive sets of experimental data concerning RITs operating at different pressure ratios, rotational speeds and nozzle throat openings. It was found that the RMS deviation between the isentropic efficiency and mass flow rate predicted by the mean-line model (when using the original loss model) and the experimental measurements was less than 4% points and 3.5 %, respectively. Moreover, the mean-line model was able to correctly predict the trends of isentropic efficiency and mass flow rate as a function of the pressure ratio, rotational speed and nozzle throat area.

Finally, in order to demonstrate their capabilities, the design optimization and performance analysis methods proposed in this work were applied to design and predict the performance of the RIT of an ORC operating with propane as working fluid. The design optimization problem was solved starting from 100 random initial values of the independent variables, and the method converged to essentially the same solution. Although not formally proved, this gives a strong indication that the optimization algorithm reliably converges to the global optimum solution despite the non-smooth

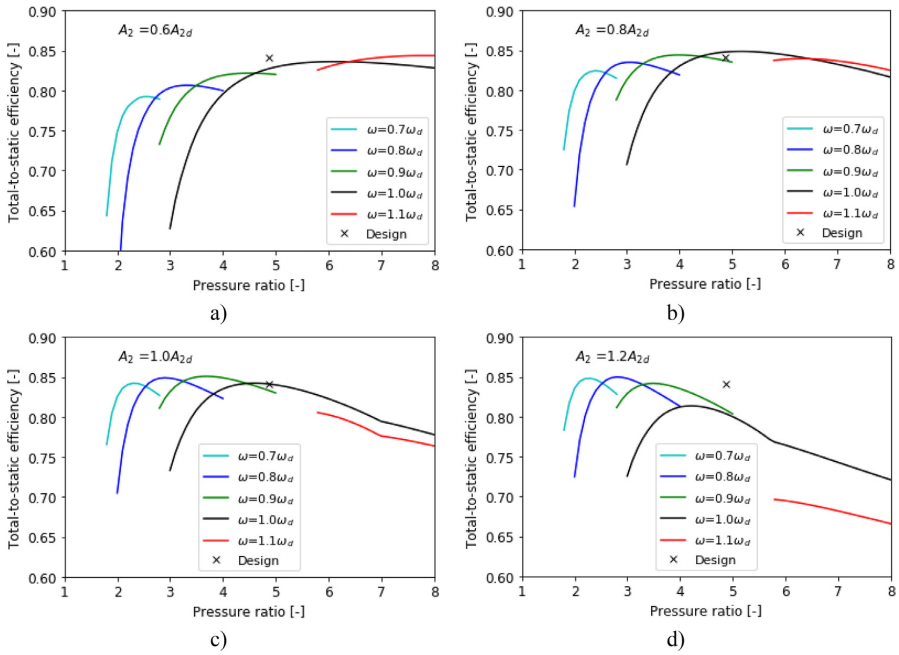

Fig. 14. Predicted efficiency vs. pressure ratio for different rotational speeds and nozzle throat areas.

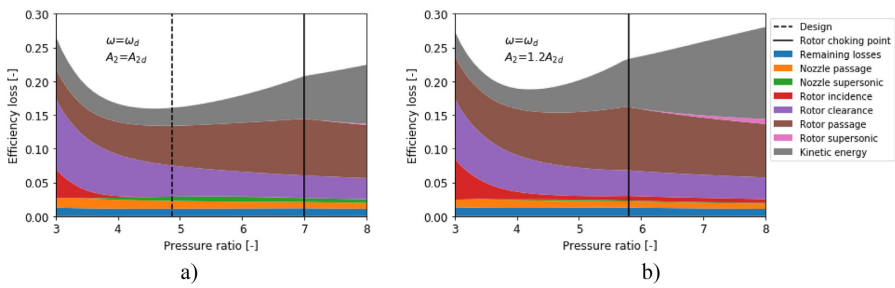

Fig. 15. Loss distribution vs. pressure ratio from some of the performance analyses.

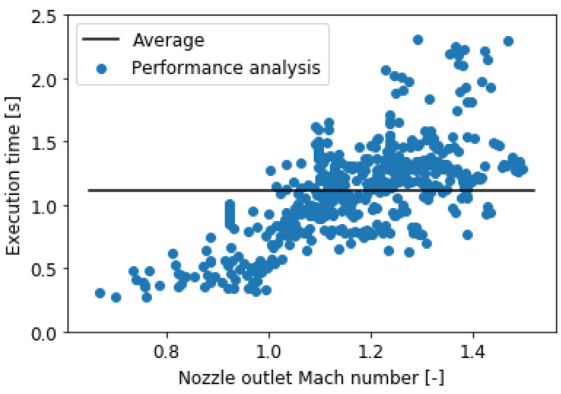

Fig. 16. Execution time vs. nozzle outlet Mach number from the performance analyses.

transition between subsonic and supersonic velocities within the mean-line model. In addition, the performance maps predicted by the performance analysis method are physically consistent and agree with general findings from experimental works available in the open literature. Notably, the performance analysis method predicts that the mass flow rate increases with the pressure ratio until choking occurs and that the corresponding mass flow rate is roughly proportional to the throat area of the choked blade row. Considering the accuracy, robustness and low computational cost of the proposed methods, they can be regarded as a powerful tool for the preliminary design and performance prediction of RITs, either as a standalone component or as part of an integrated system such as a Rankine cycle power system.

Declaration of competing interest

The authors declare that they have no known competing financial interests or personal relationships that could have

appeared to influence the work reported in this paper.

Acknowledgments

This publication has been funded by HighEFF - Centre for an Energy Efficient and Competitive Industry for the Future, an 8-years' Research Centre under the FME-scheme (Centre for Environment-friendly Energy Research, 257632). The authors gratefully acknowledge the financial support from the Research Council of Norway and user partners of HighEFF.

Appendix A. Implementation of the loss models

This Appendix describes the implementation of the loss model proposed by Meroni et al. [21]. The Reynolds number in the nozzle passage loss correlation, Eq. (9), was computed using properties at the nozzle throat and the blade height as the characteristic length, Eq. (A.1).

$$Re_2 = C_2 b_3 / \nu_2 \tag{A.1}$$

The trailing edge and supersonic loss correlations were originally proposed by Glassman [41] and Aungier [16](p. 82), respectively. However, in their original form they were expressed in terms of the total pressure loss coefficient. The factor Y_i in Eqs. (10), (11), (15) and (18) was included to convert the total-pressure-based loss correlations to enthalpy-based loss correlations. The expression for the conversion factor Y_i is given by Eq. (A.2) and it was proposed by Horlock [42].

$$Y_i = \left[1 + \frac{k_i - 1}{2} Ma_i^2\right]^{-\frac{k_i}{k_i - 1}} \tag{A.2}$$

The rotor incidence loss was implemented differently in the design optimization and the performance analysis methods. The incidence loss was disregarded in the design optimization, whereas in subsequent performance analyses the optimal rotor inlet angle, $\beta_{4,opt}$, was assigned the value of the flow angle from the design optimization, i.e. $\beta_{4,opt} = \beta_{4,d}$. This approach of forcing the minimum incidence loss to occur at the design point was proposed in Ref. [12](p. 238).

The optimal rotor inlet relative flow angle was not given in the references of the experimental data used for model validation. Therefore, a correlation given by Eq. (A.3) was applied to estimate $\beta_{4,opt}$ during the model validation.

$$\tan \beta_{4,opt} = \frac{-1.98 \tan \alpha_4}{Z_r - 1.98} \tag{A.3}$$

The rotor passage loss correlation, Eq. (14), requires the parameters L_H, D_H, c_r to be estimated. Moustapha et al. [12](p. 226) suggest to estimate the hydraulic length as the average of two quarter circles, Eq. (A.4), the hydraulic diameter as the average of the inlet and outlet hydraulic diameter, Eq. (A.5), and the rotor chord length according to Eq. (A.6). For the case of Jones' turbine [27], the value of the rotor chord was obtained from Ref. [39] rather than from Eq. (A.6).

$$L_H = \frac{\pi}{4}\left[L_z - \frac{b_4}{2} + r_4 - r_{6s} + \frac{b_6}{2}\right] \tag{A.4}$$

$$D_H = \frac{1}{2}\left[\frac{4\pi r_4 b_4}{2\pi r_4 + Z_r b_4} + \frac{2\pi\left(r_{6s}^2 - r_{6h}^2\right)}{\pi(r_{6s} + r_{6h}) + Z_r b_6}\right] \tag{A.5}$$

$$c_r = \frac{L_z}{\cos\overline{\beta}},\ \tan\overline{\beta} = \frac{1}{2}\tan\beta_{6b} \tag{A.6}$$

To the best of our knowledge, there exists no reliable correlation for the rotor deviation angle, $\delta_6 = \beta_6 - \beta_{6b}$. In addition, the use of blade metal angles is restricted to the loss model only. For these reasons the deviation angle is assumed zero unless the blade metal angle is known a priori, as was the case for the rotor in Spence et al. [29,30].

The factors K_a and K_r in the clearance loss correlation were computed by Eq. (A.7), and the derivation of these factors can be found in Ref. [12] (p. 229).

$$K_a = \frac{1 - r_{6t}/r_4}{C_{m4}},\ K_r = \frac{r_{6t}}{r_4} \cdot \frac{L_z - b_4}{C_{m5} r_6 b_6} \tag{A.7}$$

The friction coefficient, K_f, in the disc friction loss correlation, Eq. (17), is computed according to Eq. (A.8). This approach is similar to that of Meroni et al. [21] and the only difference is the value of the Reynolds number in which the transition between the laminar and the turbulent correlation occurs. As this work relies on the use of a gradient-based optimization algorithm, the transition Reynolds number of $1.58 \cdot 10^5$ was used to ensure a continuous transition between laminar and turbulent flow.

$$K_f = \begin{cases} 3.7(\varepsilon_d/r_4)^{0.1} Re_4^{-0.5},\ Re_4 = \dfrac{U_4 r_4 \rho_4}{\mu_4} < 1.58 \cdot 10^5 \\ 0.102(\varepsilon_d/r_4)^{0.1} Re_4^{-0.2}, \quad Re_4 > 1.58 \cdot 10^5 \end{cases} \tag{A.8}$$

Credit author statement

Brede A. L. Hagen: Conceptualization, Methodology, Software, Investigation, Formal analysis, Writing – original draft, Writing – review & editing, Visualization Roberto Agromayor: Methodology, Writing – review & editing, Visualization Petter Nekså; Writing – review & editing, Supervision.

References

[1] Macchi E. Theoretical basis of the organic rankine cycle. In: Macchi E, Astolfi M, editors. Organic Rankine cycle (ORC) power systems: Technologies and applications. Woodhead Publishing; 2017. p. 3–24.
[2] Tian H, Shu GQ. Organic Rankine Cycle systems for large-scale waste heat recovery to produce electricity. In: Macchi E, Astolfi M, editors. Organic Rankine cycle (ORC) power systems: Technologies and applications. Woodhead Publishing; 2017. p. 613–36.
[3] Guercio A, Bini R. Biomass-fired Organic Rankine Cycle combined heat and power systems. In: Macchi E, Astolfi M, editors. Organic Rankine cycle (ORC) power systems: Technologies and applications. Woodhead Publishing; 2017. p. 527–67.
[4] Orosz M, Dickes R. Solar thermal powered organic rankine cycles. In: Macchi E, Astolfi M, editors. Organic Rankine cycle (ORC) power systems: Technologies and applications. Woodhead Publishing; 2017. p. 569–612.
[5] Spadacini C, Xodo LG, Quaia M. Geothermal energy exploitation with organic rankine cycle technologies. In: Macchi E, Astolfi M, editors. Organic Rankine cycle (ORC) power systems: Technologies and applications. Woodhead Publishing; 2017. p. 473–525.
[6] Tchanche BF, Pétrissans M, Papadakis G. Heat resources and organic Rankine cycle machines. Renew Sustain Energy Rev 2014;39:1185–99.
[7] Colonna P, et al. Organic rankine cycle power systems: from the concept to current technology, applications, and an outlook to the future. J Eng Gas Turbines Power 2015;137(10):1–19.
[8] Capra F, Martelli E. Numerical optimization of combined heat and power Organic Rankine Cycles – Part B: simultaneous design & part-load optimization. Energy Oct. 2015;90:329–43.
[9] Song J, Gu C, Ren X. Influence of the radial-inflow turbine efficiency prediction on the design and analysis of the Organic Rankine Cycle (ORC) system. Energy Convers Manag Sep. 2016;123:308–16.
[10] Chatzopoulou MA, Simpson M, Sapin P, Markides CN. Off-design optimisation

of organic Rankine cycle (ORC) engines with piston expanders for medium-scale combined heat and power applications. Appl Energy Mar. 2019;238:1211–36.
[11] Bahamonde S, Pini M, De Servi C, Rubino A, Colonna P. Method for the preliminary fluid dynamic design of high-temperature mini-organic rankine cycle turbines. J Eng Gas Turbines Power 2017;139(8):1–14.
[12] Moustapha H, Zelesky MF, Baines NC, Japikse D. Axial and radial turbines. Vermont, USA: Concepts NREC; 2003.
[13] Valdimarsson P. "Radial inflow turbines for organic rankine cycle systems. In: Macchi E, Astolfi M, editors. Organic Rankine cycle (ORC) power systems: Technologies and applications. Woodhead Publishing; 2017. p. 321–34.
[14] Schuster S, Markides CN, White AJ. Design and off-design optimisation of an organic Rankine cycle (ORC) system with an integrated radial turbine model. Appl Therm Eng Jun. 2020;174:115192.
[15] Li S, Krivitzky EM, Qiu X. Meanline modeling of a radial-inflow turbine nozzle with supersonic expansion. In: Proceedings of the ASME Turbo Expo:Turbomachinery Technical Conference and Exposition; 2016. p. 1–14.
[16] Aungier RH. Turbine aerodynamics: axial-flow and radial-inflow turbine design and analysis. New York: ASME Press; 2005.
[17] Hu D, Li S, Zheng Y, Wang J, Dai Y. Preliminary design and off-design performance analysis of an Organic Rankine Cycle for geothermal sources. Energy Convers Manag May 2015;96:175–87.
[18] Demierre J, Rubino A, Schiffmann J. Modeling and experimental investigation of an oil-free microcompressor-turbine unit for an organic rankine cycle driven heat pump. J Eng Gas Turbines Power 2015;137(3):1–10.
[19] Song J, Gu C, Ren X. Parametric design and off-design analysis of organic Rankine cycle (ORC) system. Energy Convers Manag Mar. 2016;112:157–65.
[20] Da Lio L, Manente G, Lazzaretto A. A mean-line model to predict the design efficiency of radial inflow turbines in organic Rankine cycle (ORC) systems. Appl Energy Nov. 2017;205:187–209.
[21] Meroni A, Robertson M, Martinez-Botas R, Haglind F. A methodology for the preliminary design and performance prediction of high-pressure ratio radial-inflow turbines. Energy Sep. 2018;164:1062–78.
[22] Alshammari F, Karvountzis-Kontakiotis A, Pesiridis A, Giannakakis P. Off-design performance prediction of radial turbines operating with ideal and real working fluids. Energy Convers Manag Sep. 2018;171:1430–9.
[23] Du Y, Chen K, Dai Y. A study of the optimal control approach for a Kalina cycle system using a radial-inflow turbine with variable nozzles at off-design conditions. Appl Therm Eng Feb. 2019;149:1008–22.
[24] Liu C, Gao T. Off-design performance analysis of basic ORC, ORC using zeotropic mixtures and composition-adjustable ORC under optimal control strategy. Energy Mar. 2019;171:95–108.
[25] Zhou K, Wang J, Xia J, Guo Y, Zhao P, Dai Y. Design and performance analysis of a supercritical CO2 radial inflow turbine. Appl Therm Eng 2020;167(December 2019):114757.
[26] Lee S, Yaganegi G, Mee DJ, Guan Z, Gurgenci H. Part-load performance prediction model for supercritical CO2 radial inflow turbines. Energy Convers Manag 2021;235(March):113964.
[27] Jones AC. Design and test of a small, high pressure ratio radial turbine. J Turbomach 1996;118(2):362–70.
[28] Hagen BAL, Cavo M, Andresen T, Nekså P. Gradient based design optimization of a radial inflow turbine. In: IIR Rankine 2020 Conference; 2020.
[29] Spence SW, Artt DW. Experimental performance evaluation of a 99.0 mm radial in flow nozzled turbine with different stator throat areas. In: Proceedings of the Institution of Mechanical Engineers, Part A: Journal of power and energy, vol. 211; 1997. p. 477–88.
[30] Spence SWT, Doran WJ, Artt DW. "Experimental performance evaluation of a 99.0 mm radial inflow nozzled turbine at larger stator-rotor throat area ratios. Proc Inst Mech Eng Part A J Power Energy 1999;213(3):205–18.
[31] Perdichizzi A, Lozza G. Design criteria and efficiency prediction for radial inflow turbines. In: Gas turbine Conference and Exhibition; 1987. p. 1–9.
[32] Rohlik HE. Analytical Determination of radial inflow turbine design geometry for maximum efficiency. 1968. Washington D.C.
[33] Rodgers C. A cycle analysis technique for small gas turbines. In: Proceedings of the Institution of Mechanical Engineers. vol. 183; 1969. p. 37–49. 14.
[34] Dixon SL, Hall CA. Fluid Mechanics and thermodynamics of Turbomachinery. seventh ed. Oxford, UK: Butterworth-Heinemann; 2014.
[35] Lemmon EW, Bell IH, Huber ML, McLinden MO. NIST standard reference Database 23: reference fluid thermodynamic and Transport properties-REFPROP, Version 10.0, National Institute of standards and technology. 2018.
[36] Schittkowski K. NLPQL: a FORTRAN subroutine solving constrained nonlinear programming problems. Ann Oper Res 1985;5(1–4):485–500.
[37] Saravanamutto HIH, Rogers GFC, Cohen H, Straznicky PV. Gas turbine theory. sixth ed. Pearson Education; 2009.
[38] GNU operating system." [Online]. Available: www.gnu.org.
[39] Sauret E. Open design of high pressure ratio radial-inflow turbine for academic validation. In: Proceedings of the ASME International Mechanical engineering Congress and Exposition, vol. 7; 2012. p. 3183–97.
[40] Hagen BAL, Nikolaisen M, Andresen T. A novel methodology for Rankine cycle analysis with generic heat exchanger models. Appl Therm Eng Jan. 2020;165:114566.
[41] Glassman AJ. Enhanced analysis and users manual for radial-inflow turbine conceptual design code RTD. NASA Contractor Report 195454, no. Lewis Research Center; 1995.
[42] Horlock JH. Losses and efficiencies in axial-flow turbines. Int J Mech Sci 1960;2(1–2):48–75.

A.4 Paper IV

Equation-Oriented Methods for optimizing Rankine cycles using Radial Inflow Turbine

Brede A. L. Hagen, Trond Andresen, Petter Nekså.

The version of Paper IV attached in this thesis was submitted to *Energy* January 26. 2022 and accepted for publication April 1. 2022.

Equation-Oriented methods for optimizing Rankine Cycles using Radial Inflow Turbine

Brede A.L. Hagen[a], Trond Andresen[b], Petter Nekså[a,b]

[a] Department of Energy and Process engineering, NTNU – Norwegian University of Science and Technology, Kolbjørn Hejes vei 1B, NO-7491 Trondheim Norway
[b] SINTEF Energy Research

Abstract
This paper presents methods for optimizing the design and the performance of Rankine cycles using radial inflow turbines. Both methods follow a novel equation-oriented approach and involve a single mathematical problem that is solved by an efficient gradient-based algorithm. The capabilities of the proposed methods were demonstrated through a case study for power generation from the batch-wise casting process at a representative ferroalloy plant. More specifically, the proposed methods were used to design and analyze three Rankine cycles with CO_2 as the working fluid. The design optimization method converged in most cases to essentially the same solution regardless of the start values of the independent variables. The performance optimization method demonstrated that the control approaches with variable rotational turbine speed improved the turbine off-design efficiency over the control approaches with a constant rotational speed. Moreover, the control approaches with variable inlet guide vanes improved the thermodynamic performance of the cycle by facilitating operation at a higher pressure than the control approaches with a fixed geometry turbine. Considering the flexibility, robustness and the computational cost of the proposed methods, they can be regarded as a powerful tool for the preliminary design and performance prediction of Rankine cycles.

Nomenclature	
Roman symbols	
A_c	Cross-sectional flow area [m^2]
A_s	Heat transfer surface area [m^2]
A_5	Rotor throat area [m^2]
D_h	Hydraulic diameter [m]
L	Heat exchanger length [m]
h	Specific enthalpy [J/kg]
$\dot{m}$	Mass flow rate [kg/s]
o_n	Nozzle throat opening [m]
p	Pressure [Pa]
$P = 4A_c/D_h$	Channel perimeter [m]
R	Degree of reaction (turbine) [-]
s	Specific entropy [J/kg K]
T	Temperature [K]
$\dot{W}$	Net power output [W]
Z_r	Number of rotor blades [-]
Greek symbols	
α	Local heat transfer coefficient
Δ	Difference
ε	Effectiveness [-]
η_{EM}	Electro-mechanical conversion efficiency [-]
η_p	Pump isentropic efficiency []
η_T	Turbine isentropic efficiency (total-to-static) [-]
ν	Velocity ratio (turbine) [-]
ω	Rotational speed (turbine) [rad/s]
ω_s	Specific speed (turbine) [-]

Subscripts	
1-11	Rankine cycle state points, see Figure 2
c	Cold fluid
cond	Condenser
d	Design
h	Hot fluid
HX	Heat exchanger
recup	Recuperator
sink	Heat sink
src	Heat source
spec	Specification
wf	Working fluid
Abbreviations	
HTF	Heat transfer fluid
HX	Heat exchanger
PCHE	Printed circuit heat exchanger
PPTD	Pinch point temperature difference
RIT	Radial inflow turbine
VIGV	Variable inlet guide vane
VRS	Variable rotational speed

Keywords: *Gradient-based optimization; Mean-line model; Design; Off-design; Control approach*

1 Introduction

Increasing concerns of global warming due the emission of anthropogenic greenhouse gases has resulted in ambitious climate goals world-wide. For example, the European Union recently increased their ambition to reduce their greenhouse gas emissions by at least 55% within 2030 compared to the emission level in 1990 [1]. One key to reach this goal is to replace fossil energy, whose utilization emits the greenhouse gas CO_2, with more environmentally friendly heat sources for producing power. Examples of such energy sources are industrial surplus heat [2], biomass [3], solar energy [4] and geothermal energy [5]. These energy sources could provide a significant fraction of the worlds power demand [6], but their limited capacity and/or temperature constrain their widespread utilization. First, the use of steam Rankine cycle [7], is challenging for systems below a few MWe because the combination of small mass flow rate and large volume flow ratio lead to capital intensive expanders with low efficiency [8]. Although, the expander design challenge can be overcome by using an organic fluid [8], [9] or CO_2 [10] as the working fluid, the low efficiencies associated with power production from low temperature heat sources is a challenge for the profitability of any Rankine cycle system. Therefore, a key factor to enable further utilization of environmentally friendly heat sources for power production, is to increase the cost-effectiveness of Rankine cycle systems.

One way to achieve this in applications for which the heat source or sink characteristics vary with time is to account for the off-design performance of the system during the design phase. For instance, Capra and Martelli [11] demonstrated that a design optimization that takes into account the off-design performance of the Rankine cycle can significantly increase the cost-effectiveness of the system with respect to a conventional design approach that only accounts for the system performance at the nominal operating point. More specifically, Capra and Martelli [11] applied the two aforementioned methods to design a combined heat and power Rankine cycle and showed that the former resulted in up to 22% higher annual profit than the latter [12].

In addition, the efficiency of Rankine cycle systems whose design already exists can be increased by adopting a more flexible control approach. Indeed, Quoilin et al. [13] demonstrated that a control strategy allowing the evaporating pressure to vary yield better part-load performance compared to the control strategy with this pressure fixed to its value at the design point. In addition, Schuster et al. [14] demonstrated a significant performance improvement potential by equipping the turbine with movable nozzle blades. Finally, Dong et al. [15] demonstrated that the Rankine cycle performance can be improvement by regulating the rotational speed of the expander.

Among the different available expander architectures, the Radial Inflow Turbine (RIT) is particularly promising thanks to its high compactness and its capability to accommodate a large pressure ratio in a single stage [16]. In addition, the commercially available option of equipping the RIT with movable nozzle blades [17], [18], also known as variable inlet guide vanes (VIGV), enables efficient off-design operation[17].

To account for off-design performance of the Rankine cycle during the design phase and to consider various control approaches, it is necessary to apply accurate models. In this context the RIT model is of key importance because its efficiency and mass flow rate are strongly affected by operating conditions such as the pressure ratio, and by control variables such as nozzle throat opening and turbine rotational speed [19], [20]. Hagen et al. [21] recently proposed two equation-oriented methods for generating the preliminary design and predict the off-design performance of a RIT using a mean-line flow model. This paper proposes similar equation-oriented methods that govern Rankine cycles using a RIT and can be regarded as an extension of Hagen et al. [21].

A selection of methods for analyzing Rankine cycles using a RIT from the open literature is shown in Table 1 (design) and in Table 2 (off-design).

Table 1. Selection of methods for designing Rankine cycles using a RIT in the open literature.

Reference		RIT model	HX model	Optimization algorithm*
Hu et al. (2015)	[22]	Mean-line	Plate HX	Direct
Zhai et al. (2017)	[23]	Mean-line	Thermodynamic	Direct
Palagi et al. (2019)	[24]	(Mean-line)	(Thermodynamic)	Gradient (Direct)
Du et al. (2019)	[25]	Mean-line	Plate HX	Direct
Song et al. (2020)	[26]	Mean-line	Shell and tube	Not reported
Yao and Zou (2020)	[27]	Mean-line	PCHE	Not applicable
Li et al. (2021)	[28]	Mean-line	Thermodynamic	Direct
Present work		Mean-line	Generic	Gradient

* The type of optimization algorithm used (direct search or gradient based)

Most of the design methods summarized in Table 1 involves the use of a mean-line RIT model and is formulated as an optimization problem which is solved by a direct search optimization algorithm. A notable exception is the work by Palagi et al. [24] who trained several surrogate models on the basis of a mean-line RIT model and pinch point analysis, and solved the resulting optimization problem by a gradient-based optimization algorithm. Moreover, they demonstrated that the computational cost of their method was two orders of magnitudes lower than the method of using a direct search algorithm to solve the design problem on the basis of Rankine cycle model they used to train their surrogate models [24].

None of the design methods summarized in Table 1 considered the design of heat exchangers (HXs) as a part of the design optimization. Refs. [22]–[26] assumed for instance predefined pinch point temperature differences (PPTDs) in the HXs. However, some of the design methods applied technology specific models to design the HXs a posteriori. For example, Yao and Zou [27] designed the HXs and the RIT on the basis of predefined cycle state points and effectiveness of the recuperators.

Table 2. Selection of methods for off-design performance prediction of Rankine cycles using RIT in the open literature.

Reference		RIT model	HX model	Control variables
Walnum et al. (2013)	[29]	Constant efficiency	Compact HXs and Plate HX	p_4 and o_n
Hu et al. (2015)	[22]	Surrogate	Surrogate	p_4
Du et al. (2019)	[25]	Mean-line	Plate HX	p_4 and/or o_n
Schuster et al. (2020)	[14]	Mean-line	Not considered	o_n
This work		Mean-line	Generic	p_4 and any of o_n, ω

The Rankine cycle performance prediction methods summarized in Table 2 differ in the level of detail and in the in the approach for controlling the cycle. Walnum et al. [29] disregarded the turbine performance prediction by assuming a constant RIT efficiency and by allowing the working fluid mass flow rate and the pressure ratio to vary independently of each other. However, they indicated that their simplifications were acceptable due to the VIGV assumption and the moderate variation of the turbine operating conditions. Hu et al. [22] considered a sliding pressure control approach and applied surrogate models for the HXs and the RIT that was generated using a plate HX and a mean-line model, respectively. Schuster et al. [14] considered a constant pressure control approach and disregarded the HX performance prediction by predefining the turbine inlet temperature and the working fluid mass flow rate.

Du et al. [25] documents the most flexible Rankine cycle performance prediction method found in the literature search. They predicted the performance of a Kalina cycle using a RIT with VIGV considering three control approaches: The constant pressure, the sliding pressure and the *optimal* control approach where both the turbine inlet pressure and the nozzle throat opening were optimized simultaneously. Their results show that their *optimal* control approach yield a net power output improvement of up to 11% and 3% compared to the constant pressure and the sliding pressure control approach, respectively. However, they did not consider any control approaches involving variable rotational speed.

Considering the limitations of the methods surveyed in Table 1-Table 2, the aim of this paper is to present and demonstrate two methods for optimizing the design and the performance of Rankine cycles using RIT. The methods proposed in this work are based on a mean-line flow model of the RIT and a generic HX model and consist of the following novel aspects.

(1) The design optimization method optimizes the geometry of the RIT and the HXs, and the Rankine cycle state points simultaneously to maximize the design performance
(2) The performance optimization method allows any combination of the RIT control variables, (nozzle throat opening and rotational speed), to be optimized.
(3) Each of the methods follows an equation-oriented approach and involves the solution of a single mathematical problem that is solved by an efficient gradient-based optimization algorithm.

This paper is organized as follows. The HX- and RIT models, and the problem formulations for the design- and performance optimization methods are described in Sec. 2. The capabilities of the methods are demonstrated in Sec. 3 through a case study for power production from a time variable industrial surplus heat source. First the design optimization method is applied to design the HXs and the RIT of three different Rankine cycles. Thereafter the performance optimization method is applied to predict the annual electricity production from the Rankine cycles considering four different control approaches. The conclusions drawn from this study are summarized in Sec. 4.

2 Methodology

The proposed methods for Rankine cycle design optimization and performance optimization consist of a problem formulation, a Rankine cycle model, and a gradient-based optimization algorithm. The

illustration of the methods shown in Figure 1 is valid for both design optimization and performance optimization.

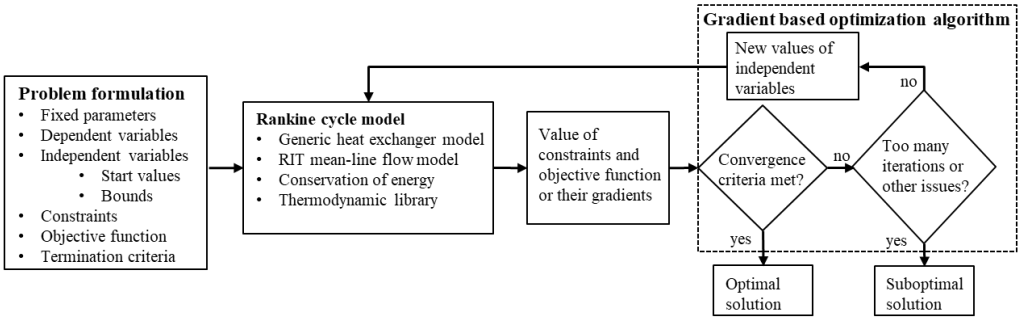

Figure 1 Overview of the methods for Rankine cycle design- and performance optimization.

2.1 The generic heat exchanger model

The present work adopted the generic HX (GHX) model that was introduced in Hagen et al. [30] for estimating HX size and fluid pressure drop. This model does not rely on a certain HX technology. Instead, the GHX model supports any two-fluid HX with a co-current of counter-current flow orientation. Moreover, it accounts for the geometry parameters that are used by the heat transfer coefficient- and pressure gradient correlations. The thermal-hydraulic correlations indicated in Table 3 were developed for channel flow and used to predict the local heat transfer coefficients and the pressure gradients in the HXs. Hence, the cross-sectional geometry of the HXs in this work can defined by the hydraulic diameter, D_h, and the cross-sectional flow area, A_c, for the channels of the hot and the cold fluid.

Table 3. Thermal-hydraulic correlations applied in this work.

	Heat transfer coefficient	**Pressure gradient**
Single phase	Gnielinski [31]	Selander [32]
Condensation	Shah [33]	Friedel [34]

The GHX model contain three ordinary differential equations (ODEs) describing heat transfer and fluid flow in a HX. The first ODE describes the relationship between the local heat transfer rate and the temperature difference between the two fluids:

$$\frac{dQ}{dx} = \frac{T_h - T_c}{R} \tag{1}$$

The thermal resistance between the two fluids accounts for convective heat transfer between the fluids and the HX wall, see Eq. (2).

$$R = \frac{1}{P_h \alpha_h} + \frac{1}{P_c \alpha_c} \tag{2}$$

The two remaining ODEs describe the change in pressure per unit length. The $\pm$ sign in Eq. (3) is required when integrating through a HX with a counter-current flow orientation: The pressure *decreases* when integrating along the flow direction, but *increases* when integrating against the flow direction.

$$\frac{dp}{dx} = \pm \left(\frac{dp}{dl}\right)_{corr} \tag{3}$$

The analytical solution to Eq. (1), commonly referred to as the LMTD method or the Effectiveness-NTU method, are commonly used but relies on the assumption of constant fluid properties [35]. The GHX model accounts for the variable fluid properties by solving Eqs. (1)) and (3) numerically as an *initial value* problem. This requires that both thermodynamic states at one end of the HX and a stop criterion are defined but enables a once-through calculation procedure.

In contrast to Hagen et al. [30] who used the HX length, L, as the stop criterion, this work introduces the fixed duty stop criterion. This reduces the complexity of the design optimization formulation compared to the formulation in Hagen et al. [30], because consistent duties can be assigned to the GHX model and the problem formulation contain no independent variables for the HX lengths, see Sec. 2.2.

The solution procedure of the GHX model starts at the end of the HX where the thermodynamic states of both fluids are defined ($x = 0$) by using the fourth order Runge-Kutta method to move a step Δx towards the other end (in the x-direction). The outcome of this step is the heat transfer rate and the pressure changes Δp_c, Δp_h that occurs over the interval $[0, \Delta x]$. After that the solution procedure moves step-by-step, as described above, until the accumulated heat transfer rate *exceeds* the predefined duty. At this point the length of the last step is reduced by 10 successive substitutions to ensure a consistent HX duty.

The output of the HX model that is processed to the Rankine cycle model is the heat transfer surface area (Eq. (4)) and the pressure drop of the two fluids.

$$A_s = (P_h + P_c)L \tag{4}$$

2.2 The Rankine cycle design optimization method

The design optimization method generates the preliminary design of a simple recuperated Rankine cycle, see Figure 2, that maximizes the thermodynamic performance at the design point. The independent variables, constraints and objective function for the Rankine cycle design optimization are shown in Table 4.

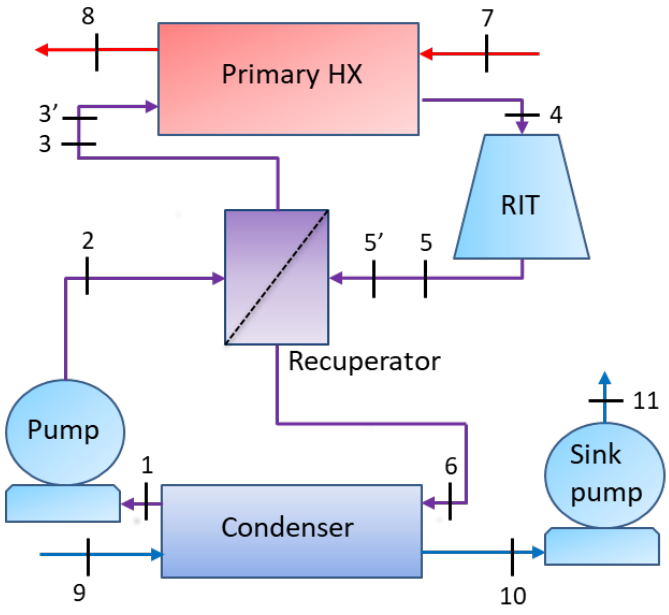

Figure 2. Illustration of the simple recuperated Rankine cycle analyzed in this work.

The objective of the optimization is to maximize the net power output, see Eq. (16). This objective function was chosen, instead of an economic one, due to the absence of a generic HX cost model. Instead, the cost of an optimized system can be estimated once the HX technology and the Rankine cycle application is determined. However, constraint(s) must be imposed to avoid oversized HXs. In contrast to the commonly used approach of predefining the PPTDs, see Refs. [22]–[26], the total HX surface area constraint guaranties that the available HX surface area are distributed optimally among the HXs.

The independent variables govern the cycle state points, component efficiencies and design parameters for the HXs and the turbine. One independent variable (the cross-sectional flow area) is introduced for each HX. These variables enable the optimal compromise between pressure drop and overall heat transfer coefficient in the HXs to be found [30]. The inclusion of turbine variables ensures a that the turbine is designed for maximum efficiency at the design point. These 12 variables govern both engineering decision variables such as specific speed and velocity ratio and parameters that are unknown a priori such as the relative velocity and the entropy at the outlet of the nozzle and the rotor. A complete list of the RIT design variables can be found in Hagen et al. [21].

All independent variables are constrained between an upper and a lower bound. Generally, the values of these bounds should be selected such that the optimal solution is not excluded by the bounds, or to avoid unphysical solutions, (e.g. entropy cannot decrease within turbomachinery) and unfeasible solutions. The bounds on the pressure variables may for instance be set to avoid too large internal pressures in the system or to avoid vacuum pressures. In addition, a non-recuperated Rankine cycle can be analyzed by allowing the recuperator effectiveness to be zero.

Table 4. Independent variables, constraints, and objective function for Rankine cycle optimization

Description	Symbol/formula	Design optimization	Performance optimization
Independent variables			
Pump inlet pressure	p_1	X	X
Pump outlet pressure	p_2	X	X
RIT inlet pressure	p_4	X	X
RIT inlet enthalpy	h_4	X	X
RIT outlet pressure	p_5	X	X
Heat source outlet temperature[a]	T_8	X	X
Recuperator effectiveness	ε_{recup}	X	X
RIT efficiency	η_T	X	X
Number of additional RIT variables		12	7
RIT rotational speed[b]	ω/ω_d		X
RIT nozzle throat opening[c]	$o_n/o_{n,d}$		X
Cross-sectional flow area[d]	A_c	X	
Constraints			
Consistent Primary HX inlet pressure	$p_3 = p_{3,}$	X	X
Consistent RIT outlet pressure	$p_5 = p_{5,}$	X	X
Consistent RIT efficiency	$\eta_T = \eta_{T,calc}$	X	X
Consistent HX length[e]	$L_{HX,calc} = L_{HX}$		X
Number of RIT equality constraints		6	8
Maximum total HX surface area	$\sum_{HX} A_{s,HX} \leq A_{s,spec}$	X	
Minimum degree of reaction - turbine	$R \geq 0.45$	X	
Objective function			
Maximize net power output, Eq. (16)	$\dot{W}$	X	X

[a] Optional – in this work fixed to the requirements of the heat recovery system
[b] Optional – in this work applied for the VRS and "VRS and VIGV" control approaches
[c] Optional – in this work applied for the VIGV and "VRS and VIGV" control approaches

[d] Three variables – one for each HX – each variable represents flow area for both fluids
[e] Three constraints – one for each HX

The Rankine cycle calculation procedure starts by computing the state-points of the cycle, see Figure 2. These state points are defined by pressure and specific enthalpy and once both properties are known the remaining thermophysical properties are computed by the thermodynamic framework. In this work the thermodynamic calculations were performed using REFPROP v10.0 [36]. The calculation procedure starts by computing the pump inlet state as saturated liquid. This enables the calculation of the pump outlet enthalpy using a prescribed pump efficiency and the independent variable for pump outlet pressure, Eq. (5).

$$h_2 = h_1 + [h(p_2, s_1) - h_1]/\eta_p \tag{5}$$

Thereafter the turbine outlet enthalpy is computed using the turbine operating conditions and efficiency defined by the independent variables, Eq. (6).

$$h_{5'} = h_5 = h_4 + [h(p_5, s_4) - h_4]\eta_T \tag{6}$$

Now, the maximum enthalpy change that can occur in the recuperator is computed as the enthalpy reduction that would occur if the turbine outlet were cooled down to the temperature of the pump outlet without pressure loss, Eq. (7).

$$\Delta h_{recup,max} = h_5 - h(p_5, T_2) \tag{7}$$

This enables the calculation of the enthalpy change in the recuperator using the recuperator effectiveness, Eq. (8).

$$\Delta h_{recup} = \varepsilon_{recup} \Delta h_{recup,max} \tag{8}$$

Then, the inlet enthalpy of the Primary HX and the condenser can be computed by Eqs. (9)-(10).

$$h_{3'} = h_3 = h_2 + \Delta h_{recup} \tag{9}$$

$$h_6 = h_5 - \Delta h_{recup} \tag{10}$$

The mass flow rates of the working fluid and heat sink can now be calculated by conservation of energy assuming that the HXs are thermally isolated from the ambient, Eqs. (11)-(12).

$$\dot{m}_{wf} = \frac{h_7 - h_8}{h_4 - h_3} \dot{m}_{src} \tag{11}$$

$$\dot{m}_{sink} = \frac{h_6 - h_1}{h_{10} - h_9} \dot{m}_{wf} \tag{12}$$

Now, the duty and the thermodynamic states at one end of each HX are defined enabling solving the HXs. More specifically, the Primary HX is solved from the hot to the cold end, and the recuperator and condenser are solved from the cold to the hot end using the GHX model described in Sec. 2.1. The outcome of the GHX model that are processed further is the pressures p_3, p_4, p_7, and p_{12} and the size (length and surface area) of each HX.

The RIT performance was accounted for by using the mean-line flow model documented in Hagen et. al. [21] This model assumes that the flow is *uniform* along the blade span, predicts the isentropic efficiency on the basis of an *empirical loss model* and has been *validated* against experimental data [21]. The RIT model starts by computing the isentropic enthalpy change, $\Delta h_{is} = h_5 - h(p_6, s_5)$ and the spouting velocity $C_0 = (2\Delta h_{is})^{0.5}$ using the RIT inlet state and outlet pressure defined by the independent variables. This enables the calculation of the rotational velocity and the rotor radius using the independent RIT variables for specific speed and velocity ratio by Eqs. (13)-(14)

$$\omega = \frac{(\Delta h_{is})^{0.75}}{\left(\dot{m}_{wf}/\rho_5\right)^{0.5}}\omega_s \tag{13}$$

$$r_4 = \frac{C_0}{\omega}\nu \tag{14}$$

Thereafter the independent RIT geometry variables are used to generate the RIT geometry. The geometry parameters involved in the mean-line model are illustrated in Figure 3 and the reader is referred to Hagen et al. [21] for further details on how their values are determined.

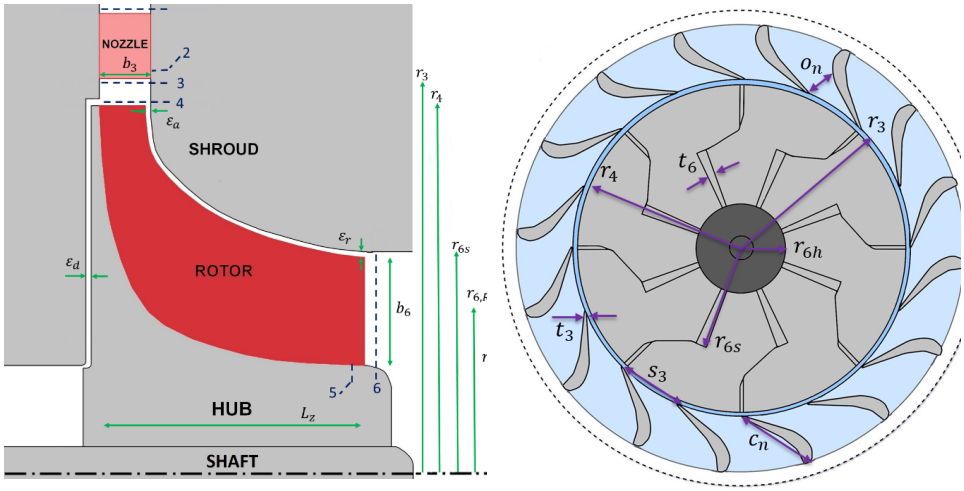

a) b)

Figure 3 Illustration of the RIT, and the geometry and state-points involved in the RIT mean-line model.

Thereafter the velocity triangles, the thermophysical properties and the losses in the RIT are computed using conservation equations, the remaining independent RIT variables and the empirical loss model (Eq. (1)-(18) in Hagen et al. [21]).

The sink pump increases the pressure of the heat sink fluid by a magnitude equal to the condenser heat sink pressure drop. More specifically, $p_{13} = p_{11}$ and the sink pump outlet enthalpy is computed by Eq. (15).

$$h_{11} = h_{10} + [h(p_{11}, s_{10}) - h_{10}]/\eta_p \tag{15}$$

The Rankine cycle calculation procedure ends by computing the net power output as the difference between the produced power and the power consumed by the pump motors accounting for the electro-mechanical conversions, Eq. (16).

$$\dot{W} = \dot{m}_{wf}(h_4 - h_5)\eta_{EM} - \dot{m}_{wf}(h_2 - h_1)/\eta_{EM} - \dot{m}_{sink}(h_{11} - h_{10})/\eta_{EM} \tag{16}$$

The design optimization method takes advantage of equality constraints to ensure that the Rankine cycle model is consistent. For instance, two equality constraints are imposed to ensure that $p_3 = p_{3'}$ and that $p_5 = p_{5'}$. In addition, an equality constraint is imposed to ensure that the value of the RIT efficiency variable equals the predicted value of the RIT model. The RIT equality constraints consists of the following: three constraints to ensure that the mass flow rate is conserved and that its value equals the working fluid flow rate computed by Eq. (11), two constraints to ensure that the entropy distribution defined by the independent variables are consistent with the predicted losses in the nozzle and the rotor, and one constraint to ensure that the rotor outlet pressure computed by the

RIT model equals p_5. The reader is referred to Hagen et al. [21] for the equations used to compute the RIT equality constraints.

In addition, other equality- or inequality constraints may readily be imposed to ensure that the optimization result satisfies additional design requirements such as dry expansion. In this work an inequality constraint was imposed to ensure a certain turbine degree of reaction. This constraint was proposed by Aungier [37] and applied by Hagen et al. [21].

The gradient-based optimization algorithm applied in this work was NLPQL [38]. This is a sequential quadratic programming (SQP) method that can be applied for solving both constrained optimization problems and systems of nonlinear equations. Gradients are calculated using a second order central difference approximation for numerical differentiation. The Kerush Kuhn Tucker (KKT) optimal criterion is set to 1.0E-4 and the maximum number of iterations is set to 100. This means that NLPQL returns an infeasible or suboptimal solution if the KKT optimal criterion is not met within 100 iterations or other issues occur [38], see Figure 1. This means that the iterative procedure indicated in Figure 1 repeats itself 100 times unless the KKT optimally criterion is met or other issues occur.

2.3 The Rankine cycle performance optimization method

The Rankine cycle performance optimization method maximizes the performance of a Rankine cycle whose design exists at a given operating condition (design or off-design). The independent variables, constraints and objective function for the Rankine cycle performance optimization method are shown in Table 4.

The performance optimization method has several similarities with the design optimization method. First it applies the same gradient-based optimization algorithm. Moreover, both methods have the similar set of independent variables and equality constraints related to cycle state points and component efficiencies, see Table 4, and their calculation procedures of the cycle (Eq. (5)-(12)) and HXs are identical. The main difference between the methods is that there are no independent component geometry variables in the performance optimization method. Instead, the geometry of the HXs and the RIT are solely defined by the fixed parameters. Furthermore, the novel treatment of choked flow introduced by Hagen et al. [21] which ensures physical consistent results in the case of supersonic velocities, is adopted in this work. This requires two additional independent variables and equality constraints to increase the resolution of the entropy distribution within the RIT and, in the case of supersonic velocities, an inner iteration to compute the thermodynamic state at the point where the flow velocity exceeds the speed of sound. The reader is referred to Hagen et al. [21] for further details on the performance evaluation of the RIT. Finally, the HX lengths are in the performance optimization method imposed as equality constraint to ensure consistent HX models.

The optional independent variables for turbine rotational speed and nozzle throat opening enable a selection of four approaches for controlling the Rankine cycle. The *sliding pressure* control approach occurs when both the turbine rotational speed and the nozzle throat opening are fixed parameters. This is a common approach for controlling Rankine cycles and involves changing the turbine inlet pressure to balance system parameters such as the working fluid mass flow rate [25]. This is the least flexible control approach considered in this work. Actually, if the heat source outlet temperature, T_8, is a fixed parameter, as is the case for the demonstration of the method, see Sec. 3, the number of equality constraints equals the number of independent variables. In this case the mathematical problem is a system of nonlinear equations with a single unique solution. Without an obvious reason for prescribing the heat source outlet temperature, T_8 should be an independent variable resulting in a mathematical problem for sliding pressure control approach with one degree of freedom.

The variable rotational speed (VRS) control approach occurs when the turbine rotational speed is an independent variable while the nozzle throat opening is a fixed parameter. VRS assumes that the turbo-generator system can deliver electric power at the grid frequency despite the variable turbine rotational speed. This can be achieved by using a high-speed generator and a flexible frequency converter system adjusting the frequency of the produced power to the grid frequency [15].

The variable inlet guide vane (VIGV) control approach occurs when the nozzle throat opening is an independent variable and the turbine rotational speed is a fixed parameter. VIGV assumes that the RIT is equipped with movable nozzle guide vanes that modifies the nozzle throat opening by rotating around a pivot point [17], [18].

In the fourth control approach, in this work referred to as "VRS and VIGV", both the nozzle throat opening, and the rotational speed are independent variables.

2.4 Discussion of the problem formulations

Developing effective methods for designing and analyzing Rankine cycles accounting for the physics within its main components is a challenging task that requires creativity and a solid understanding of the mathematical models involved. We believe the proposed methods for Rankine cycle design- and performance optimization have some advantages and contain some novelties that are worth highlighting.

- The proposed methods account for the thermophysical properties of the involved fluids by means of general heat transfer and pressure gradient correlations in the HXs and a loss model within the RIT model. One advantage of using general models based on physics is the confidence of obtaining results of reasonable accuracy for a broad range of conditions. Consequently, we regard the proposed methods applicable to design and analyze Rankine cycles for various applications (e.g. different heat sources and HX technologies) and with any fluid available in the thermodynamic library as a potential working fluid candidate. Moreover, the same underlying HX- and RIT model are applied for both the design- and the performance optimization method yielding a smooth transition between the two methods.
- The proposed methods avoids the need for defining the flow rates of the working fluid and the heat sink. Indeed, they are computed using HX energy balance, see Eqs. (11)-(12). We believe this simplifies the process of obtaining reasonable start values of the independent variables, and of adjusting them to different working fluids or heat source characteristics.
- In contrast with the published design methods in the Table 1, with the notable exception of the surrogate model approach in Ref. [24], the proposed design optimization method avoids the use of inner iteration(s) to compute the Rankine cycle performance. Indeed, all the equations involved requires only explicit computations (inner iterations are limited to thermodynamic function calls) and inner iteration loops are replaced by equality constraints that are handled by the optimization algorithm. Consequently, the Rankine cycle model doesn't have to be solved at each intermediate optimization iteration and an efficient gradient-based algorithm can be applied, leading to a reduction in the computational cost [39].

3 Case study

Energy-intensive industry release large amounts heat that can be utilized for power production. Germany industry for instance, releases more than 200 TWh every year to the environment and the annual electricity production potential from the steel, glass and cement industry alone using Rankine cycles are several TWh_e [40]. This section demonstrates the capabilities of the proposed methods through the design and performance prediction of Rankine cycles utilizing industrial surplus heat. The industrial facility is a representative Norwegian ferroalloy plant with an annual ferrosilicon production of 100 000 ton and we considered heat recovery from batch-wise metal casting. Each "batch" consists of an amount of liquid metal that is distributed into multiple molds in which it solidifies and cools down to ambient temperature. The latent and sensible heat that is released in this process is significant but seldom utilized [41]. However, a concept for capturing and utilizing this heat is proposed, see Ref. [42]. This heat recovery system consists of a cooling tunnel in which heat from the molds is transferred to a heat transfer fluid (HTF), thermal energy storage to smooth temperature variations, and a Rankine cycle as illustrated in Figure 4.

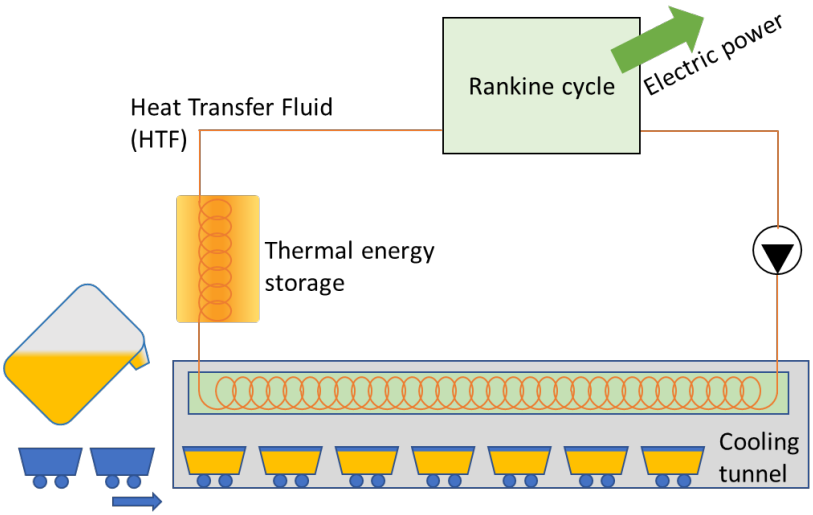

Figure 4. Concept diagram of the heat recovery system.

The time dependent HTF characteristics for a one-hour period, see Figure 5, were generated by means of the dynamic model of the heat recovery system described in Ref. [42]. In the first half an hour, molds containing liquid metal enter the cooling tunnel one by one as illustrated by the stepwise increase in the HTF temperatures and the Primary HX duty. In the second half an hour there is no further heat input to the cooling tunnel and the heat delivered to the Rankine cycle is mainly provided by the thermal energy storage, illustrated by the constantly decreasing HTF temperatures. The heat recovery system operates at a cyclic-steady state which means that the process depicted in Figure 5 repeats itself every hour.

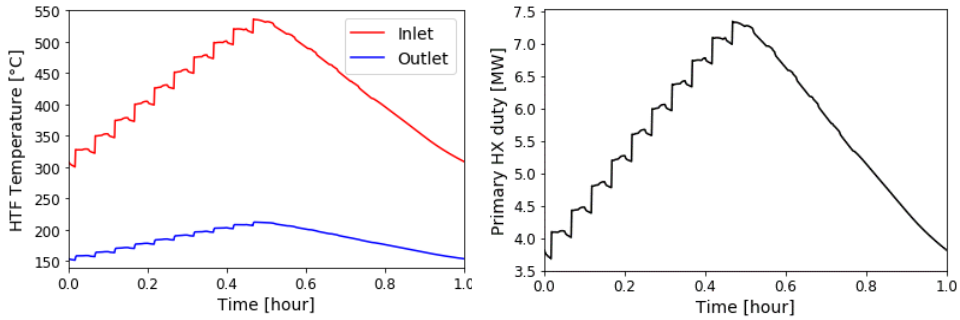

a) b)

Figure 5 Time-dependent characteristics of the Rankine cycle heat source.

3.1 Setup for the design optimizations

The present case study focuses on the Rankine cycle by considering the HTF characteristics as fixed parameters. Furthermore, the proposed methods rely on the RIT as the expander technology and the Rankine cycle layout depicted in Figure 2. Consequently, this section governs the selection of working fluid, HX technology and the remaining fixed parameters used for the design optimizations. The fixed parameters used for the present case study are shown in Table 5. The relatively low heat sink inlet temperature can be justified by the Norwegian climate. As the working fluid selection based on quantitative analysis is out of the scope of this article and the HTF temperature exceeds 500 °C we want to highlight a couple of advantages of our selected working fluid for the present case study: First, in contrast to most organic fluids whose thermal stability when their temperature exceeds 300-350°C could be questioned, CO_2 is stable at least up to 600 °C

[43]. Secondly, the moderate working fluid pressure ratio of CO_2 power cycles is ideal for applying a single stage RIT. Indeed the single stage RIT is regarded as the most suitable expander technology for CO_2 power cycles of a few MW_e [44].

Table 5 Fixed parameters of the Rankine cycle.

HTF medium	CO_2
HTF mass flow rate	18.2 kg/s
HTF pressure, p_7	200 bar
Heat sink medium	Water
Heat sink inlet temperature, T_9	10 °C
Heat sink outlet temperature, T_{10}	20 °C
Working fluid medium	CO_2
Maximum working fluid pressure, upper bound for p_2	200 bar [a]
HX hydraulic diameter, D_{hyd}	1.2 mm
Total HX surface area, $A_{s,spec}$	500 m^2 [b]
Pump efficiency, η_p	0.65
Electromechanical efficiency, η_{EM}	0.95

[a] Must be respected at both design and off-design operating conditions
[b] Only relevant for design optimization

Compact HXs such as PCHE, Plate fin or other HXs with micro tubes have been suggested for CO_2 Rankine cycles due to their high operating pressure [45]. For this reason, a low value for the hydraulic diameter was used such that the GHX model represented a generic compact HX. The value for D_h in Table 5 was used for the channels of both the hot and cold fluid in all HXs. Thus, the perimeter, or the heat transfer surface area per unit length of each channel in each HX were computed by Eq. (17) where A_c is an independent variable, see Table 4.

$$P_c = P_h = \frac{4A_c}{D_h}. \tag{17}$$

A theoretical study that accounted for the turbomachinery design demonstrated that the working fluid pressure that maximized the thermodynamic performance of a CO_2 Rankine cycle to be up to 400 bar [46]. On the other hand, existing CO_2 Rankine cycle prototypes considers much lower working fluid pressures [10]. Considering this discrepancy, an upper bound was set on the working fluid pressure to avoid proposing something unrealizable, see Table 5. The design optimizations were performed using the problem formulation from Table 4 and the fixed parameters in Table 5. The time dependent characteristics are limited to the HTF temperatures illustrated in Figure 6.

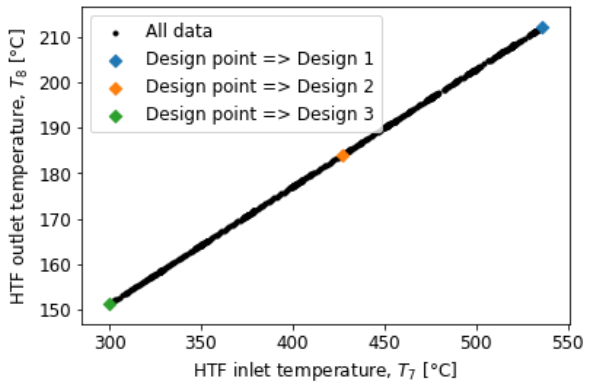

Figure 6. Scatterplot of the HTF temperatures from Figure 5(a). The characteristics used for the design optimizations leading to three *designs* are highlighted.

Three design points were considered. More specifically, one design optimization was carried out considering each of the three HTF characteristics indicated with colored markers in Figure 6 as fixed parameters. The numerical values of the design point HTF temperatures and the resulting Primary HX duties are shown in Table 6.

Table 6. Design point HTF characteristics adopted in this work.

Design		**1**	**2**	**3**
HTF inlet temperature, T_7	[°C]	535	427	300
HTF outlet temperature, T_8	[°C]	212	184	152
Primary HX duty	[MW]	7.33	5.61	3.68

3.2 Design optimization results

T-s diagrams of the Rankine cycle processes from the design optimizations are shown in Figure 7. All processes are transcritical because the high pressure exceeds the working fluid critical pressure while the low pressure is below the critical pressure illustrated by the heat rejection to the heat sink occurring within the phase envelope. Moreover, the pinch point of the Primary HX moves from its cold end (Design 1 and 2) to its hot end (Design 3).

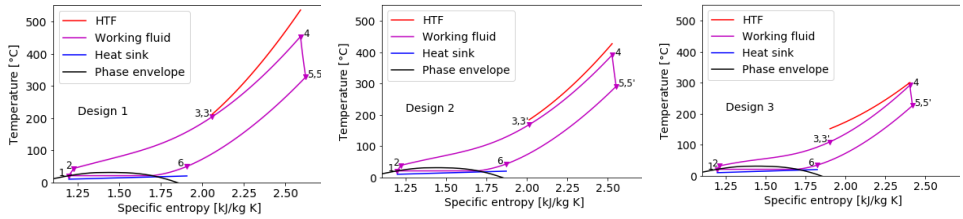

a) b) c)

Figure 7. T-s diagrams of the Rankine cycle processes obtained by the design optimizations.

Although Design 2 and Design 3 had a lower pump outlet pressure, p_2, than Design 1 this variable reached its upper bound in all cases. This was required to avoid working fluid pressure *exceeding* 200 bar at off-design operating conditions. Indeed, the blue curve in Figure 12(c) shows that p_2 increases with the HTF temperature for the sliding pressure control approach. The numerical values for p_2 of Design 2-3 shown in Table 7 were found by manually iterating between design optimization and a subsequent off-design performance prediction of the sliding pressure control approach.

Table 7. Selection of numerical results obtained by the Rankine cycle design optimizations.

Design		**1**	**2**	**3**
Pump outlet pressure, p_2	[bar]	200	163	120
Pump inlet pressure, p_1	[bar]	58.3	58.5	58.3
Working fluid mass flow rate	[kg/s]	23.5	20.2	15.9
Net power output	[MW]	2.14	1.41	0.66

The component geometry obtained by the design optimizations are shown in Table 8 (HXs) and

Table 9 (RIT). These tables show that the design point HTF characteristics do affect the optimized component geometry. Notably, there is positive correlation between turbine size and the design point Primary HX duty.

Table 8 HX geometry obtained by the Rankine cycle design optimizations.

Design		**1**	**2**	**3**
Primary HX length	[m]	1.59	1.71	1.40
Primary HX cross sectional area	[10^{-3} m^2]	12.5	13.4	15.8
Primary HX surface area	[m^2]	130	150	145
Recuperator length	[m]	1.06	1.09	1.14
Recuperator cross sectional area	[10^{-3} m^2]	23.7	21.8	20.8
Recuperator surface area	[m^2]	164	155	155
Condenser length	[m]	1.04	1.06	1.20
Condenser cross sectional area	[10^{-3} m^2]	30.3	28.2	25.5
Condenser surface area	[m^2]	205	195	200

Table 9. RIT geometry and rotational speed obtained by the Rankine cycle design optimizations.

Design			1	2	3
Nozzle	r_3	[mm]	88.61	84.75	78.81
	b_3	[mm]	3.45	3.69	4.06
	s_3	[-]	28.74	27.30	25.36
	$o_{n,d}$	[mm]	10.26	9.67	8.97
	t_3	[mm]	0.46	0.44	0.40
	c_n	[mm]	38.22	36.31	33.73
Rotor	r_4	[mm]	86.15	82.13	75.94
	r_{6s}	[mm]	60.31	57.49	53.15
	r_{6h}	[mm]	43.25	40.88	36.97
	ω_d	[kRPM]	40.65	37.20	30.88
	b_4	[mm]	3.45	3.69	4.06
	Z_r	[-]	16	17	17
	t_6	[mm]	1.72	1.64	1.52
	A_5	[(cm)^2]	19.98	18.58	16.44
	L_z	[mm]	25.59	24.92	24.27
	c_r	[mm]	41.88	40.64	39.84
	ε_a	[mm]	0.40	0.40	0.40
	ε_r	[mm]	0.40	0.40	0.40
	ε_d	[mm]	4.31	4.11	3.80
Rotor visualization (sizes in mm)			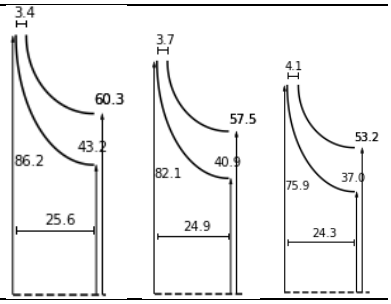		

One drawback of gradient-based optimization algorithms is that they may converge to a local optimum close to the starting point used for optimization. In addition, the convergency to an optimum is only guaranteed if the involved functions are smooth. The numerical routines within

the thermodynamic framework and the successive substitution method within the GHX model might be sources of non-smoothness. To assess the robustness of the proposed design optimization method, we carried out 100 optimizations of Design 1 using random start values of the independent variables. Only two of these failed to converge to an optimum. This is an indication that the above-mentioned sources of non-smoothness are not a major concern for convergency. The objective function value and the execution time obtained on a personal computer with an Intel Core i7-8650U processor from the remaining optimizations are shown in Figure 8. As seen in Figure 8(a), most of the optimizations yield almost the same maximized net power output. More specifically, the 88 best optimizations deviate with less than 0.01% in terms of net power output and 2% in terms of optimized values of the independent variables. The consistency in the optimization results is a strong indication that the optimization problem contains few local optimums and that the gradient-based algorithm in most cases converged to the global optimum. The average execution time was 11.5 minutes and 53 % of the simulations spent less than 10 minutes to converge, see Figure 8(b).

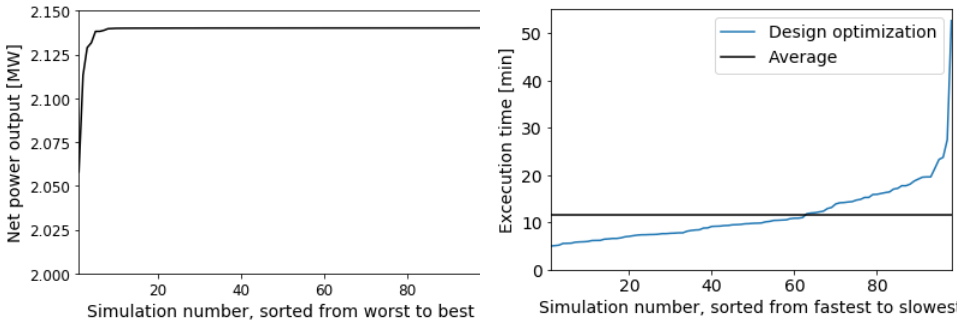

a) b)

Figure 8. Objective function value (a) and execution time (b) from 98 of the 100 optimizations of Design 1 that converged to an optimum. The independent variables were assigned random start values in all cases.

3.3 Setup for the performance optimizations

The performance optimizations were carried out using the independent variables, constraints and the objective function showed in Table 4. In addition, the parameters of Table 5 and the component geometries in Table 8

Table 9 were provided as fixed parameters.

One purpose of the performance optimizations is to estimate the annual electricity production from the Rankine cycles designed in the previous section. To this aim the performance of these Rankine cycles were evaluated at five different HTF characteristics, see Figure 9. The scatterplot in Figure 9 shows a perfect linear correlation between the HTF inlet and outlet temperatures. Consequently, the HTF temperatures were defined by the HTF inlet temperature, see Figure 10-Figure 13, because it has only one corresponding HTF outlet temperature. Finally, all four approaches for controlling the Rankine cycle described in Sec 2.3 were considered.

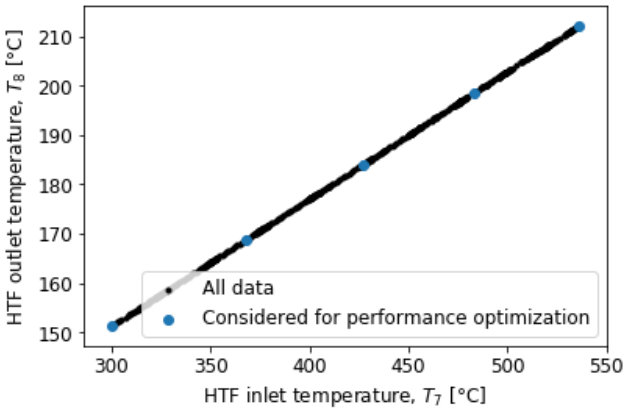

Figure 9. Scatterplot of the HTF temperatures from Figure 5(a). The characteristics used for the performance optimizations are highlighted.

3.4 Performance optimization results

3.4.1 Design 1

The performance optimization results of Design 1 are shown in Figure 10. Each of the plots (a,b,c,d) govern a certain performance metric, whereas each colored line represents a certain control approach. The result from the corresponding design optimization is highlighted with a black diamond shaped marker.

Figure 10(a) shows that working fluid mass flow rate is decreasing with decreasing HTF inlet temperature. One option for reducing the turbine mass flow rate is to reduce the pressure ratio across the RIT [21]. Indeed, Figure 10(b) shows that the maximum working fluid pressure decreases with decreasing HTF inlet temperature for the sliding pressure and the VRS control approach. Alternatively, the mass flow rate may be reduced by reducing the nozzle throat opening [21]. Indeed, the VIGV and "VRS and VIGV" control approaches maintain the maximum working fluid pressure around 200 bar by reducing the nozzle throat opening, see Figure 10(b) and Figure 11 (b).

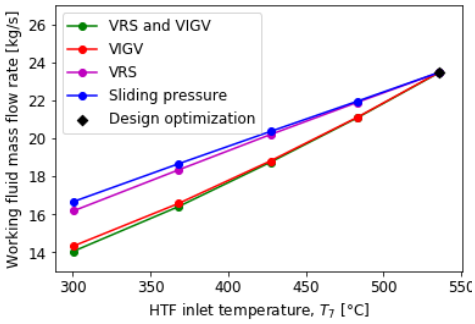

a)

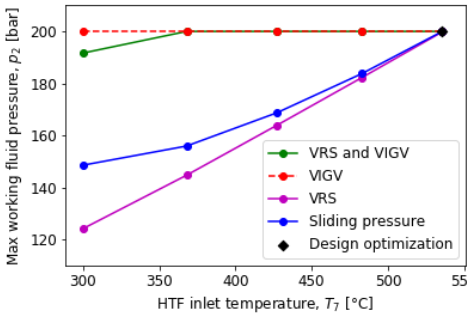

b)

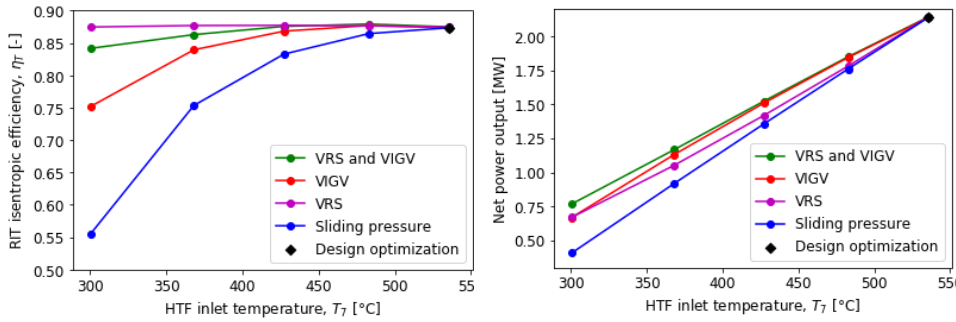

c) d)

Figure 10. Performance optimization results of Design 1.

Figure 10(c) shows that the turbine isentropic efficiency drops dramatically from the design value of 87.3% and down to 55.6% for the *sliding pressure* control approach and that the other control approaches improve the off-design RIT efficiency. Notably the VRS and "VRS and VIGV" control approach improves the RIT efficiency by reducing the rotational speed, see Figure 11(a).

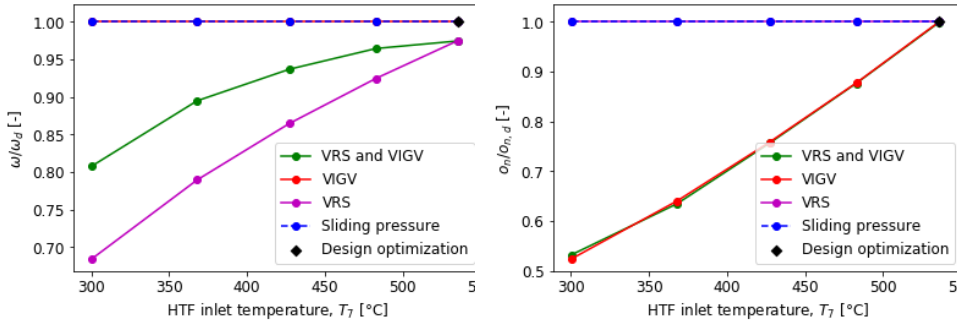

a) b)

Figure 11. Optimized values of the RIT control variables obtained from the performance optimizations of Design 1.

The net power output is shown in Figure 10(d). All control approaches yield similar performance at the design point. However, the sliding pressure control approach yield a lower off-design performance than the other control approaches. VRS outperforms the sliding pressure control approach due to the improved RIT isentropic efficiency, while the improvements of the VIGV are mainly due to the higher working fluid pressure.

3.4.2 Design 2

The main results from the performance optimizations of Design 2 are shown in Figure 12. Similarly, as for Design 1, VIGV and "VRS and VIGV" control approaches facilitate operation with higher working fluid pressure than sliding pressure by reducing the nozzle throat opening, see Figure 12(b,c). Indeed, the pump outlet pressure of the VIGV control approach went to its upper bound of 200 bar for all cases. The increased pump outlet pressure is beneficial from the thermodynamic point of view and VIGV outperforms the sliding pressure control approach for such cases which includes the design operating point, see Figure 12(d).

Figure 12(a) shows that the RIT efficiency of the sliding pressure control approach are higher than 80% in all cases except for the smallest HFT inlet temperature. Consequently, VRS yield only a slight net power improvement over the sliding pressure control approach, se Figure 12(d).

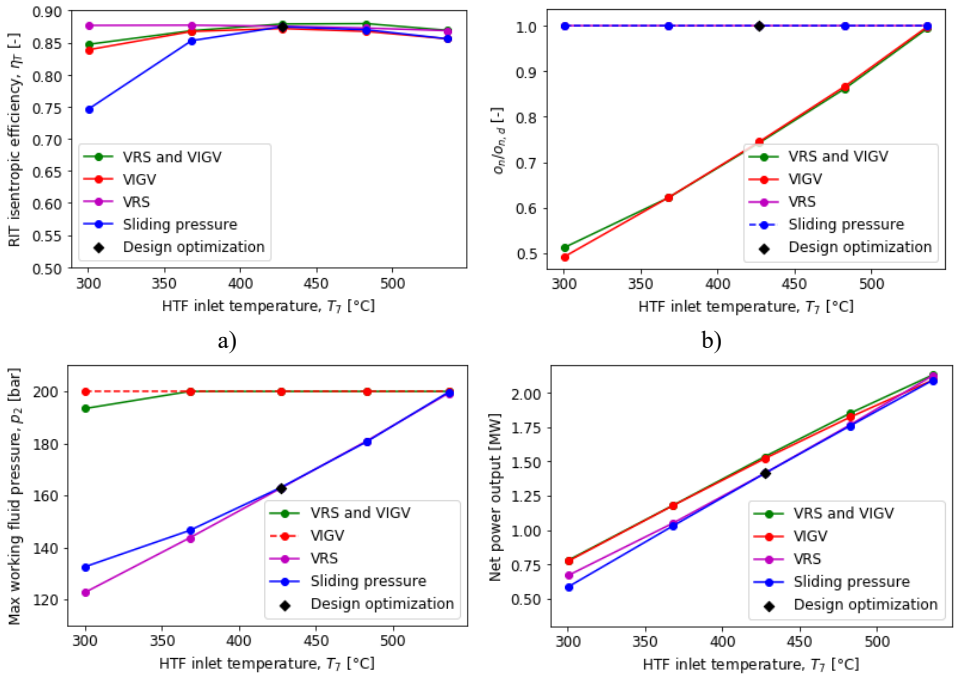

Figure 12. Performance optimization results of Design 2.

3.4.3 Design 3

The main results from the performance optimizations of Design 3 are shown in Figure 13. Figure 13(a) shows that the RIT isentropic efficiency drops from the design value of 87.6% and down to 74.3% for the sliding pressure control approach. In contrast to Design 1, VIGV yields a lower RIT efficiency than the sliding pressure control approach.

The net power output from Design 3 is shown in Figure 13(b). In this case VIGV yield only a slight performance improvement over the sliding pressure control approach. VRS also improves over the sliding pressure control approach, particularly at the largest HTF temperatures. "VRS and VIGV" maintain a significant net power improvement over sliding pressure control approach for all cases.

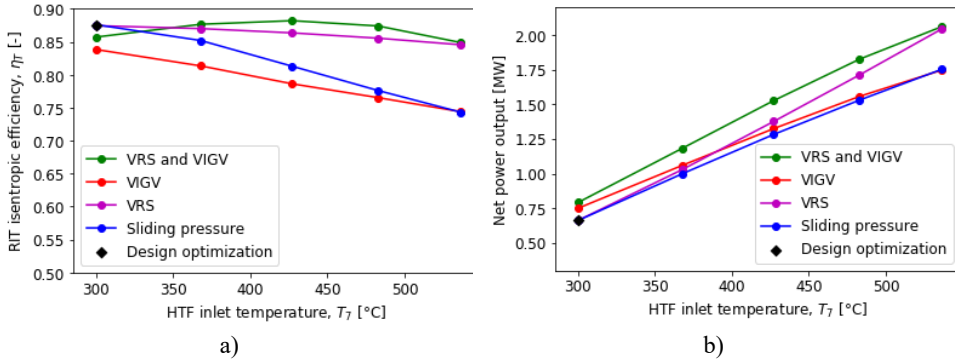

Figure 13. Performance optimization results of Design 3.

3.4.4 Computational cost

In order to assess the computational cost of the performance optimization method all performance optimization applied the same set of start values and bounds for most of the independent variables.

The only exception is the variable, h_5, whose bounds and start value was tailored accounting for the HTF inlet temperature. The average execution time of the performance optimizations of 3.2 minutes is less than one third of the average execution of the design optimizations. A possible explanation for this is that the performance optimization method involves fewer independent variables than the design optimization method. The execution time of the performance optimizations of sliding pressure, the control approach with fewest independent variables, is lower than the execution time of the performance optimizations of the other control approaches, see Figure 14.

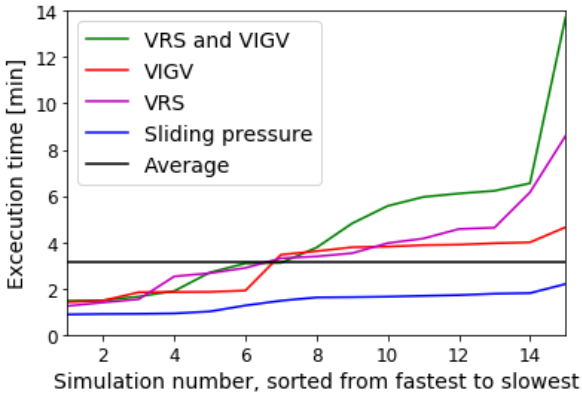

Figure 14 Execution time of the performance optimizations carried out in this work.

3.5 Discussion of the case study results

The results of the case study are summarized in Figure 15. The net power output vs. time shown in Figure 15(a,b,c) were estimated by means of linear interpolations using the HTF inlet temperature vs. time depicted in Figure 5(a) and the net power output results of Figure 10(d), Figure 12(d), Figure 13(b). Thereafter the hourly electricity production were estimated as the area under the curves in Figure 15(a,b,c) by the trapezoidal method for numerical integration. Finally, the annual electricity production estimates of Figure 15(d) were computed assuming that the system operates 95% of the year.

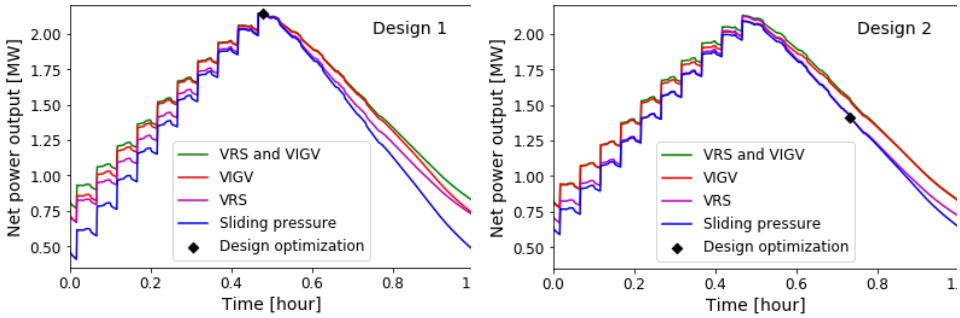

a) b)

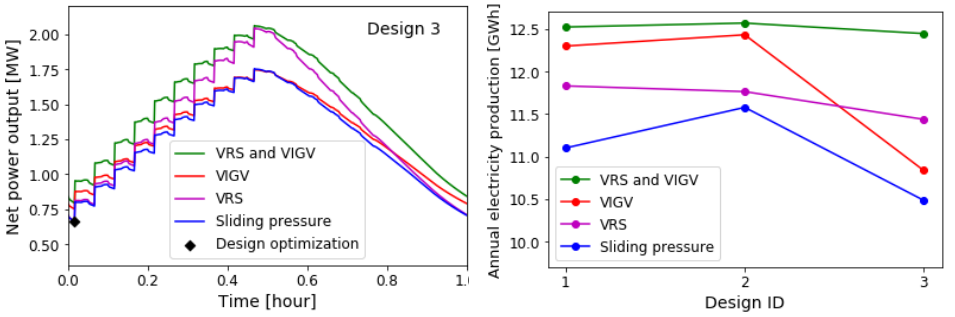

c) d)

Figure 15 Net power vs. time computed by linear interpolation for Designs 1-3 (a,b,c) and the resulting annual electricity production (d) from the present case study.

Figure 15(d) show that the "VRS and VIGV" yield the largest annual electricity production among the control approaches for all designs. In addition, and in contrast to the other control approaches, "VRS and VIGV" yield similar annual electricity production for the three designs indicating that the flexibility associated with this control approach compensates for the effect of RIT and HX design on the thermodynamic performance of the Rankine cycle.

Sliding pressure yield the lowest annual electricity production among the control approaches for all designs. Notably, the largest electricity production from the sliding pressure control approach occurs for Design 2 where the components were designed for an average operating point, see Figure 6, thus enabling the Rankine cycle to be operated closer to its design point than the other designs.

VIGV doesn't implicate improved RIT efficiency. Indeed, the results of Figure 10(c), Figure 12(a), Figure 13(a) show that VIGV only increase the RIT efficiency over the sliding pressure control approach for cases when the HTF inlet temperature is lower than its value at the design point. This agrees with the results of Du et al. [25] whose optimal control approach only predicted larger RIT efficiency than their sliding pressure control approach for the cases when the heat source quantity was lower than its design value.

One of the key parameters affecting the turbine efficiency is the velocity ratio defined as the ratio between the velocity of the rotor blade tip and the spouting velocity which is proportional to the square root of the isentropic enthalpy drop, see Eq. (14). Indeed, as depicted in Figure 16 there is a strong correlation between the RIT efficiency and the velocity ratio. The figure also show that the lower RIT efficiencies obtained by the sliding pressure and the VIGV control approaches are caused by the velocity ratio deviating from its design value. On the other hand, the VRS and "VRS and VIGV" control approaches optimized the rotational speed such that velocity ratio and the RIT efficiency are close to their values at the design point.

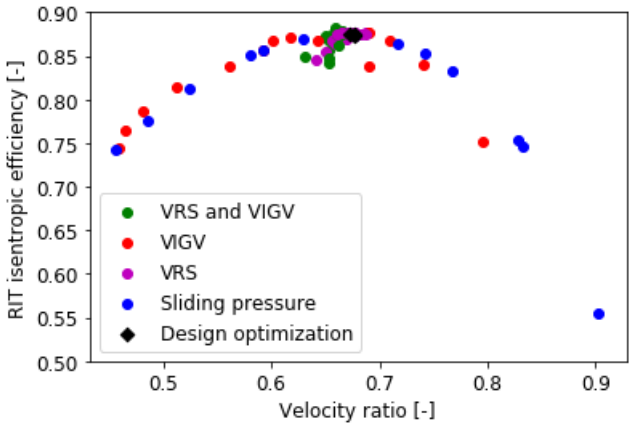

Figure 16 RIT efficiencies and velocity ratios obtained by the design- and performance optimizations of designs 1-3 in this work.

4 Conclusions

This paper presented a method for optimizing the design of Rankine cycles using RIT. A novelty of this method is that the geometry of the HXs and the RIT is optimized simultaneously with the cycle state points to maximize performance at the design point. In addition, the paper also presented a method to optimize the performance of the Rankine cycle. A novelty of this method is the selection of four different approaches to control the cycle. Both methods follow a novel equation-oriented approach enabling the use of an efficient gradient-based optimization algorithm. This means that the underlying Rankine cycle model doesn't have to be solved at each intermediate optimization iteration which reduces the computational cost.

The capabilities of the proposed methods were demonstrated through a case study for power generation from the batch-wise casting process at a representative ferroalloy plant. More specifically the proposed methods were used to design and analyze three Rankine cycles with CO_2 as the working fluid. The main results from the case study are the following:

- The design optimization problem contains few local optimums, and the design optimization method converges to the global optimum with a high probability regardless of the starting point used for optimization.
- The "VRS and VIGV" control approach yield the largest annual electricity production of 12.6 GWh.
- The VRS control approach yields up to 9.2% larger annual electricity production than the sliding pressure control approach due to the increased RIT off-design efficiency.
- The VIGV control approach yields up to 10.5 % larger annual electricity production than the sliding pressure control approach due to the facilitation of operating at larger working fluid pressures.
- The sliding pressure control approach performed best for the Rankine cycle where the RIT and the HXs were designed for optimal performance at an average operating condition. This Rankine cycle operated closer to its design point than the other designs.

Considering the flexibility, robustness and the computational cost of the proposed methods, they can be regarded as a powerful tool for the preliminary design and performance prediction of Rankine cycles.

Acknowledgments

This publication has been funded by HighEFF - Centre for an Energy Efficient and Competitive Industry for the Future, an 8-years' Research Centre under the FME-scheme (Centre for Environment-friendly Energy Research, 257632). The authors gratefully acknowledge the financial support from the Research Council of Norway and user partners of HighEFF.

References

[1] "An official website of the Eurpean Union." https://ec.europa.eu/clima/policies/strategies/2030_en (accessed Jul. 16, 2021).

[2] H. Tian and G. Q. Shu, "Organic Rankine Cycle systems for large-scale waste heat recovery to produce electricity," *Org. Rank. Cycle Power Syst. Technol. Appl.*, pp. 613–636, 2017, doi: https://doi.org/10.1016/B978-0-08-100510-1.00017-X.

[3] A. Guercio and R. Bini, "Biomass-fired Organic Rankine Cycle combined heat and power systems," *Org. Rank. Cycle Power Syst. Technol. Appl.*, pp. 527–567, 2017, doi: https://doi.org/10.1016/B978-0-08-100510-1.00015-6.

[4] M. Orosz and R. Dickes, "Solar thermal powered Organic Rankine Cycles," *Org. Rank. Cycle Power Syst. Technol. Appl.*, pp. 569–612, 2017, doi: https://doi.org/10.1016/B978-0-08-100510-1.00016-8.

[5] C. Spadacini, L. G. Xodo, and M. Quaia, "Geothermal energy exploitation with Organic Rankine Cycle technologies," *Org. Rank. Cycle Power Syst. Technol. Appl.*, pp. 473–525, 2017, doi: https://doi.org/10.1016/B978-0-08-100510-1.00014-4.

[6] B. F. Tchanche, M. Pétrissans, and G. Papadakis, "Heat resources and organic Rankine cycle machines," *Renew. Sustain. Energy Rev.*, vol. 39, pp. 1185–1199, 2014, doi: https://doi.org/10.1016/j.rser.2014.07.139.

[7] S. C. Gülen, "Steam Turbine—Quo Vadis?," *Front. Energy Res.*, vol. 8, pp. 1–20, 2021, doi: https://doi.org/10.3389/fenrg.2020.612731.

[8] P. Colonna *et al.*, "Organic Rankine Cycle Power Systems: From the Concept to Current Technology, Applications, and an Outlook to the Future," *J. Eng. Gas Turbines Power*, vol. 137, no. 10, 2015, doi: https://doi.org/10.1115/1.4029884.

[9] E. Macchi, "Theoretical basis of the Organic Rankine Cycle," *Org. Rank. Cycle Power Syst.*, pp. 3–24, 2017, doi: https://doi.org/10.1016/B978-0-08-100510-1.00001-6.

[10] K. Brun, P. Friedman, and R. Dennis, *Fundamentals and Applications of Supercritical Carbon Dioxide (sCO₂) Based Power Cycles,*. Woodhead Publishing, 2017.

[11] F. Capra and E. Martelli, "Numerical optimization of combined heat and power Organic Rankine Cycles – Part B: Simultaneous design & part-load optimization," *Energy*, vol. 90, pp. 329–343, 2015, doi: https://doi.org/10.1016/J.ENERGY.2015.06.113.

[12] E. Martelli, F. Capra, and S. Consonni, "Numerical optimization of Combined Heat and Power Organic Rankine Cycles – Part A: Design optimization," *Energy*, vol. 90, pp. 310–328, 2015, doi: https://doi.org/10.1016/J.ENERGY.2015.06.111.

[13] S. Quoilin, R. Aumann, A. Grill, A. Schuster, V. Lemort, and H. Spliethoff, "Dynamic modeling and optimal control strategy of waste heat recovery Organic Rankine Cycles," *Appl. Energy*, vol. 88, no. 6, pp. 2183–2190, 2011, doi: https://doi.org/10.1016/j.apenergy.2011.01.015.

[14] S. Schuster, C. N. Markides, and A. J. White, "Design and off-design optimisation of an organic Rankine cycle (ORC) system with an integrated radial turbine model," *Appl. Therm. Eng.*, vol. 174, no. 115192, 2020, doi: https://doi.org/10.1016/J.APPLTHERMALENG.2020.115192.

[15] S. Dong, X. Hu, J. F. Huang, T. Zhu, Y. Zhang, and X. Li, "Investigation on improvement potential of ORC system off-design performance by expander speed regulation based on

theoretical and experimental exergy-energy analyses," *Energy*, vol. 220, no. 119753, 2021, doi: https://doi.org/10.1016/j.energy.2021.119753.

[16] S. Bahamonde, M. Pini, C. De Servi, A. Rubino, and P. Colonna, "Method for the Preliminary Fluid Dynamic Design of High-Temperature Mini-Organic Rankine Cycle Turbines," *J. Eng. Gas Turbines Power*, vol. 139, no. 8, pp. 1–14, 2017, doi: https://doi.org/10.1115/1.4035841.

[17] P. Valdimarsson, "Radial inflow turbines for Organic Rankine Cycle systems," *Org. Rank. Cycle Power Syst. Technol. Appl.*, pp. 321–334, 2017, doi: https://doi.org/10.1016/B978-0-08-100510-1.00010-7.

[18] H. Moustapha, M. F. Zelesky, N. C. Baines, and D. Japikse, *Axial and Radial Turbines*. Vermont, USA: Concepts NREC, 2003.

[19] S. W. Spence and D. W. Artt, "Experimental performance evaluation of a 99.0 mm radial in flow nozzled turbine with different stator throat areas," in *Proceedings of the Institution of Mechanical Engineers, Part A: Journal of Power and Energy*, 1997, vol. 211, pp. 477–488.

[20] S. W. T. Spence, W. J. Doran, and D. W. Artt, "Experimental performance evaluation of a 99.0 mm radial inflow nozzled turbine at larger stator-rotor throat area ratios," *Proc. Inst. Mech. Eng. Part A J. Power Energy*, vol. 213, no. 3, pp. 205–218, 1999, doi: 10.1243/0957650991537554.

[21] B. A. L. Hagen, R. Agromayor, and P. Nekså, "Equation-Oriented Methods for Design Optimization and Performance Analysis of Radial Inflow Turbines," *Energy*, vol. 237, no. 121596, 2021, doi: https://doi.org/10.1016/j.energy.2021.121596.

[22] D. Hu, S. Li, Y. Zheng, J. Wang, and Y. Dai, "Preliminary design and off-design performance analysis of an Organic Rankine Cycle for geothermal sources," *Energy Convers. Manag.*, vol. 96, pp. 175–187, 2015, doi: https://doi.org/10.1016/J.ENCONMAN.2015.02.078.

[23] L. Zhai *et al.*, "An improved modeling for low-grade organic Rankine cycle coupled with optimization design of radial-inflow turbine," *Energy Convers. Manag.*, vol. 153, pp. 60–70, 2017, doi: http://dx.doi.org/10.1016/j.enconman.2017.09.063.

[24] L. Palagi, E. Sciubba, and L. Tocci, "A neural network approach to the combined multi-objective optimization of the thermodynamic cycle and the radial inflow turbine for Organic Rankine cycle applications," *Appl. Energy*, vol. 237, pp. 210–226, 2019, doi: https://doi.org/10.1016/j.apenergy.2019.01.035.

[25] Y. Du, K. Chen, and Y. Dai, "A study of the optimal control approach for a Kalina cycle system using a radial-inflow turbine with variable nozzles at off-design conditions," *Appl. Therm. Eng.*, vol. 149, pp. 1008–1022, 2019, doi: https://doi.org/10.1016/J.APPLTHERMALENG.2018.12.117.

[26] J. Song *et al.*, "Thermodynamic and economic investigations of transcritical CO2-cycle systems with integrated radial-inflow turbine performance predictions," *Appl. Therm. Eng.*, vol. 165, 2020, doi: 10.1016/j.applthermaleng.2019.114604.

[27] L. Yao and Z. Zou, "A one-dimensional design methodology for supercritical carbon dioxide Brayton cycles: Integration of cycle conceptual design and components preliminary design," *Appl. Energy*, vol. 276, no. 115354, 2020, doi: https://doi.org/10.1016/j.apenergy.2020.115354.

[28] Y. Li, W. Li, X. Gao, and X. Ling, "Thermodynamic analysis and optimization of organic Rankine cycles based on radial-inflow turbine design," *Appl. Therm. Eng.*, vol. 184, no. 116277, 2021, doi: https://doi.org/10.1016/j.applthermaleng.2020.116277.

[29] H. T. Walnum, P. Nekså, L. O. Nord, and T. Andresen, "Modelling and simulation of CO2 (carbon dioxide) bottoming cycles for offshore oil and gas installations at design and off-design conditions," *Energy*, vol. 59, pp. 513–520, 2013, doi:

https://doi.org/10.1016/J.ENERGY.2013.06.071.

[30] B. A. L. Hagen, M. Nikolaisen, and T. Andresen, "A novel methodology for Rankine cycle analysis with generic heat exchanger models," *Appl. Therm. Eng.*, vol. 165, no. 114566, 2020, doi: https://doi.org/10.1016/j.applthermaleng.2019.114566.

[31] V. Gnielinski, "New equations for heat and mass transfer in turbulent pipe and channel flow," *Int. Chem. Eng.*, vol. 16, no. 2. pp. 359–368, 1976.

[32] W. N. Selander, "Explicit Formulas for the Computation of Friction Factors in Turbulent Pipe Flow.," 1978.

[33] M. M. Shah, "A general correlation for heat transfer during film condensation inside pipes," *Int. J. Heat Mass Transf.*, vol. 22, no. 4, pp. 547–556, 1979, doi: 10.1016/0017-9310(79)90058-9.

[34] L. Friedel, "Improved friction pressure drop correlation for horizontal and vertical two-phase pipe flow," 1979.

[35] F. P. Incropera, D. P. Dewitt, T. L. Bergman, and A. S. Lavine, *Fundamentals of Heat and Mass Transfer*, Sixth edit. John Wiley & Sons, 2006.

[36] E. W. Lemmon, I. H. Bell, M. L. Huber, and M. O. McLinden, "NIST Standard Reference Database 23: Reference Fluid Thermodynamic and Transport Properties-REFPROP, Version 10.0, National Institute of Standards and Technology," 2018, doi: https://doi.org/10.18434/T4JS3C.

[37] R. H. Aungier, *Turbine aerodynamics: Axial-flow and radial-inflow turbine design and analysis*. New York: ASME Press, 2005.

[38] K. Schittkowski, "NLPQL: a FORTRAN subroutine solving constrained nonlinear programming problems," *Ann. Oper. Res.*, vol. 5, pp. 485–500, 1986, doi: https://doi.org/10.1007/BF02022087.

[39] M. Astolfi, E. Martelli, and L. Pierobon, "Thermodynamic and technoeconomic optimization of Organic Rankine Cycle systems," *Org. Rank. Cycle Power Syst.*, pp. 173–249, 2017, doi: https://doi.org/10.1016/B978-0-08-100510-1.00007-7.

[40] R. Pili, L. García Martínez, C. Wieland, and H. Spliethoff, "Techno-economic potential of waste heat recovery from German energy-intensive industry with Organic Rankine Cycle technology," *Renew. Sustain. Energy Rev.*, vol. 134, no. February, p. 110324, 2020, doi: 10.1016/j.rser.2020.110324.

[41] M. T. Børset, "Energy dissipation and recovery in the context of silicon production," PhD thesis, NTNU, 2015.

[42] T. Andresen, S. Lingaas, B. A. L. Hagen, and P. Nekså, "Dynamic Analysis of Energy Recovery Utilizing Thermal Storage from Batch-Wise Metal Casting," 2020.

[43] C. M. Invernizzi and D. Bonalumi, "Thermal stability of organic fluids for Organic Rankine Cycle systems," *Org. Rank. Cycle Power Syst. Technol. Appl.*, pp. 121–151, 2017, doi: https://doi.org/10.1016/B978-0-08-100510-1.00005-3.

[44] M. T. White, G. Bianchi, L. Chai, S. A. Tassou, and A. I. Sayma, "Review of supercritical CO2 technologies and systems for power generation," *Appl. Therm. Eng.*, vol. 185, 2021, doi: https://doi.org/10.1016/j.applthermaleng.2020.116447.

[45] G. Musgrove, S. Sullivan, D. Shiferaw, P. Fourspring, and L. Chordia, "Heat exchangers," *Fundam. Appl. Supercrit. Carbon Dioxide Based Power Cycles*, pp. 217–244, 2017, doi: https://doi.org/10.1016/B978-0-08-100804-1.00008-6.

[46] A. Uusitalo, A. Ameli, and T. Turunen-Saaresti, "Thermodynamic and turbomachinery design analysis of supercritical Brayton cycles for exhaust gas heat recovery," *Energy*, vol. 167, pp. 60–79, 2019, doi: https://doi.org/10.1016/j.energy.2018.10.181.

Appendix B Paper V

Dynamic Analysis of Energy Recovery Utilizing Thermal Storage from Batch-Wise Metal Casting

Trond Andresen, Simon Lingaas, Brede A. L. Hagen, Petter Nekså, in *Rankine 2020 Conference*, 2020.

PAPER ID: 1144
DOI: 10.18462/iir.rankine.2020.1144

Dynamic Analysis of Energy Recovery Utilizing Thermal Storage from Batch-Wise Metal Casting

Trond ANDRESEN[(a,*)], Simon LINGAAS[(b)], Brede A. L. HAGEN[(b)], Petter NEKSÅ[(a)]

[(a)] SINTEF Energy Research,
Trondheim, 7034, Norway, [*]trond.andresen@sintef.no
[(b)] Norwegian University of Science and Technology (NTNU), Trondheim, 7034, Norway

ABSTRACT

The thermal exergy contained in the liquid metal in ferroalloy production makes it an interesting source for energy recovery. The heat released during casting is rarely utilized today. This work investigates the feasibility of continuous power production from batch wise ferroalloy casting using an energy recovery system concept that includes a thermal energy storage to buffer captured heat between casting cycles and enable a more stable heat supply to a Rankine cycle. A dynamic model of the heat recovery and storage system was developed, and a demonstration case applied to evaluate basic system behaviour. Every two hours, liquid metal at 1450 °C was poured into moulds and placed in a cooling tunnel. With the investigated concept, only 54.6 % of the available heat was captured into the system, indicating a potential for further improvements. Overall, the system was able to output 667 kWh_{el} from the 4 005 kWh of thermal exergy available in the metal in each casting cycle, equivalent to an exergy efficiency of 16.7 %.

Keywords: Waste heat recovery, Intermittent heat source, Dynamic analysis, Rankine cycle, Energy storage.

1. INTRODUCTION

In order to reduce greenhouse gas emissions and lessen the effects of climate change, it is vital to improve upon the energy efficiency in the industry. One way to increase the industrial energy efficiency is waste heat recovery. The metal industry has large potential for waste heat recovery. The waste heat recovery potential from the iron and steel industry in EU is estimated to be 72 TWh/year (Vance et al., 2019). Off-gases contain the major part of the waste heat in the metal industry. However, the high temperature heat that is released during metal casting has higher specific exergy content and is consequently interesting to consider as a heat source for power production. The casting processes in many steel plants, and all Norwegian ferroalloy and silicon plants (Tangstad, 2013), are performed batch-wise. This adds complexity to both heat capture and practical power production. Due to the high initial temperatures of the metal during casting, radiation is likely the dominant mechanism for heat loss. As radiative power is proportional to the surface temperature to the power of 4, there will be significant and non-linear variations in radiative heat dissipation during a casting cycle. The time from casting until full solidification is also a matter of importance, as it can negatively affect mechanical strength and distribution of impurities in the final product if solidification occurs too quickly or too slowly (Tveit, 1988). A heat recovery system aiming for high utilization rate of heat from metal casting should be designed to handle considerable fluctuations in heat input, as well as being able to buffer captured heat to enable continuous heat and/or power output between batches.

Several concepts for recovering heat released during casting has been proposed in the literature. A flat heat pipe recovery system was designed to recover radiant heat in the steel production industry (Jouhara et al., 2017). A pilot system was built and implemented on a steel wire cooling process, and reported to recover 700 kW of heat. The feasibility of other radiative heat sources has also been examined, such as the ceramics industry (Delpech et al., 2019) or from rotary kilns (Caputo et al., 2011; Du et al., 2018).

In this work we explore the hypothetical feasibility of a proposed integrated power production system aiming to achieve high utilization and conversion efficiency of the available thermal energy in the hot liquid metal, while featuring options for controlling desired cooling rates and continuous power production despite the

intermittent nature of batch casting. The proposed system solution consists of a Heat Recovery Heat Exchanger (HRHE) extracting heat from the liquid metal, a Thermal Energy Storage (TES) for smoothing the time-variability of the heat source and a heat transfer fluid loop supplying heat to a Rankine cycle. Analysing the thermal behaviour of the thermal input and heat recovery system as a crucial first step towards enabling practical and efficient power production from such heat sources. Main focus in this work is thus the feasibility of capturing and translating intermittent heat input from casted metal into sufficiently smooth heat supply to a Rankine cycle, while the Rankine cycle itself is represented quite simplified. The paper is organised as follows: Section 2 presents the proposed power production system. Section 3 presents the methodology used for modelling and simulation of the power production system. The case study used for demonstrating the proposed power production system is presented in Section 4. Section 5 presents and discusses results from the case study. The conclusions drawn from this study are presented in Section 6.

2. ENERGY RECOVERY CONCEPT

Aiming to achieve high power output and controllable metal cooling rates, a system concept for power production is proposed, see Figure 1. A metal production plant with batchwise casting is used as basis for these considerations. The main sequence of each cycle with the proposed system, as shown in Figure 1, is: 1) Molten metal is sequentially poured into moulds, which are moved into a cooling tunnel when full. 2) The moulds stay inside the tunnel for a period of time while dissipating heat to both the ambient and a heat exchanger. 3) The tunnel is emptied and prepared for a new cycle. The extracted moulds can be cooled further with e.g. direct water spray as necessary before being processed further.

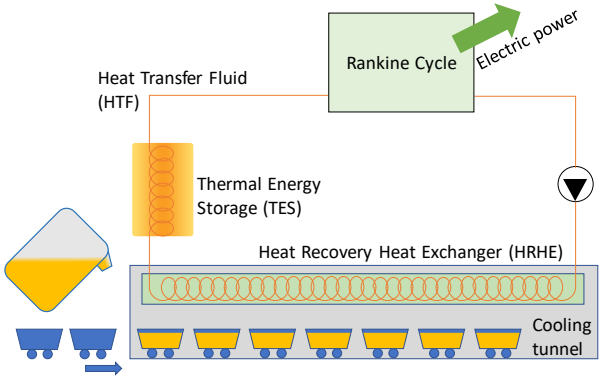

Figure 1: Simple system concept diagram

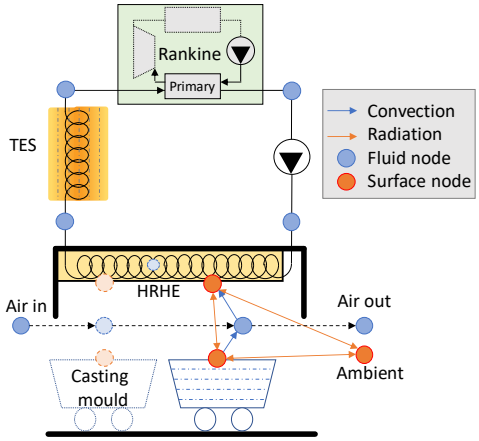

Figure 2: System modelling principles

Inside the cooling tunnel, a heat recovery heat exchanger (HRHE) absorbs heat from the cooling metal and transfers it to the heat transfer fluid (HTF). From the HRHE, the HTF is circulated through a thermal energy storage (TES) and further on to the Rankine cycle's evaporator. The TES will buffer thermal energy to supply the Rankine cycle in the periods without (sufficient) heat input to the HRHE, as well as help mitigate rapid fluctuations in heat input. The temperature level of the HTF loop and TES during a cycle is possible to control through both system design and variables such as fluid flow rates. However, identifying optimum temperatures in dynamic systems such as this is not trivial. Heat-to-power conversion has a higher theoretical maximum efficiency with increasing temperature. At the same time, the temperature level in the TES, HTF loop, and HRHE will determine how much of the thermal energy in the heat source that can be recovered. Higher temperatures in the HTF loop allows for less utilization of the heat source, as heat cannot be recovered when the source is cooled down below the temperature of the fluid in the HRHE.

The proposed system utilizes a single HTF loop for both charging and discharging of the thermal energy storage, instead of having separate loops for charging and discharging. Such systems enable active control of charging and discharging, for example with use of temperature set points in the TES or HTF loop. A single loop system simplifies modeling and operation and does not require a controller to operate the system.

3. METHODOLOGY

A dynamic model of the energy recovery system was implemented using the programming language Modelica, with Dymola being used as the platform for modelling and simulation. The basic modelling principles and included mechanisms of the component models is described in the remainder of this section. The reader is referred to Lingaas (2019) for details regarding governing equations and model code, as well as validation of the individual submodels using reported measurements from the literature. Models for the cooling tunnel, HRHE, and TES were based on geometry parameters such as basic overall dimensions and channel diameters for fluid flow. This enables the use of the overall system model to explore effects of individual component sizes and configurations. Fluid flow was modelled with constant fluid properties and using control volumes. Convective heat transfer coefficients were calculated with the Gnielinski (2013) correlation.

3.1. Cooling tunnel with Heat Recovery Heat Exchanger

Figure 2 illustrates the basic model principles for the cooling tunnel and HTF loop. The cooling tunnel includes several casting moulds, the heat recovery heat exchanger, tunnel wall, and air flow. The sub-models are discretized along the length of the tunnel. The HRHE is modelled as heat transfer surfaces coupled on one side to the tunnel air and to the HTF on the other. The HRHE surface area facing the air equals the tunnel footprint. Heat loss from the HRHE to the ambient via the tunnel walls is calculated using a constant heat transfer coefficient. Convective heat transfer is modelled between the air and HRHE outer surface, HTF and HRHE inner surface, and the air and the casting mould surface. Radiative heat transfer is modelled using the radiation heat transfer network method described in (Incorpera et al., 2006). Three surfaces are considered here: the surface of the casted metal, the HRHE outer surface, and the surroundings, i.e. radiation lost through the tunnel openings in each end. The surroundings are assumed to be a black body with emissivity of 1 from which insignificant amounts of heat radiate back into the tunnel. A fixed flow rate of air through the tunnel is assumed.

3.2. Casting mould

Each casting mould is modelled as a box-shaped thermal mass discretized both vertically and along the tunnel length axis. The mould model only considers the casted metal, ignoring any physical and thermal impact of a mould frame itself. The mould has one external surface facing upwards exchanging heat with the surroundings, and the other surfaces are assumed to be adiabatic. This is similar to other simple metal solidification models (Benham et al., 2016). The sum of mould surface areas is equal to the tunnel footprint (length x width). For a fixed mass of metal, the specified tunnel footprint thus also determines the exposed mould surface area and the mould depth. Mould surface area directly influences radiative power. Heat conduction between each layer is modelled using thermal resistances. Temperature dependent enthalpy reflects both a constant heat capacity and the enthalpy of fusion in the liquidus-solidus temperature interval. For the material used in the demonstration case described in Section 4, the heat capacity was 0.812 $kJ \times kg^{-1} \times K^{-1}$ for both liquid and solid phases, and the enthalpy of fusion was 1100 $kJ \times kg^{-1}$ uniformly distributed over the interval of 1350 - 1205 °C.

3.3. Thermal energy storage

The thermal energy storage (TES) was modelled as described by Jian (2015), where a thermal energy storage is modelled using the lumped capacitance assumption while defining an effective heat transfer coefficient to describe heat transfer from the HTF to the storage material. To simplify the model, a single heat transfer tube with its surrounding material was modelled, and the model was scaled up assuming symmetry to properly represent the actual size of the storage. Constant thermal properties of the storage material were assumed.

3.4. Rankine cycle

As the primary focus in this work is behaviour and performance of the overall heat capture system, the Rankine cycle is represented in a quite simplified manner. Only the behaviour of the HTF exchanging heat with the working fluid (WF) in the primary heat exchanger is considered. The primary heat exchanger is discretized into several control volumes of equal and constant UA-value. The working fluid enters the primary heat exchanger at a fixed temperature and flow rate, and the outlet temperature is calculated based on the heat transferred. Net power produced, $\dot{W}_{el}$, is estimated using a fixed exergy efficiency, B, multiplied with the exergy transferred *into* the Rankine cycle; $\dot{W}_{el} = B * \eta_{carnot} * \dot{Q}_{Primary}$, where $\eta_{carnot} = 1 - \frac{T_{amb}}{T_{HTF,in} - T_{HTF,out}} * ln\left(\frac{T_{HTF,in}}{T_{HTF,out}}\right)$. In other words, the working fluid side of the Rankine cycle is not directly used

to estimate net power. However, the load- and temperature variable behaviour in this heat exchanger affects heat transfer and temperatures in the rest of the HTF loop. This modelling principle, though simplified, provides an estimate for net power sensitive to input exergy as well as realistic impact on the HTF loop. With a constant *B*, part load characteristics are disregarded. We believe this simplification to be adequate, because the intention is to explore the overall system feasibility for integration of a generic power cycle, and not for accurate performance prediction of a specific Rankine cycle.

4. DEMONSTRATION CASE

The model is demonstrated on a test case representing a hypothetical silicon furnace based on parameters and conditions described in Børset (2015); every two hours, 9000 kg of liquid Silicon at 1450°C is cast into multiple moulds and allowed to cool down. A measuring campaign indicated that complete solidification of a mould was reached in 36 minutes after casting, which would be a target to match also in the current work.

The system model was set up using the parameters listed in Table 1. Superheated steam at 20 bar was considered as HTF, and concrete as the TES material. The specified TES thermal capacity of 50 $MJ \times K^{-1}$ is equivalent to 13.7 m³ of concrete. The parameter *tunnel* height is used as the distance from the top of the mould to the surface of the HRHE. The model was initialized by running the model for several cycles until reaching a cyclic steady state. The system was operated without controllers to govern HTF and WF flow rates, thus relying on the behaviour of the system design to mitigate the variability in heat input. The demonstration case results should therefore be considered as conservative regarding any estimates for energy recovery potential.

Table 1: Key model parameters used in demonstration case

Property	Unit	Value	Property	Unit	Value
General			***Tunnel***		
Ambient temperature	°C	25	Dimensions L x W x H	m	21.8 x 2 x 1
Casting cycle duration	s	7 200	Tunnel segments	-	30
Time to fill all moulds	s	1 800	Wall insulation thickness	m	0.01
Mould time inside tunnel	s	6 480	Insulation conductivity	$W \times m^{-1} \times K^{-1}$	0.055
Silicon mass per cycle	kg	9 000	Air flow velocity	$m \times s^{-1}$	1
Silicon initial temperature	°C	1 450	HRHE channel diameter	m	0.1
Silicon emissivity	-	0.55	HRHE surface emissivity	-	0.8
Number of moulds	-	10	***Thermal energy storage***		
Mould vertical segments	-	15	Density	$kg \times m^{-3}$	3 100
Rankine exergy efficiency, *B*	-	50 %	Specific heat capacity	$J \times kg^{-1} \times K^{-1}$	1 100
Heat Transfer Fluid (HTF)	-	Steam	Thermal conductivity	$W \times m^{-1} \times K^{-1}$	2.65
HTF pressure	bar	20	Total thermal capacity	$MJ \times K^{-1}$	50
HTF mass flow rate	$kg \times s^{-1}$	15	Channel diameter	m	0.15
			Channel pitch	m	0.9

5. RESULTS AND DISCUSSION

Summarized results from one casting cycle are shown in Table 2. The system managed to fully solidify the silicon within the targeted 36 minutes. Figure 3 shows the temperature distribution in one casting mould for the duration of the casting cycle. At the end of the cycle, the moulds exited the cooling tunnel at an average temperature of 427 °C. At this point, the metal contained around 15% of the initial thermal energy but only 8 % of the initial thermal exergy. The potential for further energy recovery is therefore quite limited. Overall, the system managed to recover 54.6% of the thermal energy, and 16.7% of the thermal exergy initially present in the molten metal. For 8000 hours of operation annually, the system could produce 2.7 GWh_{el}/y. Figure 4 shows the overall heat flows surrounding the tunnel, including losses to the ambient via different paths. The

10 sharp spikes in heat flow indicate the introduction of each mould into the tunnel. The rapid initial decline after each spike is the result of the metal surface cooling down to the onset of solidification within a couple of minutes. The surface cooling from the initial 1450 °C to 1350 °C reduces the radiative heat loss by over 20%.

Table 2: Summarized results from simulation

Property	Unit	Value
Initial thermal energy in Si	MWh	5.64
Initial thermal exergy in Si	MWh	4.05
Thermal energy recovered in the HRHE	MWh	3.08
Electric energy produced	kWh_{el}	676
Maximum variation in power output	kW_{el}	259
Average metal temperature at cycle end	°C	427
Remaining thermal energy in Si at cycle end	MWh	0.81
Remaining thermal exergy in Si at cycle end	MWh	0.25
Metal solidification time	min	36
Average TES temperature	°C	384
Maximum local TES temperature	°C	427
Variation in WF turbine inlet temperature	K	106

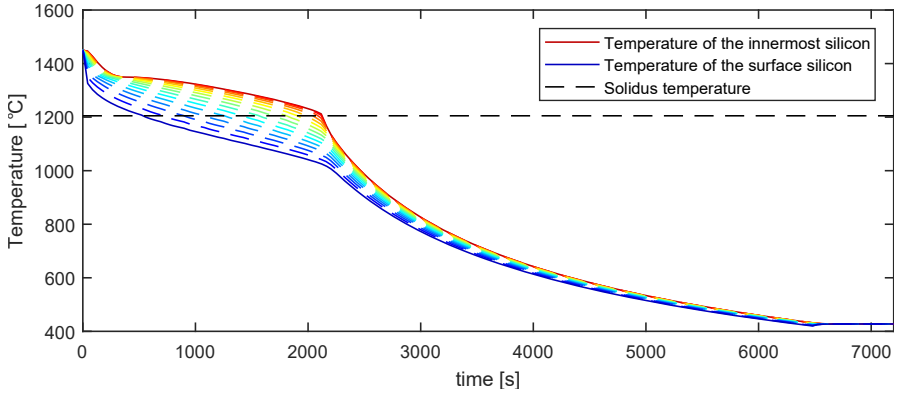

Figure 3: Temperature distribution in one casting mould

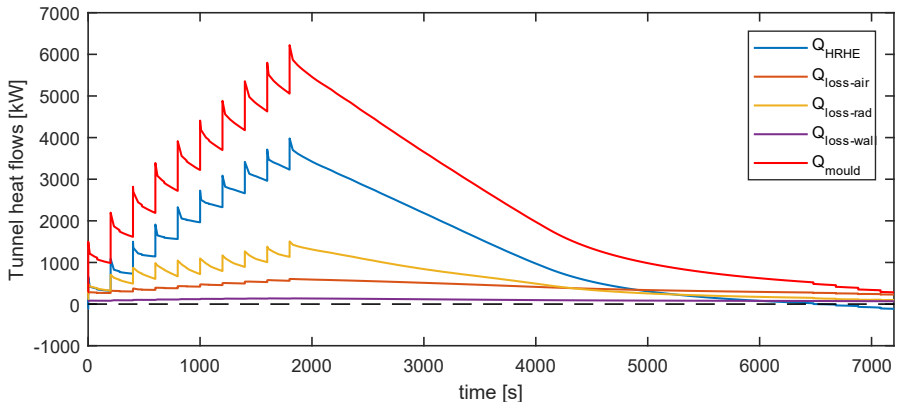

Figure 4: Heat flows around the cooling tunnel

The largest heat loss is caused by radiation through the openings in each end of the tunnel. Convective heat loss to the air flow is also significant. Both losses could likely be reduced by changing the tunnel geometry to reduce radiation paths to the ambient or by adding doors to fully close the tunnel during operation.

Additional heat flows and temperature profiles are shown in Figure 5 a-d. The average HRHE heat flow was 1.54 MW, with a peak of 4 MW. Given the constraint on solidification time, this peak cannot be easily reduced by for example controlling the heat dissipation rate. The system output was 338 kW_{el} electric power on average, but with a variation between maximum and minimum power output of 260 kW_{el} as can be seen by the W_{net} line in Figure 5a. However, the system managed a fairly consistent power output considering the much larger variation in heat and exergy input, and the lack of active control of both heat buffering and Rankine cycle. Unlike the large variations in HRHE duty, it should be feasible to reduce variations in Rankine power output by implementing control strategies and considering more advanced system configurations the allow better control of heat flow from the HTF loop to the TES and Rankine cycle.

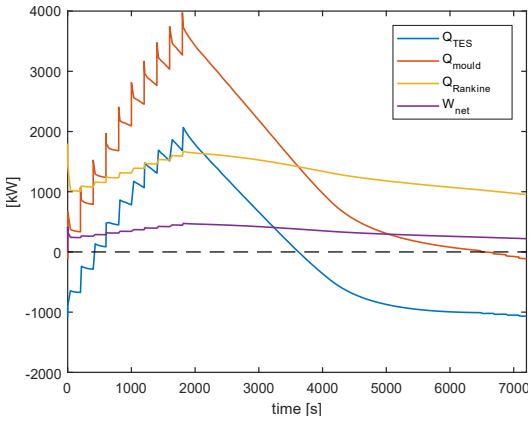

a) Key heat flows and net power

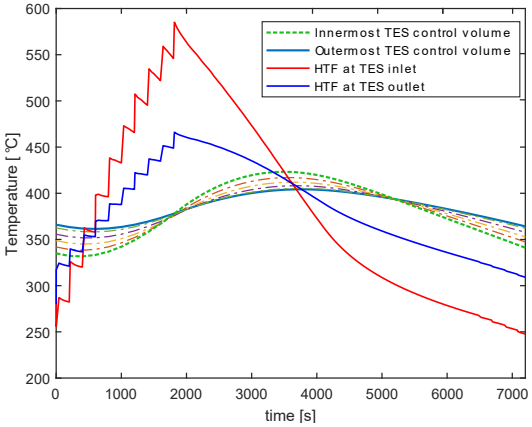

b) Temperature profiles in the TES

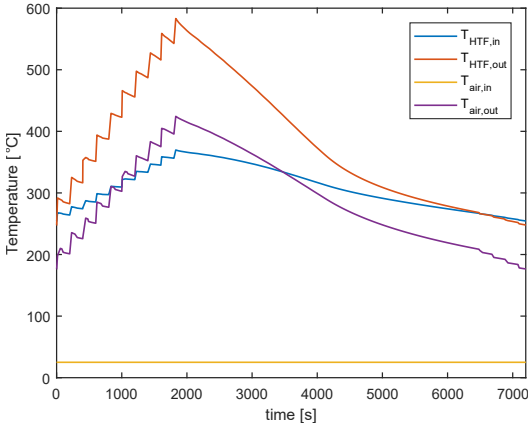

c) Air and HTF temperatures at inlet and outlet of cooling tunnel

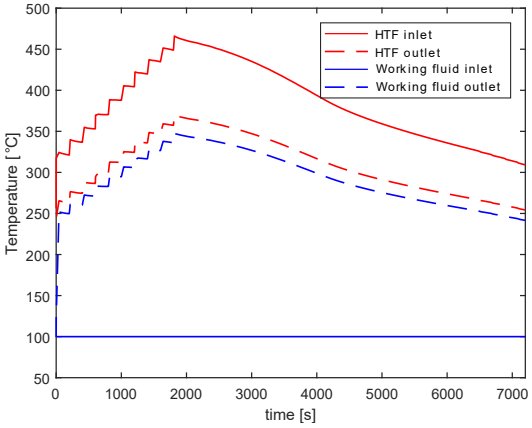

d) HTF and WF temperatures in and out of the Rankine cycle primary heat exchanger

Figure 5: Heat flows and temperature profiles

The effect of the TES in the system can also be analysed in Figure 5. In Figure 5a, the blue line represents TES heat input. From ~500 to ~3500 seconds into the cycle, TES heat input is above zero, indicating that the TES is being charged. The rest of the time, the TES provides a net heat input to the HTF loop. Figure 5b shows temperatures of the thermal storage control volumes and the HFT in the TES. The average TES temperature was 384 °C, with variations during the cycle of ±50 K. Figure 5d shows fluid temperatures across the primary heat exchanger in the Rankine cycle. As discussed in Chapter 3, only the HFT side was used to estimate power production potential. The average HTF inlet temperature at the Rankine primary heat exchanger was around

350 °C, indicating that much of the specific exergy from the heat source was lost even before reaching the Rankine cycle. At least parts of these losses are intrinsic to the cyclic availability of the heat source in the explored case.

Figure 6 illustrates the impact of a TES in the system. The system was simulated again with identical parameters but with the TES removed. Without any TES, the system experiences a fluctuation in HTF temperature at the HRHE outlet of 425 K, compared to around 100 K with the specified thermal capacity in the demonstration case.

Figure 7 shows the distribution of heat loss from the silicon moulds accumulated over one casting cycle for different tunnel heights. With all other parameters fixed, simulation results for different tunnel heights shows a significant potential to improve fraction of heat recovered in the HRHE.

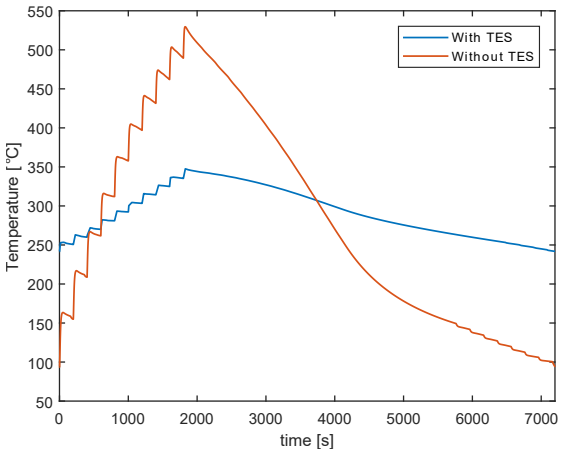

Figure 6: HRHE HTF outlet temperature with and without TES present in system

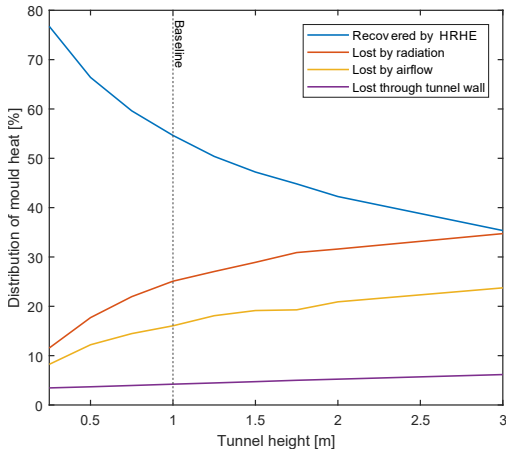

Figure 7: Overall mould heat loss distribution at varying tunnel height

6. CONCLUSIONS

This work has investigated the feasibility of continuous heat recovery and power production from batch wise metal casting. An energy recovery system concept was described, and a dynamic model developed. A demonstration case was applied to evaluate basic system behaviour and to provide some insight into practical feasibility. The simulation results indicated that the heat recovery heat exchanger and heat transfer loop must handle significant variations in heat load, but even the fairly simple thermal energy storage configuration analysed in this work was found to buffer heat input fluctuations well. Overall, the system was able to output 667 kWh_{el} from the 4 005 kWh of exergy available in the metal each casting cycle, equivalent to an exergy efficiency of 16.7 %. However, only 54.6 % of the available heat was captured into the system, indicating a potential for design and control improvements. The dynamic system model proved capable of providing useful insights into the behaviour of such an energy recovery system. Future work should expand the model to consider a full Rankine cycle to enable more accurate power conversion estimates, evaluate control strategies, and analysis of practical feasibility.

ACKNOWLEDGEMENTS

This publication has been funded by HighEFF - Centre for an Energy Efficient and Competitive Industry for the Future, an 8-year Research Centre under the FME-scheme (Centre for Environment-friendly Energy Research, 257632). The authors gratefully acknowledge the financial support from the Research Council of Norway and user partners of HighEFF.

REFERENCES

Benham, G., Hildal, K., Please, C. P., Van Gorder, R. A., 2016. Solidification of silicon in a one-dimensional slab and a two-dimensional wedge. International Journal of Heat and Mass Transfer 98, 530-540.

Børset, M. T., 2015. Energy Dissipation and Recovery in the Context of Silicon Production: Exergy Analysis and Thermoelectricity. PhD thesis, Norwegian University of Science and Technology.

Caputo, A. C., Pelagagge, P. M., Salini, P., 2011. Performance modeling of radiant heat recovery exchangers for rotary kilns. Applied Thermal Engineering 31(14-15), 2578-2589.

Delpech, B., Axcell, B., Jouhara, H., 2019. Experimental investigation of a radiative heat pipe for waste heat recovery in a ceramics kiln. Energy 170, 636 – 651.

Du, W. J., Yin, Q., Cheng, L., 2018. Experiments on novel heat recovery systems on rotary kilns. Applied Thermal Engineering 139, 535 – 541.

Gnielinski, V., 2013. On heat transfer in tubes, Int. J. of Heat and Mass Transfer 63, 134-140.

Incorpera, F. P., Dewitt, D. P., Bermann, T. L., Lavine, A. S., 2005. Fundamentals of Heat and Mass Transfer, 6th ed. John Wiley & Sons, 2005.

Jian, Y., Bai, F., Falcoz, Q., Xu, C., Wang, Y., Wang, Z., 2015, Thermal analysis and design of solid energy storage systems using a modified lumped capacitance method. Applied Thermal Engineering 75, 213 – 223.

Jouhara, H., Almahmoud, S., Chauhan, A., Delpech, B., Bianchi, G., Tassou, S. A., Llera, R., Lago, F., Arribas, J. J., 2017. Experimental and theoretical investigation of a flat heat pipe heat exchanger for waste heat recovery in the steel industry. Energy 141, 1928-1939.

Lingaas, S., 2019. Heat-to-power conversion from variable surplus heat sources utilizing a thermal energy storage. Msc thesis, Norwegian University of Science and Technology

Schei, A., 1998. Production of high silicon alloys. Tapir, Trondheim, Norway.

Tangstad, M., 2013. Metal production in Norway. Akademika, Norway, 240.

Tveit, H., 1988. Størkning av 75% ferrosilisium : forløp, struktur og styrke. Ph.D. thesis, Norges Tekniske Høgskole, Trondheim.

Vance, D., Nimbalkar, S., Thekdi, A., Armstrong, K., Wenning, T., Cresko, J., Jin, M., 2019. Estimation of and barriers to waste heat recovery from harsh environments in industrial processes. Journal of Cleaner Production 222, 539 – 549.